



**Pre-normative REsearch for Safe use of Liquid Hydrogen (PRESLHY)**

Project Deliverable

## **Detailed description of novel engineering correlations and tools for LH<sub>2</sub> safety, version 2**

Deliverable Number:	6.5
Work Package:	6
Version:	2.2
Author(s), Institution(s):	D. Cirrone (UU), D. Makarov (UU), V. Molkov (UU), A. Venetsanos (NCSRDI), S. Coldrick (HSE), G. Atkinson (HSE), C. Proust (INERIS), A. Friedrich (PS), M. Kuznetsov (KIT)
Submission Date:	30 April 2021
Due Date:	30 April 2021
Report Classification:	Public



**FUEL CELLS AND HYDROGEN  
JOINT UNDERTAKING**



This project has received funding from the Fuel Cells and Hydrogen 2 Joint Undertaking under the European Union's Horizon 2020 research and innovation programme under grant agreement No 779613.

History		
Nr.	Date	Changes/Author
1.0	19.12.2019	MS29 Detailed description of novel engineering tools for LH <sub>2</sub> version 1 / D. Cirrone (UU), A. Venetsanos (NCSRD)
1.1	24.03.2020	Contribution to Section 3.5 / S. Coldrick (HSE)
1.2	30.11.2020	Contribution to Section 5.3 / D. Cirrone (UU)
1.3	31.03.2021	Contribution to Sections 3.2 and 5.6 / D. Cirrone (UU)
1.4	06.04.2021	Contribution to Section 3.3 / A. Venetsanos (NCSRD)
1.5	09.04.2021	Contribution to Sections 3.4 and 5.1 / C. Proust (INERIS) Contribution to Section 4.2 / A. Friedrich (PS) Contribution to Section 5.4 / D. Cirrone (UU)
1.6	15.04.2021	Contribution to Section 5.5 / M. Kuznetsov (KIT)
2.0	17.04.2021	Final version for review / D. Cirrone (UU)
2.1	29.04.2021	Final version after review / D. Cirrone (UU)
2.2	31.05.2021	Version updated with change of tool N.2's name in table 1 (p.14), update in description within section 3.3, update of figure 22 (p.55) according to latest experimental results, correction of hazard distances in p.66, correction of eq. 5.42 (p.88).

Approvals			
Version	Name	Organisation	Date
2.0	J. Wen	UWAR	25 April 2021
2.0	P. Sathiah	Shell	25 April 2021

## Acknowledgements

This project has received funding from the Fuel Cells and Hydrogen 2 Joint Undertaking under the European Union's Horizon 2020 research and innovation programme under grant agreement No 779613.

## Disclaimer

Despite the care that was taken while preparing this document the following disclaimer applies: The information in this document is provided as is and no guarantee or warranty is given that the information is fit for any particular purpose. The user thereof employs the information at his/her sole risk and liability.

The document reflects only the authors' views. The FCH JU and the European Union are not liable for any use that may be made of the information contained therein.

## Key words

Liquid hydrogen, cryogenic hydrogen, safety, dispersion, fire, hazard distances, engineering correlations and tools.

## Publishable summary

This report gathers and presents the engineering correlations developed and validated within PRESLHY project to close the relevant knowledge gaps associated to cryogenic and liquid hydrogen safety and to calculate the hazard distances of relevant accident scenarios. The unique experimental data generated within PRESLHY project in the technical work packages 3-5 were used to develop empirical or semi-empirical correlations or for validation of novel engineering tools and models. In addition to PRESLHY outcomes, experimental data available in the literature were also employed to widen the pool of covered phenomena and validation ranges. Validated engineering correlations will be fed into recommendations for Regulations Codes and Standards (RCS). This deliverable provides the description of the engineering correlations and tools according to a unified template to ease future implementation into existing and/or future integrated platforms for hazards and risks assessment, e.g. the e-Laboratory developed within the ongoing project Net-Tools.

## Abbreviations

BLEVE	Boiling Liquid Expanding Vapour Explosion
BR	Blockage ratio
CFD	Computational Fluid Dynamics
DDT	Deflagration to Detonation Transition
EoS	Equation of State
FA	Flame Acceleration
GH <sub>2</sub>	Gaseous Hydrogen
HEM	Homogeneous Equilibrium Model
HNEM	Homogeneous Non Equilibrium Model
IR	Infrared
LFL	Lower Flammable Limit
LH <sub>2</sub>	Liquefied Hydrogen
LNG	Liquefied Natural Gas
MIE	Minimum Ignition Energy
PIF	Possible Impossible Flow
PIRT	Phenomena Identification and Ranking Table
RCS	Recommendations Codes and Standards
RH	Relative Humidity
RPT	Rapid phase transition
RUD	Run Up Distance

## Table of Contents

<b>Acknowledgements .....</b>	<b>ii</b>
<b>Disclaimer.....</b>	<b>ii</b>
<b>Key words.....</b>	<b>ii</b>
<b>Abbreviations .....</b>	<b>iv</b>
<b>Table of Contents.....</b>	<b>v</b>
<b>List of figures .....</b>	<b>viii</b>
<b>List of tables.....</b>	<b>x</b>
<b>1 Introduction and scope.....</b>	<b>13</b>
1.1 Phenomena.....	13
<b>2 List of engineering correlations.....</b>	<b>14</b>
2.1 Synergy and interconnections.....	14
2.2 Description of engineering correlations.....	15
<b>3 Release and mixing.....</b>	<b>17</b>
3.1 The similarity law for concentration decay in momentum jets (UU) .....	17
3.1.1 Introduction .....	17
3.1.2 Nomenclature.....	17
3.1.3 Model description.....	17
3.1.4 Validity range .....	18
3.1.5 Input values.....	19
3.1.6 Output values.....	19
3.1.7 Conclusions .....	19
3.1.8 References.....	19
3.2 The non-adiabatic blowdown model for a hydrogen storage tank (UU) .....	20
3.2.1 Introduction .....	20
3.2.2 Nomenclature.....	20
3.2.3 Model description.....	21
3.2.3.1 Convective heat transfer coefficient.....	21
3.2.3.2 Change of internal energy in the tank .....	22
3.2.3.3 Calculation of temperature at the wall: <i>T<sub>wint</sub></i> and <i>T<sub>wext</sub></i> .....	22
3.2.3.4 Heat transfer through the discharge line .....	23
3.2.3.5 Under-expanded jet theory .....	23
3.2.4 Validity range .....	24
3.2.5 Input values.....	29
3.2.6 Calculation procedure .....	29
3.2.7 Output values.....	30
3.2.8 Conclusions .....	30
3.2.9 References.....	30
3.3 DISCHA tool, for physical properties and discharge calculations (NCSRD) .....	31
3.3.1 Introduction .....	31
3.3.2 Model description.....	31
3.3.2.1 Physical properties and phase-change model .....	31
3.3.2.2 Tank model .....	31
3.3.2.3 Pipe flow model.....	32
3.3.2.4 Pipe wall heat transfer model .....	32

3.3.2.5 Fictitious nozzle models .....	32
3.3.3 Validity range .....	33
3.3.4 Input values.....	35
3.3.5 Calculation procedure (possible algorithm) .....	35
3.3.5.1 Mass flow rate calculation .....	35
3.3.5.2 Pipe step calculation .....	35
3.3.5.3 Tank state calculation.....	36
3.3.5.4 Numerics .....	36
3.3.6 Output values.....	36
3.3.7 Interface (GUI) .....	36
3.3.8 References.....	36
<b>3.4 Extent of cryogenic pools – HyPond (INERIS) .....</b>	<b>37</b>
3.4.1 Introduction .....	37
3.4.2 Nomenclature.....	37
3.4.3 Model description.....	37
3.4.4 Validity range .....	40
3.4.5 Input values.....	40
3.4.6 Output values.....	41
3.4.7 Conclusions .....	41
3.4.8 References.....	41
<b>3.5 Method for calculating the final state when mixing liquid hydrogen and moist air (HSE)42</b>	
3.5.1 Introduction .....	42
3.5.2 Nomenclature.....	42
3.5.3 Model description.....	42
3.5.4 Equations for thermodynamic properties .....	44
3.5.5 Input values.....	46
3.5.6 Validity range .....	46
3.5.7 Output values.....	46
3.5.8 Conclusions .....	48
3.5.9 References.....	49
<b>4 Ignition.....</b>	<b>50</b>
4.1 Ignition Energy for hydrogen-air mixtures (UU).....	50
4.1.1 Introduction .....	50
4.1.2 Nomenclature.....	50
4.1.3 Model description.....	50
4.1.3.1 Calculation of parameters for the unburnt and burnt mixtures.....	51
4.1.3.2 Calculation of the laminar flame speed.....	52
4.1.4 Validity range .....	53
4.1.5 Input values.....	55
4.1.6 Output values.....	55
4.1.7 Conclusions .....	55
4.1.8 References.....	55
4.2 Electrostatic field built-up generated during hydrogen releases (PS) .....	56
4.2.1 Introduction .....	56
4.2.2 Nomenclature.....	57

4.2.3 Model description .....	57
4.2.4 Validity range .....	59
4.2.5 Input values.....	60
4.2.6 Output values.....	60
4.2.7 Conversion of input and output units .....	60
4.2.8 Conclusions .....	61
<b>5 Combustion .....</b>	<b>62</b>
5.1 Laminar burning velocity and expansion ratios for hydrogen-air mixtures (INERIS) ....	62
5.1.1 Introduction .....	62
5.1.2 Nomenclature.....	62
5.1.3 Model description.....	62
5.1.4 Validity range .....	64
5.1.5 Calculation procedure .....	64
5.1.6 Conclusions .....	64
5.1.7 References.....	65
5.2 Flame length correlation and hazard distances for jet fires (UU).....	65
5.2.1 Introduction .....	65
5.2.2 Nomenclature.....	65
5.2.3 Model description.....	65
5.2.4 Validity range .....	67
5.2.5 Input values.....	67
5.2.6 Output values.....	67
5.2.7 Conclusions .....	68
5.2.8 References.....	68
5.3 Assessment of thermal load from hydrogen jet fires (UU) .....	68
5.3.1 Introduction .....	68
5.3.2 Nomenclature.....	68
5.3.3 Model description.....	69
5.3.4 Validity range .....	71
5.3.4.1 Validation against experimental tests on hydrogen jet fires .....	72
5.3.5 Input values.....	76
5.3.6 Output values.....	76
5.3.7 Conclusions .....	76
5.3.8 References.....	76
5.4 Maximum pressure load from delayed ignition of turbulent jets (UU) .....	77
5.4.1 Introduction .....	77
5.4.2 Nomenclature.....	77
5.4.3 Model description.....	78
5.4.4 Validity range .....	79
5.4.5 Input values.....	80
5.4.6 Output values.....	80
5.4.7 Conclusions .....	80
5.4.8 References.....	81
5.5 Flame acceleration and detonation transition for cryogenic hydrogen-air mixtures (KIT/PS) .....	81

5.5.1 Introduction .....	81
5.5.2 Nomenclature.....	82
5.5.3 Model description .....	82
5.5.3.1 Flame acceleration .....	83
5.5.3.2 Detonation onset. DDT conditions .....	85
5.5.3.3 Mixture characterization. Strength of the explosion. ....	88
5.5.4 Validity range .....	92
5.5.5 Calculation procedure: required parameters and algorithm .....	92
5.5.5.1 Option1: Sonic deflagration in obstructed tube (BR=0.3) .....	93
5.5.5.2 Option 2: Detonation in obstructed tube (BR=0.3) .....	95
5.5.5.3 Option 3: Slow deflagration in obstructed tube (BR=0.6) .....	97
5.5.5.4 Option 4: Detonation in smooth tube (BR=0) .....	99
5.5.6 Conversion units .....	100
5.5.7 Conclusions .....	101
5.5.8 References.....	101
5.6 Fireball size after liquid hydrogen spill combustion (UU, KIT) .....	102
5.6.1 Introduction .....	102
5.6.2 Nomenclature.....	102
5.6.3 Model description .....	102
5.6.4 Validity range .....	102
5.6.5 Input and output values.....	103
5.6.6 Conclusions .....	103
5.6.7 References.....	103
<b>6 Conclusions .....</b>	<b>104</b>
<b>Annex 1. Template for tool description .....</b>	<b>105</b>

## List of figures

Figure 1. Cryogenic gaseous hydrogen jet: outlook of the applicable engineering correlations to quantify associated hazards.....	15
Figure 2. Liquid hydrogen spill: outlook of the applicable engineering correlations to quantify associated hazards.....	15
Figure 3. The similarity law and experimental data on axial concentration decay in momentum controlled expanded and under-expanded jets from Hecht and Panda's (2019) tests (solid lines) and data collected in Molkov and Saffers (2013) (diamonds).....	18
Figure 4. Scheme of conjugate heat transfer at a tank wall. .....	22
Figure 5. Scheme of under-expanded jet: 1 – storage tank; 2 – end of pipe prior to restrictor; 3- real nozzle exit; 4 – notional nozzle exit. .....	23
Figure 6. Validation of non-adiabatic blowdown model against cryogenic temperature releases. ....	26
Figure 7. Validation of non-adiabatic blowdown model against ambient temperature releases. ....	28
Figure 8. Temperature dynamics for Test 16w: “closed” versus “open” thermocouples measurements.....	28
Figure 9. Blowdown calculations against INERIS test, see (Venetsanos et al. 2021a).....	34

Figure 10. Blowdown calculations against DISCHA-PS/KIT test, see (Venetsanos et al. 2021a).	34
Figure 11. Representation of the pool formation process (left) and heat flux evolution as function of time during a 1D instantaneous deposit of LH <sub>2</sub> on a paraffin wax thick substrate by Zabetakis et al. (1961) (right). ....	38
Figure 12. Comparison between the predicted evolution of the pool radius and the experimental observation for a 0.42 kg/s LH <sub>2</sub> spill on a thick aluminium plate (points from thermocouple reading and shadowed zone from video records) from Verfondern and Dienhart (1997). ....	40
Figure 13. Saturation pressure as a function of liquid temperature .....	43
Figure 14. Enthalpy of vaporisation of water. ....	44
Figure 15. Variation of final temperature with final hydrogen concentration (v/v) for a range of ambient temperatures (0 - 30 °C) and relative humidities (0%, 50% and 100%). ....	47
Figure 16. Variation of final density difference with final hydrogen concentration (v/v) for a range of ambient temperatures (0-30 °C) and relative humidities (0%, 50% and 100%). ....	48
Figure 17. Effect of release pressure on the final state (saturated vapour pressures are absolute pressures). ....	48
Figure 18. Thermophysical properties of the unburnt and burnt mixture as function of hydrogen concentration in air for ambient temperature (Tu=298K). ....	51
Figure 19. Thermophysical properties of the unburnt (dashed lines) and burnt mixture (solid lines) as function of hydrogen concentration in air for temperature Tu=100-250 K.....	52
Figure 20. Unstretched laminar flame speed calculated through Chemkin software as function of hydrogen concentration in air and temperature of the unburnt mixture. ....	52
Figure 21. Validation of the analytical model versus experiments performed with hydrogen-air mixtures at initial temperature equal to ambient.....	54
Figure 22. Validation of the analytical model versus experiments performed with hydrogen-air mixtures at initial temperature equal to 173 K.....	55
Figure 23. Graphs with extremal field values over initial pressure for each nozzle diameter and corresponding auxiliary lines. ....	58
Figure 24. Derivation of the factors for the engineering correlations for the estimation of field built-up.....	58
Figure 25. Lines for the correlations (4.6) and (4.7) in black together with the experimental data and the auxiliary lines for each nozzle diameter. ....	59
Figure 26. Burner used to measure the laminar burning velocity (left) and intensified IR picture of the flame (right 50% H <sub>2</sub> @ -85°C). ....	63
Figure 27. Evolution of the laminar burning velocity as function of the temperature and of the mixture composition. ....	63
Figure 28. Evolution of the expansion ratio of the combustion as function of the temperature and of the mixture composition. ....	64
Figure 29. The dimensionless correlation for hydrogen jet flames: “+” data from Molkov and Saffers (2013); “◆” data from Cirrone et al. (2019). ....	66
Figure 30. Measured axial temperature as a function of distance normalised to the flame length, and three criteria for jet fire effects (Molkov, 2012). ....	67
Figure 31. Visual representation of the weighted multi source model. ....	71
Figure 32. Validation of the model against SNL tests: a) calculated versus experimental radiative heat flux for Tests 1-5; f) calculated versus experimental flame length for Tests 1-5; g) scheme of the experimental set-up including sensors' location. ....	73

Figure 33. Validation of the model against KIT tests: calculated versus experimental radiative heat flux. ....	74
Figure 34. Validation of model against INERIS test: a) calculated versus experimental radiative heat flux; b) position of radiometers with respect to the flame; c) flame length prediction during storage tank blowdown. ....	75
Figure 35. The correlation for predicting overpressure from delayed ignition of turbulent hydrogen jets versus experiments. ....	79
Figure 36. Combustion regimes for hydrogen-air mixtures in a tube geometry (Dorofeev et al., 2000; 2001). ....	83
Figure 37. Critical expansion ratio as function of initial temperature based on experiments in obstructed tubes (BR=0.3 and BR=0.6): black dashed line is the border between slow and fast flames. ....	84
Figure 38. Hydrogen concentrations corresponding to critical expansion ratio according to Eq. (5.21) as function of initial temperature. ....	85
Figure 39. Experimental detonation cell size at cryogenic temperature T=100K in comparison with the data at ambient temperature T = 293K. ....	88
Figure 40. Maximum combustion pressure for different hydrogen-air mixtures at cryogenic temperature T=100K in comparison with the data at ambient temperature T = 293K. ....	89
Figure 41. Chapman-Jouguet detonation pressure P_CJ and adiabatic combustion pressure Picc as a function of initial temperature for stoichiometric hydrogen-air mixture: open points – calculations by STANJAN code; dotted line – Eqs. (5.44-5.45). ....	90
Figure 42. Maximum combustion pressure for different hydrogen-oxygen mixtures at cryogenic temperature T=100K in comparison with the data at ambient temperature T = 293K. ....	91
Figure 43. Dynamic pressure as a function of flow velocity calculated for stoichiometric hydrogen air at two temperatures. ....	92
Figure 44. Maximum combustion pressure as function of characteristic flame velocity in obstructed and smooth tube: a) BR=0%; b) BR=30%; c) BR=60%. ....	92
Figure 45. Algorithm of solution for option 1: sonic deflagration in obstructed tube (BR=0.3). (*) Maximum possible combustion pressure can be evaluated here. ....	93
Figure 46. Algorithm of solution for option 2: detonation in obstructed tube (BR=0.3). (*)Maximum possible combustion pressure can be evaluated here. ....	96
Figure 47. Algorithm of solution for option 3: slow deflagration in obstructed tube (BR=0.6). (*)Maximum possible combustion pressure can be evaluated here. ....	97
Figure 48. Algorithm of solution for option 4: detonation in smooth tube (BR=0). (*)Maximum possible combustion pressure can be evaluated here. ....	99

## List of tables

Table 1. List of engineering correlations and tools.....	14
Table 2. Nomenclature for the similarity law. ....	17
Table 3. Input parameters for the similarity law. ....	19
Table 4. Output parameters for the similarity law. ....	19
Table 5. Nomenclature for the non-adiabatic blowdown model. ....	20
Table 6. Subscripts for the non-adiabatic blowdown model. ....	21
Table 7. Initial storage conditions of the 16 experimental tests used for validation of non-adiabatic blowdown model. ....	25
Table 8. Input parameters for the non-adiabatic blowdown model. ....	29

Table 9. Calculation algorithm for non-adiabatic blowdown model .....	29
Table 10. Output parameters for the non-adiabatic blowdown model.....	30
Table 11. List of available fictitious nozzle models. ....	33
Table 12. Relative error (%) of predicted mass flow rate against HSE experiments (positive means overestimation). .....	34
Table 13. Nomenclature of the tool to assess extent of cryogenic pools.....	37
Table 14. Comparison between experiments and predictions. ....	39
Table 15. Input parameters on the substrate characteristics. ....	40
Table 16. Input parameters of the LH <sub>2</sub> spill.....	41
Table 17. Output parameters for a given LH <sub>2</sub> spill.....	41
Table 18. Nomenclature in method for calculating the final state when mixing LH <sub>2</sub> and moist air. ....	42
Table 19. Elements of the enthalpy balance .....	43
Table 20. Coefficients of function to assess enthalpy of gaseous hydrogen. ....	45
Table 21. Coefficients of function to assess enthalpy of liquid hydrogen.....	45
Table 22. Coefficients of function to assess vapour pressure of water over ice.....	45
Table 23. Coefficients of function to assess enthalpy of air. ....	46
Table 24. Antoine coefficients for oxygen and nitrogen. ....	46
Table 25. Nomenclature for assessment of MIE.....	50
Table 26. Subscripts and superscripts.....	50
Table 27. Input parameters to determine MIE for hydrogen-air mixtures.....	55
Table 28. Output parameters for determination of MIE for hydrogen-air mixtures.....	55
Table 29. Nomenclature for the tool ElFiBU.....	57
Table 30. Input parameters for the ElFiBU-correlation and example of application. ....	60
Table 31. Output parameters for the ElFiBU-correlation and example of application.....	60
Table 32. Nomenclature for the assessment of combustion parameters.....	62
Table 33. Nomenclature for the dimensionless jet flame correlation. ....	65
Table 34. Input parameters for the dimensionless jet flame correlation.....	67
Table 35. Output parameters for the dimensionless jet flame correlation. ....	67
Table 36. Nomenclature for reduced model to evaluate radiative heat flux from a hydrogen jet fire. ....	69
Table 37. Experiments for the validation of the model to evaluate radiative heat flux. ....	72
Table 38. Input parameters and associated details.....	76
Table 39. Output parameters and associated details. ....	76
Table 40. Nomenclature for correlation on pressure load from delayed ignition of a turbulent jet.....	77
Table 41. Input parameters for the reduced model on delayed ignition of hydrogen jets. ....	80
Table 42. Output parameters for the reduced model on delayed ignition of hydrogen jets.....	80
Table 43. Nomenclature: FA and DDT for cryogenic hydrogen-air mixtures. ....	82
Table 44. Dimensionless scale for different processes. ....	85
Table 45. Critical ratios for DDT as function of blockage ratio. ....	86
Table 46. Main properties of hydrogen-air combustible mixtures at ambient temperature T=293K.....	90
Table 47. Input parameters for option 1: sonic deflagration in obstructed tube (BR=0.3).....	93
Table 48. Algorithm of solution for option 1: sonic deflagration in obstructed tube (BR=0.3). Steps 1, 2, 3.....	93
Table 49. Main properties of hydrogen-air combustible mixtures at cryogenic temperature T=100K.....	94
Table 50. Output values for option 1: sonic deflagration in obstructed tube (BR=0.3). ....	95
Table 51. Input values for option 2: detonation in obstructed tube (BR=0.3). ....	95

Table 52. Algorithm of solution for option 2: detonation in obstructed tube (BR=0.3). Steps 1, 2, 3.....	95
Table 53. Output values for option 2: detonation in obstructed tube (BR=0.3). .....	96
Table 54. Input values for option 3: slow deflagration in obstructed tube (BR=0.6).....	97
Table 55. Algorithm of solution for option 3: slow deflagration in obstructed tube (BR=0.6). Steps 1, 2, 3.....	97
Table 56. Output values for for option 3: slow deflagration in obstruced tube (BR=0.6).....	98
Table 57. Input values for option 4: detonation in smooth tube (BR=0).....	99
Table 58. Algorithm of solution for option 4: detonation in smooth tube (BR=0). Steps 1, 2, 3.....	99
Table 59. Output values for option 4: detonation in smooth tube (BR=0). .....	100
Table 60. Nomenclature for correlation on fireball size from LH <sub>2</sub> spills. ....	102
Table 61. Input parameters for the correlation on a fireball size. ....	103
Table 62. Output parameters for the correlation on a fireball size. ....	103
Table 63. Nomenclature.....	105
Table 64. Input parameters and associated details.....	106
Table 65. Output parameters and associated details. ....	106
Table 66. Standard units for calculation and storage in database. ....	107
Table 67. Alternative units for user inputs and outputs. ....	107

## 1 Introduction and scope

The present report gathers the engineering correlations and tools developed and validated within the technical work packages 3, 4 and 5. Experiments available in the literature or performed within PRESLHY research programme were used for either building semi-empirical and empirical correlations, or for the validation of theoretical models. The engineering correlations and tools aim at characterising the phenomena associated with cryogenic hydrogen and at assessing the hazards and consequences from likely accident scenarios. Where relevant and applicable, the engineering correlations and tools cover as well the range of temperatures close to ambient, to either assess if the models are suitable for the wider spectrum of temperatures, or to highlight the differences in behaviour of cryogenic and ambient temperature hydrogen.

The objectives of the deliverable are the following:

- Present the engineering correlations developed and validated within PRESLHY project to close the relevant knowledge gaps associated to cryogenic and liquid hydrogen safety and to calculate the hazard distances of relevant accident scenarios. Such engineering correlations will be fed into recommendations for Regulations, Codes and Standards.
- Provide the description of the engineering correlations and tools according to a unified template for future implementation into existing and/or future integrated platforms for hazards and risks assessment, e.g. the e-Laboratory developed within the ongoing project Net-Tools.

A first version of this document was presented in Milestone 29 “Detailed description of novel engineering tools for LH<sub>2</sub>”, delivered in December 2019. The document provided a first list of the envisaged engineering correlations to be developed during the project due course. However, in some cases, it has not proved possible to generate meaningful correlations for the associated sets of experiments or the plans were amended to address knowledge gaps deemed to be more relevant. Title of deliverable D6.5 “Detailed description of novel engineering correlations and tools for LH<sub>2</sub> safety, version 2” is slightly different from indication in GA, to include that the report will describe the developed tools as well. The description of tools based on CFD approaches is outside the scope of this report, and will be addressed in dedicated PRESLHY reports on computational studies (see PRESLHY D3.2, D4.2, D5.2).

### 1.1 Phenomena

The analysed phenomena reflect the generally accepted three pillars of explosion protection concept. They are investigated in the phenomena-oriented work packages WP3, WP4 and WP5, which are the core of the pre-normative research performed in PRESLHY. The phenomena are grouped as follows:

- Release and mixing (WP3): hazards associated with cryogenic and LH<sub>2</sub> releases, including but not limiting to: characterisation of steady state and transient hydrogen releases in a multiphase or gaseous state, assessment of extent and evaporation rate of LH<sub>2</sub> pools, and extent of a flammable cloud following a release, characterisation of the final state following mixing of cryogenic hydrogen and air.
- Ignition (WP4): ignition risks associated with situations unique to liquid hydrogen releases, where factors of cryogenic temperatures are significant. Areas of particular interest are: ignition potential at reduced temperature in the vapour phase, electrostatic charging in liquefied/multiphase mixtures.

- Combustion (WP5): hazards of LH<sub>2</sub> and cryogenic hydrogen combustion associated with conditions of 5-10 times higher density of combustible matters and different reactivity characteristics from hydrogen at atmospheric temperature. Attention is paid to thermal and pressure hazards from hydrogen jet fires, assessment of the laminar flame speed and expansion ratio, potential for flame acceleration and detonation transition, assessment of a fireball size following a LH<sub>2</sub> spill.

## 2 List of engineering correlations

The list of the engineering correlations and tools developed throughout the project is given in Table 1. The list was refined based on conclusions of the Phenomena Identification and Ranking Technique (PIRT) exercise (Task 2.3) and the refinement of the work programme (Task 2.4). The engineering correlations and tools are in total 13 and they are distributed as follows within the technical work-packages (WPs), thus per phenomena:

- **5** engineering tools associated to release and mixing phenomena (WP3);
- **2** engineering tools associated to ignition (WP4);
- **6** engineering tools associated to combustion (WP5).

**Table 1. List of engineering correlations and tools.**

N.	WP	Correlation title	Leading partner
1	3	The similarity law for concentration decay in momentum jets	UU
2	3	The non-adiabatic blowdown model for a hydrogen storage tank	UU
3	3	DISCHA tool, for physical properties and discharge calculations	NCSRD
4	3	Extent of cryogenic pools - HyPond	INERIS
5	3	Method for calculating the final state when mixing liquid hydrogen and moist air	HSE
6	4	Ignition Energy for hydrogen-air mixtures	UU
7	4	Electrostatic field-up generated during hydrogen releases	PS
8	5	Laminar burning velocity and expansion ratios for hydrogen-air mixtures	INERIS
9	5	Flame length correlation and hazard distances for jet fires	UU
10	5	Thermal load from hydrogen jet fires	UU
11	5	Maximum pressure load from delayed ignition of turbulent hydrogen jets	UU
12	5	Flame acceleration and detonation transition for cryogenic hydrogen-air mixtures	KIT
13	5	Fireball size after liquid hydrogen spill combustion	UU, KIT

### 2.1 Synergy and interconnections

The analyses conducted in WP2 “Technical Strategy and State-of-the-Art” were essential to identify the knowledge gaps and technological bottlenecks associated to cryogenic and liquid hydrogen applications, and to select the relevant phenomena and key accident scenarios to be addressed by PRESLHY research programme. These were the basis to build and refine the list of engineering correlations for the quantification of hazards and consequences from relevant accident scenarios (see Table 1).

The technical part of the research is given by WPs 3, 4 and 5, addressing the release and mixing, ignition and combustion phenomena, respectively. These WPs are the core for the development and validation of the engineering correlations and tools throughout the performed experimental, analytical and numerical studies.

The engineering correlations and tools presented in this document has fed the knowledge reported in D6.1 “Handbook of Hydrogen Safety: Chapter on LH<sub>2</sub> safety”. Furthermore, they have been implemented to provide the guidelines for safe design and operation of LH<sub>2</sub> infrastructure and the recommendations for RCSs, addressed in deliverables D6.2 and D6.3 respectively.

The engineering correlations developed within work-packages 3, 4 and 5 are interconnected. They may be used in synergy to provide a full spectrum of the expected hazards and consequences from an initiating event. An outlook and guidance through the interconnections of the engineering correlations and tools is given in Figure 1 and Figure 2 for two example scenarios. Figure 1 provides an outlook of the engineering correlations applicable to evaluate the hazards associated to pressurised cryogenic hydrogen releases, whereas the example given in Figure 2 is associated to liquid hydrogen spills.

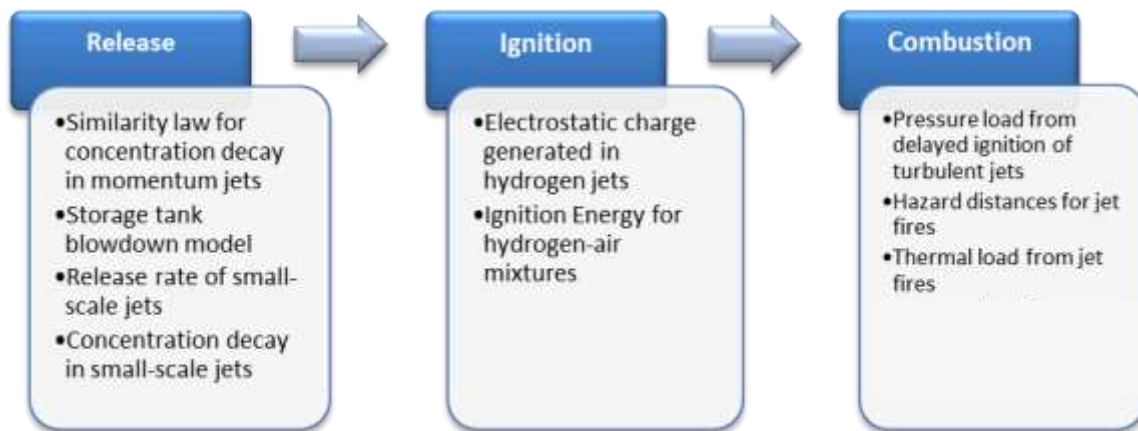


**Figure 1. Cryogenic gaseous hydrogen jet: outlook of the applicable engineering correlations to quantify associated hazards.**

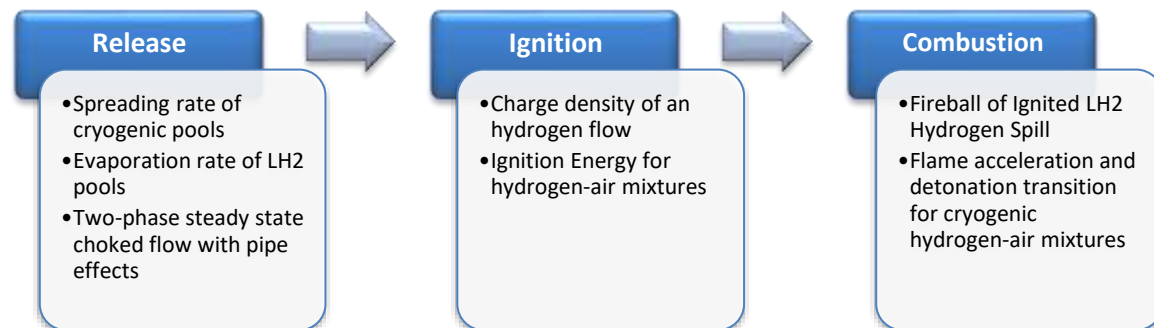


**Figure 2. Liquid hydrogen spill: outlook of the applicable engineering correlations to quantify associated hazards.**

## 2.2 Description of engineering correlations

The aims of this task include bringing the engineering correlations and tools developed within PRESLHY into a unified format suitable for programming and implementation into any existing and/or future integrated platforms for hazards and risks assessment, e.g. European e-Laboratory (ongoing NET-Tools project), HyRAM tool in USA, similar Canadian tool (UTRQ), etc. Each model description should report all the information required by a user to successfully use the correlation or tool. To this aim, a unified template to describe each correlation and tool was prepared in the early stage of the project. The

unified template is available in Appendix 1 and is designed in several sections covering the following points:

- Brief scientific summary;
- Validity range specifying the experimental data where relevant;
- A short user's manual which describes the input/output parameters and the detailed algorithm description for implementation in a software;
- Reference and/or link to publication.

Chapters on description of the engineering correlations will generally follow the template. Nevertheless, the template may be adapted to the specifics of the described engineering tool when deemed necessary. The level of detail of the model description or validation process may be variable depending on whether the study has been published yet. In case a study has already been published, the reader will be directed to the specific reference. Otherwise, the description and validation process will be shown in detail.

## 3 Release and mixing

This chapter presents the engineering correlations and tools developed for the evaluation of hazards associated to cryogenic, including liquid, hydrogen releases and their mixing with ambient air.

### 3.1 The similarity law for concentration decay in momentum jets (UU)

#### 3.1.1 Introduction

The similarity law for expanded and under-expanded jets aims at calculating the axial hydrogen concentration decay in cryogenic momentum-controlled jets. The similarity law can be used to estimate the distance from the nozzle where a concentration of interest is reached. For instance, the similarity law allows to calculate the location at which the Lower Flammability Limit (LFL) is reached (4%) to determine the axial size of the flammable envelope produced by an unintended hydrogen release.

#### 3.1.2 Nomenclature

Table 2 lists the nomenclature used throughout the model description.

**Table 2. Nomenclature for the similarity law.**

Parameter	Symbol	Unit
Hydrogen axial concentration	$C_{ax}$	-
Density of hydrogen at the nozzle	$\rho_N$	kg/m <sup>3</sup>
Density of the surroundings	$\rho_s$	kg/m <sup>3</sup>
Diameter	$d$	m
Distance	$x$	m
Froude number	$Fr$	-
Velocity at the nozzle	$u_N$	m/s
Gravity acceleration	$g$	m/s <sup>2</sup>

#### 3.1.3 Model description

The similarity law by (Chen and Rodi, 1980) is formulated as:

$$C_{ax} = 5.4 \sqrt{\frac{\rho_N}{\rho_s}} \frac{d}{x}, \quad (3.1)$$

where  $\rho_N$  is the density of hydrogen at the nozzle,  $\rho_s$  is the density of the surrounding air,  $d$  is the nozzle diameter and  $x$  is the distance from the release point.

For releases at pressure above 2 bar absolute an under-expanded jet is expected, as pressure at the nozzle exit is above atmospheric. Parameters at the real nozzle may be calculated by the under-expanded jet theory developed at Ulster (Molkov et al., 2009). The approach employs the Abel-Noble Equation of State (EOS) to describe the non-ideal behaviour of the gas at low temperatures and high-pressure. Release conditions are calculated assuming choked flow at the nozzle, isentropic expansion and conservation of energy between the stagnation and release locations. Cirrone et al. (2019) showed that for pressures up to 6 bar abs and temperature down to 46 K, Abel-Noble equation of state (EOS) can be used interchangeably with NIST EOS (Leachman et al., 2009). This conclusion was supported by calculations showing a maximum variation in the mass flow rate by 7%. Figure 3 shows the similarity law against experimental data reported in Molkov and Saffers (2013) and Hecht and Panda (2019). The same graph can be used as a graphical tool to retrieve the

hydrogen mass fraction at the distance x. Parameters at the real nozzle can be calculated as well by using e-Laboratory platform, available at the link <https://elab-prod.iket.kit.edu/>.

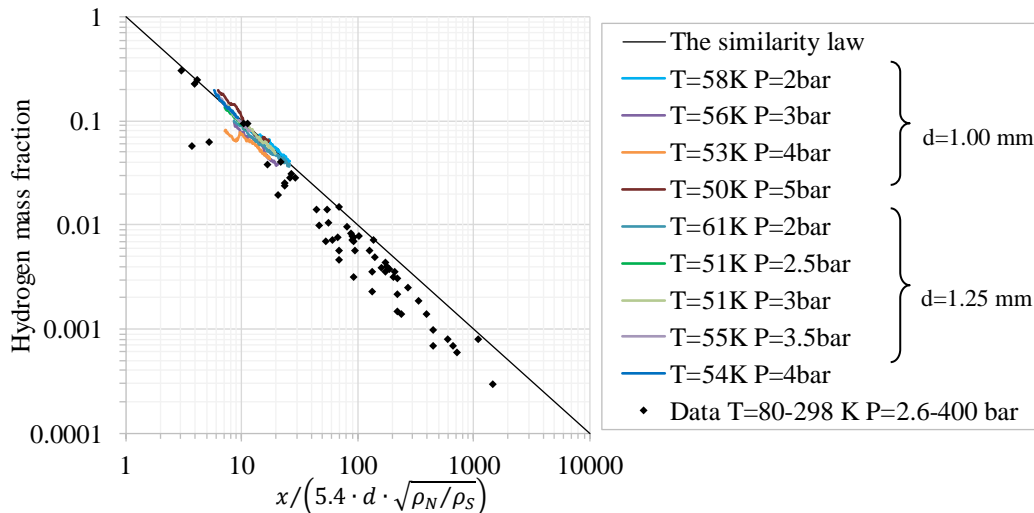


**Figure 3.** The similarity law and experimental data on axial concentration decay in momentum controlled expanded and under-expanded jets from Hecht and Panda's (2019) tests (solid lines) and data collected in Molkov and Saffers (2013) (diamonds).

The similarity law is valid for momentum-controlled jets. This assumption can be verified by calculating the Froude number as:

$$Fr = \frac{u_N^2}{gd}, \quad (3.2)$$

where  $u_N$  is the velocity at the nozzle and  $g$  is the gravity acceleration. Based on Molkov (2012) it can be concluded that jets are momentum controlled, at least up to the distance where hydrogen concentration 4% is reached, if Froude number logarithm is above 7.

The tool is available on e-laboratory platform developed within Net-Tools (<https://elab-prod.iket.kit.edu/>). Thanks to the studies performed within PRESLHY, this tool has been validated against releases at cryogenic temperature.

### 3.1.4 Validity range

The similarity law for concentration decay in momentum-dominated expanded jets (Chen and Rodi, 1980) was validated for under-expanded jets with release temperature down to 80 K and pressure in the range 2.6–400 bar if density at the real nozzle is calculated using Ulster's under-expanded jet theory (Saffers and Molkov, 2013). In the study by Cirrone et al. (2019), performed within PRESLHY, the similarity law validation was expanded to releases with temperature as low as 50 K for pressure in the range 2-5 bar abs (Hecht and Panda, 2019). Representation of experimental data on hydrogen concentration decay against the similarity law is given in Figure 3.

### 3.1.5 Input values

Table 3 reports the parameters required as input for the model. The column input value reports an example of calculations to test the tool once implemented on the platform.

**Table 3. Input parameters for the similarity law.**

Parameter	Symbol	Input value	Unit	Limits (min-max)	Defaults
Temperature in the storage	$T$	80	K	50-300	293
Pressure in the storage	$P$	$20 \cdot 10^6$	Pa	1-1000	350
Release diameter	$d$	0.00125	m	0.0001-0.2	0.002
Hydrogen axial concentration	$C_{ax}$	4%	-	4-75	4%
Ambient temperature	$T_{amb}$	288	K	233-313	293
Ambient pressure	$P_{amb}$	101325	Pa	33700-107900	101325

### 3.1.6 Output values

Table 4 reports the output parameters of the tool.

**Table 4. Output parameters for the similarity law.**

Parameter name	Symbol	Output value	Unit
Distance	$x$	10.6	m

### 3.1.7 Conclusions

The similarity law was used to develop an engineering tool for calculating the hydrogen concentration decay in momentum-controlled jets. This tool predicts the axial extension of hydrogen-air flammable envelopes by calculating the distance at which the LFL is reached.

### 3.1.8 References

- Chen, C. and Rodi, W. (1980), Vertical Turbulent Buoyant Jets - a review of experimental data, Pergamon Press, Oxford.
- Cirrone D., Makarov D., Molkov, V. (2019), Cryogenic hydrogen jets: calculation of hazard distances. International Conference on Hydrogen Safety, 24th-26th September 2019, Adelaide, Australia.
- Hecht, E. S. and Panda, P. P. (2018), Mixing and Warming of Cryogenic Hydrogen Releases, International Journal of Hydrogen Energy, pp. 1–11.
- Leachman, J.W., Jacobsen, R.T., Lemmon, E.W. (2009) Fundamental Equations of State for Parahydrogen, Normal Hydrogen, and Orthohydrogen, J. Phys. Chem. Ref. Data, Vol. 38, no. 3.
- Molkov, V. (2012), Fundamentals of Hydrogen Safety Engineering I, Free-download electronic book available at [www.bookboon.com](http://www.bookboon.com), 2012. Download free books at bookboon.com.
- Saffers, J. B. and Molkov, V. V. (2013), Towards Hydrogen Safety Engineering for Reacting and non-Reacting Hydrogen Releases, Journal of Loss Prevention in the Process Industries, vol. 26, no. 2, pp. 344–350.

## 3.2 The non-adiabatic blowdown model for a hydrogen storage tank (UU)

### 3.2.1 Introduction

During blowdown of pressurised hydrogen storage systems, temperature in the tank decreases due to the gas expansion. This process competes with the tendency of the gas temperature to increase due to the heat transfer through the tank wall. Study by (Schefer et al., 2007) highlighted the importance to include heat transfer effect on blowdown dynamics. This may further gain significance in the case of cryo-compressed storage tanks with a damaged insulation, affecting significantly parameters in the storage and at the nozzle. (Dadashzadeh et al., 2019) and (Molkov et al., 2021) developed and validated a non-adiabatic blowdown model accounting for heat transfer through the wall of high pressure hydrogen tanks. The under-expanded jet theory by (Molkov et al., 2009) was employed to calculate parameters at the real and notional nozzle exits.

Here, the theoretical model was further developed to extend its application and validation to cryo-compressed hydrogen. In this formulation, the non-ideal behaviour of cryogenic hydrogen is taken into account by using NIST EOS by implementing CoolProp database to evaluate hydrogen thermodynamic parameters (Bell et al., 2014). The blowdown model takes into account the conductive heat transfer through the tank wall by solving an unsteady heat transfer one dimensional equation. The model includes the convective heat transfer at the internal and external interfaces, i.e. hydrogen/wall and wall/external ambient, respectively, in either natural or forced convection regimes. Heat transfer coefficients are calculated through Nusselt correlations.

The tool allows to accurately predict the temperature and pressure dynamics in cryogenic hydrogen storages during blowdown. The inclusion of heat transfer through the release pipe leads to an accurate evaluation of hydrogen temperature, pressure and mass flow rate at the release nozzle. The tool has been validated against experiments performed within PRESLHY project with initial storage temperature of 300 K and 80 K and pressure up to 200 bar (PRESLHY D3.4, 2019). The model well represents pressure and temperature dynamics during blowdown for releases with diameter in the range 0.5-4 mm.

The tool may be implemented on calculation platforms such as Matlab, Python, Microsoft Excel, Fortran, etc, as they are all supported by CoolProp database libraries. For the study presented here, Matlab software was employed.

### 3.2.2 Nomenclature

Table 5 reports the nomenclature used in the non-adiabatic blowdown model and Table 6 reports the used subscripts to characterise the parameters.

**Table 5. Nomenclature for the non-adiabatic blowdown model.**

Parameter	Symbol	Unit
Area	$A$	m <sup>2</sup>
Diameter	$d$	m
Friction factor	$f$	-
Gravity acceleration	$g$	m/s <sup>2</sup>
Enthalpy	$h$	J/kg
Convective heat transfer coefficient	$k$	W/m <sup>2</sup> K
Length	$L$	m
Mass	$m$	kg
Prandtl number	$Pr$	-
Pressure	$P$	Pa

Heat transfer rate	$Q$	W
Temperature	$T$	K
Velocity	$v$	m/s
Internal energy	$U$	J
Volume	$V$	m <sup>3</sup>
Thermal expansion coefficient	$\beta$	1/K
Thermal conductivity	$\lambda$	W/mK
Density	$\rho$	kg/m <sup>3</sup>
Dynamic viscosity	$\mu$	Pa·s

**Table 6. Subscripts for the non-adiabatic blowdown model.**

Reference	Subscripts
Storage tank	$1$
Exit of discharge pipe prior to orifice	$2$
Real nozzle exit	$3$
Notional nozzle exit	$4$
External to the tank	$ext$
Internal to the tank	$int$
Tank	$tank$
Wall	$w$

### 3.2.3 Model description

The non-adiabatic blowdown model takes into account the non-ideal behaviour of hydrogen gas through the high-accuracy Helmholtz energy formulations (NIST) for mixture properties. This is done by implementing CoolProp database, which is an opensource C++ library implementing NIST EoS and transport properties for hydrogen (Bell et al., 2014). The database allows to calculate hydrogen parameters and properties by knowing two variables of its thermodynamic state.

The first law of thermodynamics is used to assess the change of storage conditions during blowdown. The rate of change of internal energy of hydrogen in the tank,  $U$ , is calculated from the rate of heat transfer  $Q$  to/from hydrogen through the tank wall and the rate of enthalpy exiting the tank by hydrogen outflow ( $h_{out}$ ):

$$\frac{dU}{dt} = \frac{dQ}{dt} - h_{out} \frac{dm}{dt}, \quad (3.3)$$

The rate of heat transfer by convection at the wall internal wall is calculated as:

$$\frac{dQ}{dt} = k_{int} A_{int} (T_{w(int)} - T_1), \quad (3.4)$$

where  $A_{int}$  is the internal area of the tank,  $T_{w(int)}$  is the temperature of the tank wall in contact with hydrogen,  $T_1$  is the temperature of hydrogen in the tank and  $k_{int}$  is the heat transfer coefficient at the internal tank wall.

#### 3.2.3.1 Convective heat transfer coefficient

The convective heat transfer inside the tank and within the discharge pipeline is calculated according to the convection regime: natural, combined or forced convection. The convection regime is defined according to the ratio of the Grashof number to Reynolds number and is used to determine the corresponding Nusselt number,  $Nu_{Din}$ . The convective heat transfer at the internal tank wall is calculated as:

$$k_{int} = \frac{\lambda_g \times N u_{Din}}{D_{int}}. \quad (3.5)$$

where  $\lambda_g$  and  $\mu_g$  are the hydrogen gas thermal conductivity ( $\frac{W}{mK}$ ) and dynamic viscosity (Pa·s). Detailed list of equations is given in (Molkov et al., 2019).

### 3.2.3.2 Change of internal energy in the tank

We can use the first law of thermodynamics differentiated in time to calculate the specific internal energy with advancement of time  $t + \Delta t$  from parameters calculated at the time step  $t$ :

$$u_1^{t+\Delta t} = (m_1^t u_1^t + \Delta t [k_{int}^t A_{int} (T_{w(int)} - T_1)^t - h_1^t \dot{m}_3^t]) / m_1^{t+\Delta t}, \quad (3.6)$$

where:  $m_1^{t+\Delta t} = m_1^t - \dot{m}_3^t \Delta t$ .

All parameters needed for determination of  $k_{int}^t$ , i.e.  $\beta, \mu_g, \lambda_g, c_{p,g}$ , are provided by CoolProp database for  $T_1^t$  and  $P_1^t$ . This allows to calculate  $u_1^{t+\Delta t}$ . The density of hydrogen in the tank at the time  $t + \Delta t$  is calculated as:

$$\rho_1^{t+\Delta t} = \frac{m_1^{t+\Delta t}}{V_{tank}}. \quad (3.7)$$

$u_1^{t+\Delta t}$  and  $\rho_1^{t+\Delta t}$  can now be used as input to CoolProp database to determine the thermodynamic state of hydrogen at the time  $t + \Delta t$ :  $T_1^{t+\Delta t}, P_1^{t+\Delta t}, h_1^{t+\Delta t}$ .

The following sections will show how to calculate the temperature at the tank wall,  $T_{w(int)}$ , and released mass flow rate of hydrogen  $\dot{m}_3^t$ .

### 3.2.3.3 Calculation of temperature at the wall: $T_{w(int)}$ and $T_{w(ext)}$

The model solves the unsteady heat conduction equation through a tank wall exposed on one side to hydrogen at temperature  $T_1$  and on the other side to external ambient temperature  $T_{ext}$ , as shown in Figure 4. Scheme of conjugate heat transfer at a tank wall. Figure 4. The 1-D heat conduction equation is expressed as follows (Patankar, 1980):

$$\rho_w c_{pw} \frac{dT_w}{dt} = \frac{d}{dx} \left( \lambda_w \frac{dT_w}{dx} \right). \quad (3.8)$$

where  $\rho_w, c_{pw}$  and  $\lambda_w$  are respectively the density, specific heat, thermal conductivity of the wall.

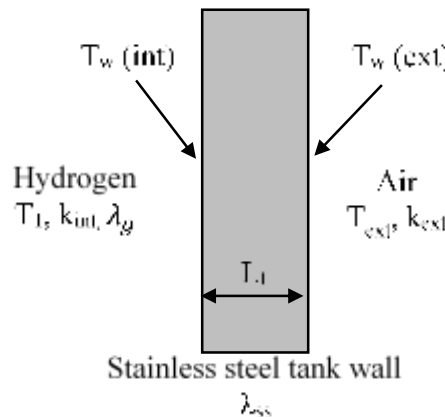


Figure 4. Scheme of conjugate heat transfer at a tank wall.

Full details on the model equations are given in (Dadashzadeh et al., 2019).

### 3.2.3.4 Heat transfer through the discharge line

CoolProp database implementing NIST EoS in (Bell et al., 2014) allows to calculate the thermodynamic state and properties of hydrogen by knowing two parameters of the fluid, given that it is in single-phase conditions. Therefore, they do not necessitate further considerations or expressions to determine the flow properties. For each time  $t$  of calculation,  $P_1$  and  $T_1$  are used to calculate  $\rho_1$ ,  $h_1$ ,  $s_1$ . If a discharge line between storage and nozzle is not insulated, heat transfer through the pipe wall may affect the flow parameters at the release nozzle, and for such release conditions close to the saturation line it may determine if the flow will be gaseous or multiphase. This model takes into account heat transfer in the release pipe with constant diameter (see Figure 5). The process is assumed to be isobaric, thus  $P_2 = P_1$ . The first and second law of thermodynamics are combined to assess the effect of heat transfer on the fluid properties:

$$dh = Q + vdp, \quad (3.9)$$

The heat transfer through the pipe is calculated through parameters for time step  $t$  as:

$$\frac{dQ}{dt} = k_{int\_pipe}^t A_{int\_pipe} (T_{w\_pipe}^t - T_2^t), \quad (3.10)$$

$T_{w\_pipe}^t$  is the temperature of the pipe wall, which in the present case is considered as constant to simplify the model.  $k_{int\_pipe}^t$  is the convective heat transfer coefficient calculated for either forced, combined, or natural convection as for the tank.  $A_{int\_pipe}$  is the internal surface of the pipe.  $T_2^t$  is the temperature at the exit of the pipe exchanging heat and is retrieved from the value at time step  $t$  to calculate the heat transfer that will affect the flow at time step  $t+\Delta t$ .

Finally, it is possible to use the energy conservation equation to retrieve the thermodynamic state  $h_2$  at the exit from the pipe:

$$h_2 + \frac{v_2^2}{2} = q + h_1, \quad (3.11)$$

where:  $v_2 = \dot{m}_3^t / (A_{int} \rho_2)$ , and  $q = \frac{dQ}{dt} / \dot{m}_3^t$ .

$P_2$  and  $h_2$  are used as input to CoolProp database to estimate:  $T_2$ ,  $s_2$  and  $\rho_2$ .

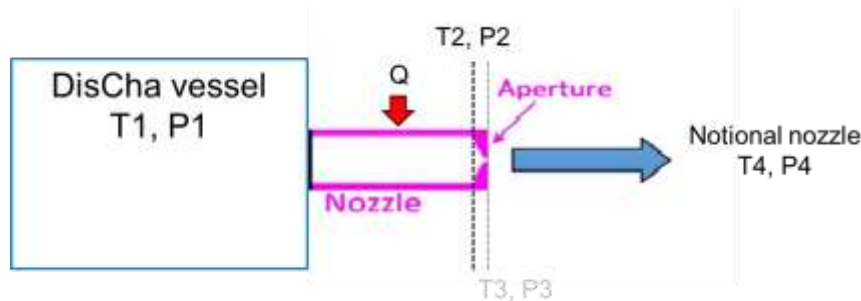


Figure 5. Scheme of under-expanded jet: 1 – storage tank; 2 – end of pipe prior to restrictor; 3- real nozzle exit; 4 – notional nozzle exit.

### 3.2.3.5 Under-expanded jet theory

After flowing in the pipe, the hydrogen flow undergoes an isentropic expansion at the real nozzle, i.e.  $s_3 = s_2$ . The flow here is assumed to be sonic. The equation for conservation of energy was employed to calculate conditions at the real nozzle exit as follows:

$$h_3 - h_2 + \frac{v_3^2}{2} = 0, \quad (3.12)$$

Resolution of the equation for energy conservation employs an iterative algorithm. Temperature is gradually decreased by a certain  $\Delta T$  along the isentropic expansion transformation from the “storage” conditions  $s(T, P) = s_2(T_2, P_2)$ . For each iteration  $n$ , enthalpy,  $h_3^n(T_3^n, s_3 = s_2)$ , and speed of sound,  $v_3^n(T_3^n, s_3 = s_2)$  at the real nozzle exit are determined by the CoolProp database by using two parameters  $s_3 = s_2$  and  $T_3^n$ , i.e. the temperature at the iteration  $n$ . At each iteration  $n$  we will have the energy conservation equation as follows, until a solution is found:

$$h_3^n - h_2 + \frac{(v_3^n)^2}{2} = diff^n, \quad (3.13)$$

The algorithm is stopped when the equation of energy conservation is satisfied with a given tolerance. This may depend on the particular problem, and for the present case a good compromise between solution accuracy and calculation time was found for  $toll=0.1\text{ kJ/kg}$  and  $\Delta T=0.001\text{ K}$ . The temperature  $T_3^{end}$  providing the resolution of the equation for energy conservation describes the status of the jet at the real nozzle exit. Knowing  $T_3$  and  $s_3$ , it is possible to determine from the CoolProp database all other properties of interest, i.e.  $v_3$ ,  $P_3$  and  $\rho_3$ . The mass flow rate is calculated as  $\dot{m}_3 = \rho_3 v_3 A_3$ .

In case of absence of a discharge pipe or its vacuum insulation, the model can be amended to evaluate direct expansion from storage to nozzle.

An additional feature of the model may be the implementation of the algorithm to evaluate notional nozzle conditions for application in numerical simulations. The expansion of the flow to ambient pressure ( $P_4 = P_{amb}$ ) assumes the conservation of energy and speed of sound at the notional nozzle exit:

$$h_3 + \frac{v_3^2}{2} = h_4 + \frac{v_4^2}{2}. \quad (3.14)$$

Also in this case, an iterative algorithm as per expansion from storage to the real nozzle exit is used: temperature  $T_4$  is varied iteration after iteration with a certain  $\Delta T$ . For each iteration  $n$ , the speed of sound  $v_4^n(T_4^n, P_4)$  is calculated from CoolProp database. The parameters are substituted in the equation above and the process is repeated until the balance is satisfied within a given tolerance (0.1 kJ/kg).

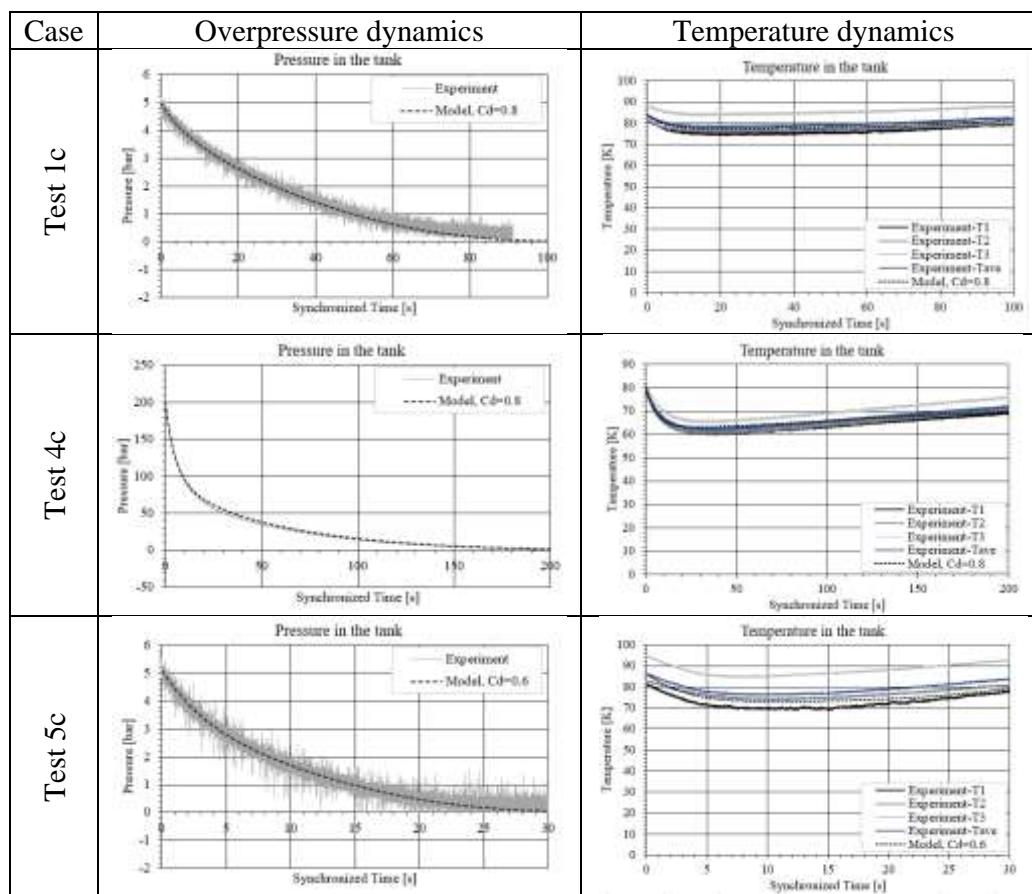
### 3.2.4 Validity range

Tests from DiScha experimental campaign performed by Pro-Science within PRESLHY project (Friedrich et al., 2019) were employed here for validation of the non-adiabatic blowdown model. The tank was made of stainless steel and had volume 2.81 dm<sup>3</sup>. The tank was exposed to ambient temperature air for the ambient temperature releases. External heat transfer coefficient was considered equal to 6 W/m<sup>2</sup>K (Dadashzadeh et al., 2019). In the case of cryogenic releases, the tank was immersed in a liquid nitrogen bath with temperature equal to 77 K. External heat transfer coefficient for LN2 was considered equal to 120 W/m<sup>2</sup>K (Wang et al., 2015). In this case the only portion of pipe exposed to ambient air was 55 mm long. The temperature of the pipe wall was taken from experiments. A discharge coefficient was applied to take into account pressure and friction losses in the system. Sixteen tests out of the available forty-four experiments were selected to maximize the validation range of the tool: initial storage pressure = 5-200 bar, initial storage temperature=80-300 K, release nozzle diameter= 0.5-4 mm. Table 7 presents the storage conditions and nozzle diameter for each of the validation tests.

**Table 7. Initial storage conditions of the 16 experimental tests used for validation of non-adiabatic blowdown model.**

Cryogenic temperature releases, $T_s \approx 80$ K			Ambient temperature releases, $T_s \approx 300$ K		
Test No.	D <sub>nozzle</sub> , mm	P <sub>s</sub> , bar	Test No.	D <sub>nozzle</sub> , mm	P <sub>s</sub> , bar
1c	0.5	5	1w	0.5	5
4c	0.5	200	4w	0.5	200
5c	1	5	5w	1	5
8c	1	200	8w	1	200
9c	2	5	9w	2	5
15c	2	200	15w	2	200
16c	4	5	16w	4	5
22c	4	200	22w	4	200

The overpressure and temperature dynamics measured in experiments were used to validate the model. Figure 6 shows the comparison between calculations and experiments for the cryogenic hydrogen releases with different discharge coefficients. Figure 7 shows results for ambient temperature releases. Calculated temperature is compared to three measurements at different heights within the tank (T1, T2, T3), performed via type K thermocouples with a stainless steel sensitive tip (hereby indicated as “closed” thermocouple), and the average value among the three experimental record (Tave).



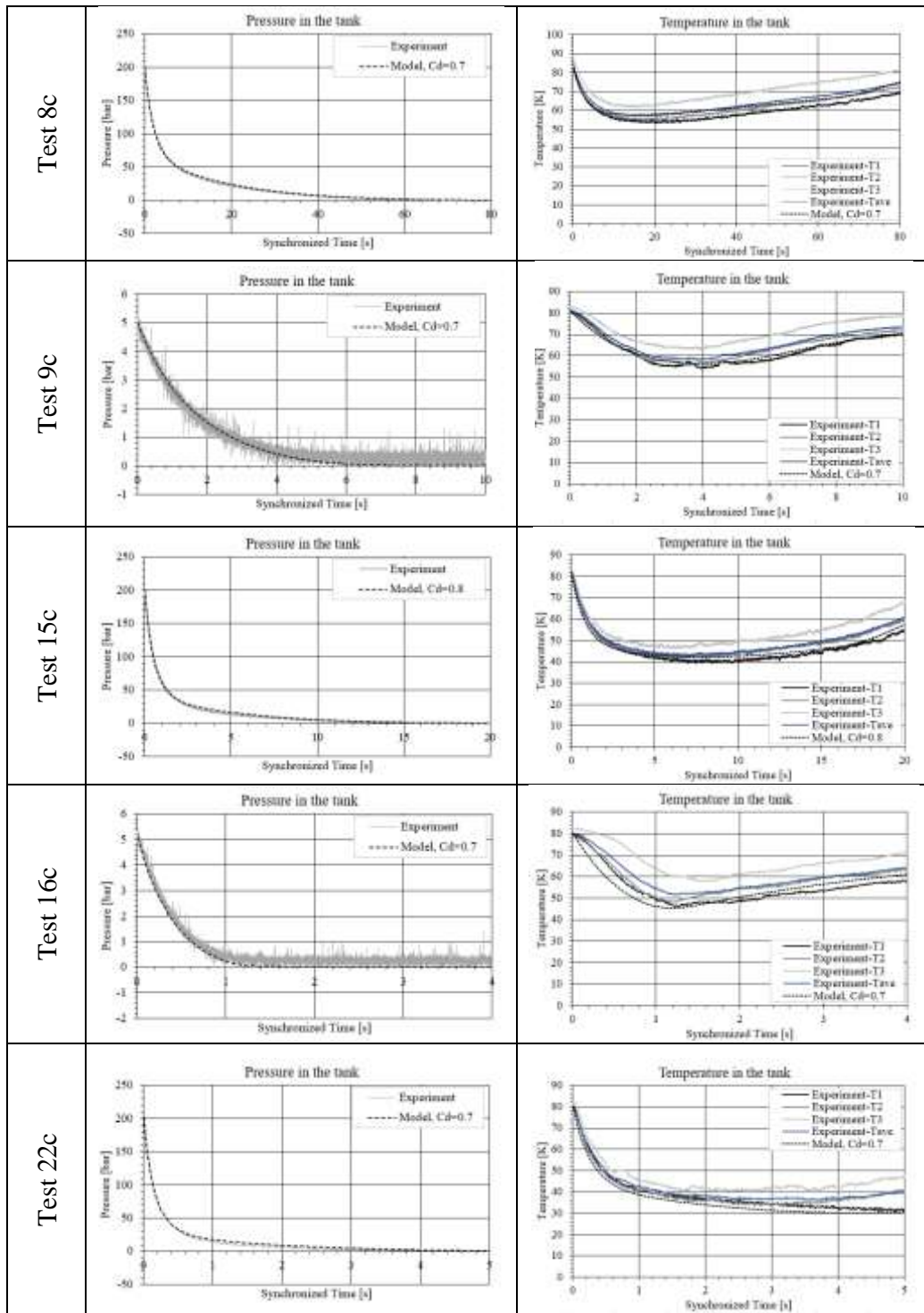
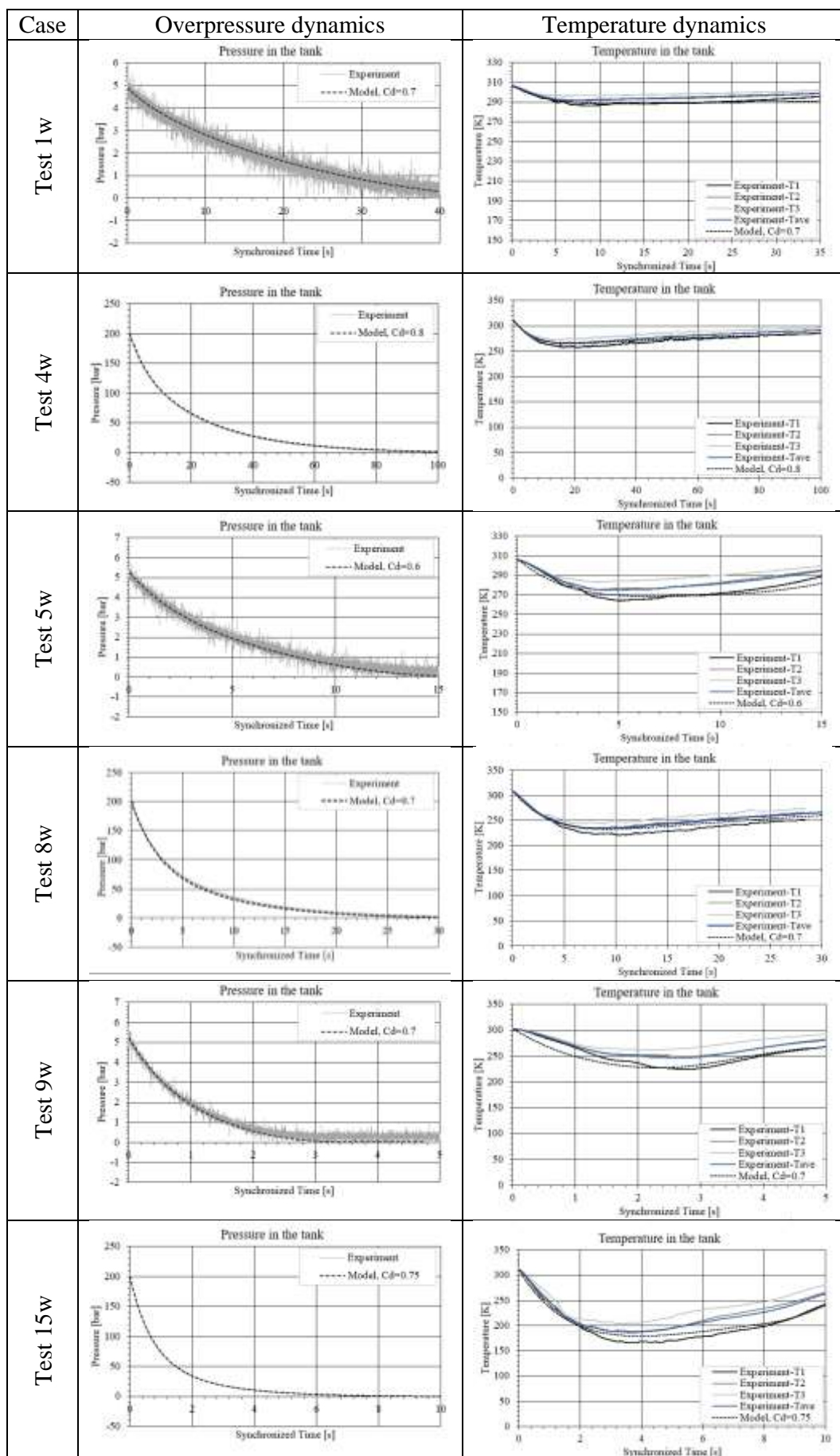
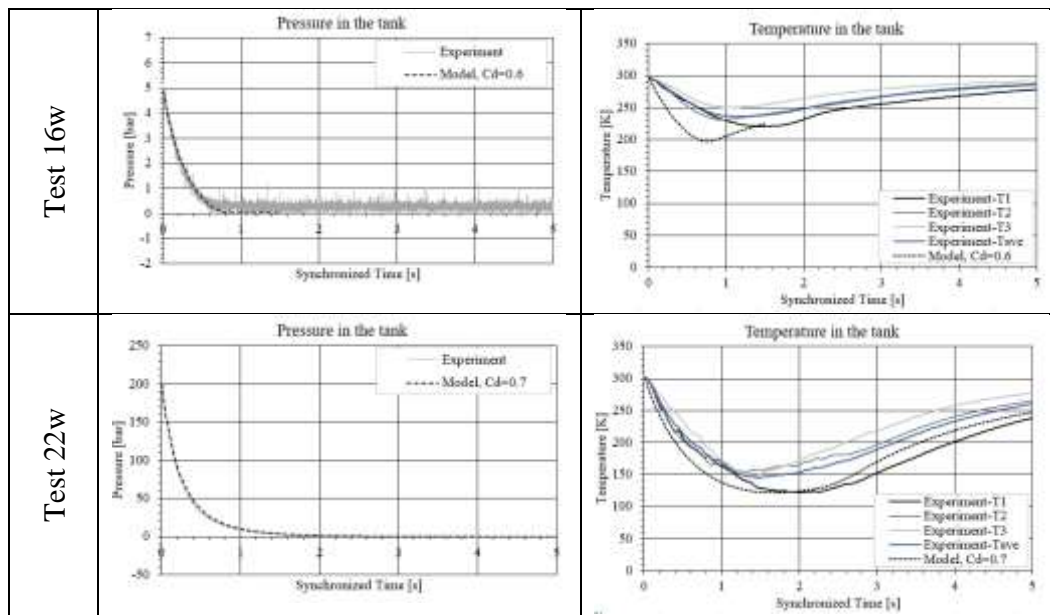


Figure 6. Validation of non-adiabatic blowdown model against cryogenic temperature releases.





**Figure 7. Validation of non-adiabatic blowdown model against ambient temperature releases.**

Predictions of pressure and temperature dynamics in the storage tank agree well with experimental measurements. Few exceptions are given by the releases with larger diameter, e.g. test 16w with diameter equal to 4 mm, initial storage pressure of 5 bar and temperature equal to ambient. This deviation was thought to be caused by the experimental thermocouples' inertia being comparable with the blowdown duration. This is supported by experimental evidences, as Test 16w is one of the tests showing largest difference in temperature measurements by the “closed” and “open” thermocouples used in experiments. “Open” thermocouples had the stainless-steel sensitive tip removed, decreasing the thermocouple inertia but as well reducing measurements accuracy for cryogenic temperatures. Figure 8 shows the comparison between the predicted temperature in the tank and experimental measurements by the two thermocouple types. It could be seen that for the “open” thermocouples there is better agreement with the model, as the sensors inertia is reduced considerably for such a short blowdown duration.

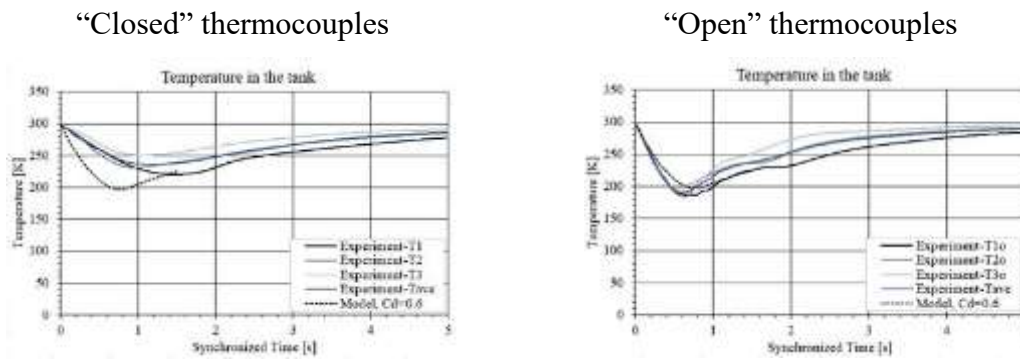


**Figure 8. Temperature dynamics for Test 16w: “closed” versus “open” thermocouples measurements.**

### 3.2.5 Input values

Table 8 reports the parameters required as input for the model. The column input value reports an example of calculations to test the tool once implemented on the platform.

**Table 8. Input parameters for the non-adiabatic blowdown model.**

Parameter	Symbol	Input value	Unit	Limits (min-max)	Defaults
Temperature in the storage	$T_1$	80	K	80-300	288
Pressure in the storage	$P_1$	$20 \cdot 10^6$	Pa	$2 \cdot 10^5$ - $2 \cdot 10^6$	$2 \cdot 10^6$
Release diameter	$d_n$	0.001	m	0.5-4.0	0.002
Discharge coefficient	$C_d$	0.7	-	0.1-1	1.0
Volume of the storage tank	$V_{tank}$	0.002815	$m^3$	0.002-0.300	0.0028
Tank internal diameter	$D_{int}$	0.16	m	0.14-0.5	0.16
Tank internal height	$H_{int}$	0.14	m	0.14-0.5	0.14
Tank thickness	$L_t$	0.03	m	0.01-0.1	0.03
Tank material specific heat	$c_{p,w}$	200	J/kgK	10-1000	500
Tank material thermal conductivity	$\lambda_w$	9	W/mK	0.01-100	16.3
Tank material density	$\rho_w$	8000	kg/m <sup>3</sup>	100-8000	8000
Release pipe diameter	$d_{pipe}$	0.010	m	0.0005-0.010	0.010
Release pipe length	$L_{pipe}$	0.055	m	0.0	0.055
Time step	$\Delta t$	0.01	s	0.001-0.2	0.01
Nodes for spatial discretization	$n$	20	-	10-100	20
External heat transfer coefficient	$k_{ext}$	120	W/m <sup>2</sup> K	1-400	6
External temperature	$T_{ext}$	77	-	233-313	293
Ambient pressure	$P_{amb}$	101325	Pa	33700-107900	101325

### 3.2.6 Calculation procedure

At the beginning of calculations (time=Δt), parameters at the release nozzle are initialised by applying the under-expanded jet theory without inclusion of heat transfer. The calculated hydrogen mass flow rate and velocity are used as input to calculate the heat transfer rate exchanged through the pipe wall and the associated hydrogen mass flow rate. Afterwards, the calculation proceeds as described in Table 9.

**Table 9. Calculation algorithm for non-adiabatic blowdown model.**

Step	Calculation algorithm until $P_1/P_{amb} > P_{lim}$
1	Hydrogen mass in the tank
2	Convective heat transfer in the hydrogen tank: section 3.2.3.1
3	Change of internal energy to find storage parameters at time $t+\Delta t$ : section 3.2.3.2
4	Temperature distribution across the tank wall: see section 3.2.3.3
5	Heat transfer rate through the discharge pipe wall: see section 3.2.3.4
6	Calculate real nozzle exit parameters: see section 3.2.3.5

### 3.2.7 Output values

Table 10 reports the output parameters of the tool. Given the transient nature of the tool, it is not possible to provide full table with time history. Please see Figure 6-Test 8c for pressure and temperature dynamics to be used for verification of a tool.

**Table 10. Output parameters for the non-adiabatic blowdown model.**

Parameter	Symbol	Output value	Unit
Tank temperature	$T_1$	Time history	K
Tank pressure	$P_1$	Time history	Pa
Tank density	$\rho_1$	Time history	kg/m <sup>3</sup>
Hydrogen mass flow rate	$\dot{m}_3$	Time history	kg/s
Real nozzle temperature	$T_3$	Time history	K
Real nozzle pressure	$P_3$	Time history	Pa
Real nozzle density	$\rho_3$	Time history	kg/m <sup>3</sup>
Real nozzle velocity	$u_3$	Time history	m/s

### 3.2.8 Conclusions

The non-adiabatic blowdown model allows an accurate prediction of the temperature and pressure dynamics in a pressurised storage tank during blowdown by taking into account the conjugate heat transfer through the tank wall. In this formulation, the non-ideal behaviour of cryogenic hydrogen is taken into account using NIST EOS by implementing CoolProp database to evaluate hydrogen thermodynamic parameters. The under-expanded jet theory by (Molkov et al., 2009) was employed to calculate parameters at the real and notional nozzle exits. The tool has been validated against numerous tests performed within PRESLHY project on transient releases from pressurised hydrogen storages at cryogenic and ambient temperature.

### 3.2.9 References

- Bell, I.H., Wronski, J., Quoilin, S. and Lemort, V. (2014), Pure and Pseudo-pure Fluid Thermophysical Property Evaluation and the Open-Source Thermophysical Property Library CoolProp, Industrial & Engineering Chemistry Research, Vol. 53 No. 6, pp. 2498–2508.
- PRESLHY D3.4 (2019), PRESLHY - D3.4 Summary of Experiment Series E3.1 (Discharge) Results – Part A High Pressure.
- Dadashzadeh, M., Makarov, D., Kashkarov, S. and Molkov, V. (2019), Non-adiabatic under-expanded jet theory for blowdown and fire resistance rating of hydrogen, International Conference on Hydrogen Safety, Adelaide, Australia.
- Friedrich, A., Veser, A. and Jordan, T. (2019), PRESLHY - D3.4 Summary of Experiment Series E3.1 (Discharge) Results.
- Molkov, V., Dadashzadeh, M., Kashkarov, S. and Makarov, D. (2021), Performance of hydrogen storage tank with TPRD in an engulfing fire, submitted to: Int. J. Hydrot. Energy.
- Molkov, V., Dadashzadeh, M. and Makarov, D. (2019), Physical model of onboard hydrogen storage tank thermal behaviour during fuelling, International Journal of Hydrogen Energy, Elsevier Ltd, Vol. 44 No. 8, pp. 4374–4384.
- Molkov, V., Makarov, V. and Bragin, M. V. (2009), Physics and modelling of underexpanded jets and hydrogen dispersion in atmosphere, Physics of Extreme States of Matter, pp. 146–149.
- Patankar, S. (1980), Numerical Heat Transfer and Fluid Flow: Computational Methods in

Mechanics and Thermal Science, Hemisphere Publication Corporation, Washington, DC.

Schefer, R.W., Houf, W.G., Williams, T.C., Bourne, B. and Colton, J. (2007), Characterization of high-pressure, underexpanded hydrogen-jet flames, International Journal of Hydrogen Energy, Vol. 32, pp. 2081–2093.

Wang, T., Zhao, G., Tang, H. and Jiang, Z. (2015), Determination of convective heat transfer coefficient at the outer surface of a cryovial being plunged into liquid nitrogen, Cryo-Letters, Vol. 36 No. 4, pp. 285–288.

### 3.3 DISCHA tool, for physical properties and discharge calculations (NCSRD)

#### 3.3.1 Introduction

DISCHA tool can be applied to calculate accurate physical properties of pure substances and perform discharge calculations either in transient (blowdown) or steady state mode with account of discharge line.

#### 3.3.2 Model description

##### 3.3.2.1 Physical properties and phase-change model

Single phase physical properties and vapor-liquid equilibrium for normal hydrogen and para-hydrogen are modeled using the Helmholtz Free Energy (HFE) formulation of (Leachman et al., 2009). Similar HFE formulations from literature are used for other substances (CH<sub>4</sub>, H<sub>2</sub>O, CO<sub>2</sub>).

Physical properties within the two-phase regime are by default modeled using the Homogeneous Equilibrium Mixture (HEM) model as in (Venetsanos, 2018). Homogeneous Non-Equilibrium (HNEM) formulations to be applied in the bubbly two-phase regime have also been implemented and tested.

##### 3.3.2.2 Tank model

In the present version of the tool thermal equilibrium is assumed inside the tank, i.e. in case of two-phase conditions both phases sharing same pressure and temperature. Non-equilibrium two-phase conditions will be provided in future versions of the tool.

The tank stagnation conditions (temperature, pressure, vapor quality) versus time can either be read from files or calculated from the following tank mass and energy (specific entropy) conservation equations, where  $\rho$ ,  $s$  are the tank averaged density and entropy,  $V$ ,  $A$  the tank free volume and its enclosing internal surface,  $\dot{m}$  the mass flow rate into the discharge line,  $\dot{q}$  the heat flux through  $A$ .

$$V \frac{d\rho}{dt} = -\dot{m} \quad (3.15)$$

$$V \frac{d\rho s}{dt} = -\dot{m}s + \frac{\dot{q}A}{T} \quad (3.16)$$

In the present version of the tool tank heat flux is not modeled but provided as input. Tank heat flux modeling will be provided in future versions of the tool. In case of zero heat flux (adiabatic tank) the entropy equation combined with the mass balance equation lead to the condition that tank entropy remains constant during a blowdown.

### 3.3.2.3 Pipe flow model

The model finds the choked (maximum) mass flow rate  $\dot{m}$  satisfying the 1-D steady state pipe conservation equations of mass, momentum and energy along the entire length of the discharge line:

$$u = \frac{\dot{m}}{\rho A} \quad (3.17)$$

$$\frac{\dot{m}^2}{A} d\left(\frac{1}{\rho A}\right) = -dP - \frac{\dot{m}^2 dx}{2\rho A^2} \left(\frac{f_D}{D} + \frac{K}{L}\right) \quad (3.18)$$

$$d\left(h + \frac{u^2}{2}\right) = \dot{q} \frac{4dx}{\rho u D} \quad (3.19)$$

In the equations above  $\rho$  is the density,  $u$  the velocity,  $dx$  is the step along the line,  $A$ ,  $D$  the flow cross section and discharge line internal diameter (considered variable along the line),  $h$  the enthalpy,  $f_D$  the Darcy friction factor,  $L$  is the length over which the extra resistance factor  $K$  applies (different line sections may have different values of  $K$ ) and  $\dot{q}$  is the heat flux at the internal wall. Darcy friction factor is calculated from Colebrook's equation for rough walls. Resistance factors must be prescribed by the user. Gravity effects are neglected.

### 3.3.2.4 Pipe wall heat transfer model

Heat flux at pipe internal wall is calculated by solving the one-dimensional energy conservation equation inside the discharge line walls given below, Subscripts ‘in’ and ‘ex’ refer to the internal and external surface of the discharge line respectively, subscript ‘w’ refers to wall material, subscript ‘amb’ refers to ambient conditions,  $T_w$  is the thickness averaged wall temperature,  $a$  is the heat transfer coefficient, and  $\lambda, \rho, c_p$  the wall material conductivity, density and specific heat respectively. Heat transfer coefficient between flow and internal wall is calculated using the Reynolds analogy. External heat transfer coefficient is prescribed by the user.

$$\rho_w c_{Pw} \left( \frac{D_{ex}^2 - D_{in}^2}{4} \right) \frac{dT_w}{dt} = \dot{q}_{ex} D_{ex} - \dot{q}_{in} D_{in} \quad (3.20)$$

$$\dot{q}_{ex} = \frac{\lambda_w a_{ex}}{\lambda_w + a_{ex} \Delta D / 2} (T_{amb} - T_w), \quad \dot{q}_{in} = \frac{\lambda_w a_{in}}{\lambda_w + a_{in} \Delta D / 2} (T_w - T) \quad (3.21)$$

### 3.3.2.5 Fictitious nozzle models

In case of choked flow conditions at the real nozzle exit the tool can calculate the expanded conditions at the fictitious nozzle using 7 different fictitious nozzle models from the literature as shown in the table below. All models assume mass preservation between nozzle and fictitious nozzle. Two choices are available for momentum: either to apply a Ma = 1 condition at the fictitious nozzle or use momentum balance to connect nozzle and fictitious nozzle. Four choices are available for energy: a) adiabatic (i.e. total enthalpy constant between nozzle and fictitious nozzle), b) assume ambient temperature at the fictitious nozzle, c) assume fictitious nozzle temperature is equal to the real nozzle temperature and d) assume entropy is constant between real and fictitious nozzle.

**Table 11. List of available fictitious nozzle models.**

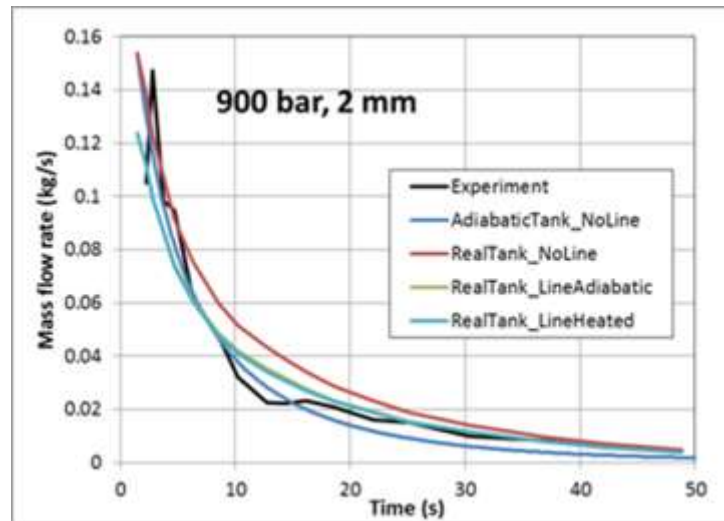
<b>Model id</b>	<b>Mach=1</b>	<b>Momentum balance</b>	<b>Adiabatic</b>	<b>Ambient temperature</b>	<b>Isothermal</b>	<b>Isentropic</b>
1	✓			✓		
2	✓				✓	
3	✓		✓			
4		✓		✓		
5		✓			✓	
6		✓	✓			
7		✓				✓

### 3.3.3 Validity range

The tool was validated against:

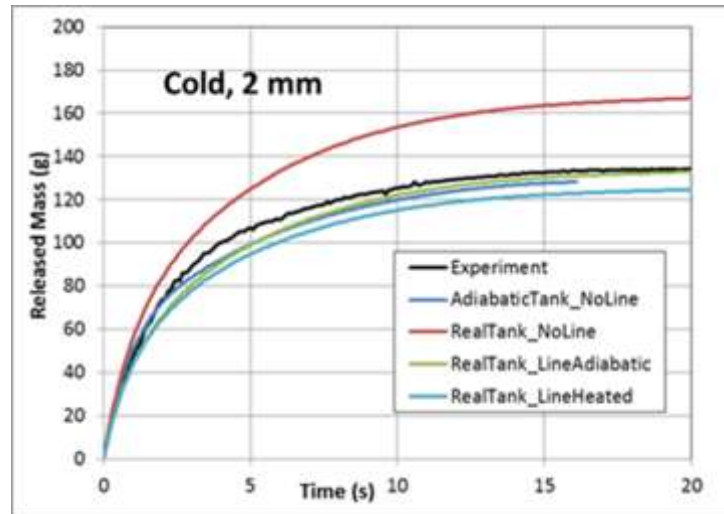
- NASA cryogenic hydrogen critical flow experiments (22 tests) with elliptical converging-diverging nozzle @12.9-58.9 bar, 27.2-32.3 K, see (Venetsanos and Giannissi, 2017) and (Venetsanos, 2018).
- KIT-2012 cryogenic hydrogen experiments @ $1.02 < T_0/T_{cr} < 1.96$  and  $0.54 < P/P_{cr} < 2.7$ , with 1 and 0.5 mm nozzles, see (Venetsanos and Giannissi, 2017).
- Super Moby Dick experiments with liquid water @20 bar, 212.3 C with a variable cross section discharge line (minimum diameter 2 cm) and length of approximately 0.6m, see (Venetsanos, 2019).
- DISCHA CGH2 experiments, @200 bar, cold (80 K) and warm (ambient temp.), 2.815 dm<sup>3</sup> steel tank, 39 cm line, 9 mm ID ending to 0.5, 1, 2 and 4 mm ID nozzles, see (Venetsanos et al. 2021a).
- INERIS CGH2 blowdown experiments, @900 bar, ambient temperature, 25 dm<sup>3</sup> type-IV tank, 10 m line, 10mm ID ending to a 2 mm ID nozzle, see (Venetsanos et al. 2021a).
- HSE LH<sub>2</sub> experiments, @2 and 6 bara, 23 m line, 1 inch ID and 1, 1/2, 1/4 inch ID nozzles, see (Venetsanos et al. 2021b)

Figure below shows predicted hydrogen mass flow rate against experimental for INERIS CGH2 blowdown experiments. Predictions were made with or without a discharge line and either assuming an adiabatic tank or reading the experimental stagnation conditions versus time from a file (real tank calculation).



**Figure 9.** Blowdown calculations against INERIS test, see (Venetsanos et al. 2021a).

Figure below shows predicted released hydrogen mass against experimental for DISCHA blowdown experiment by PS/KIT @200bar, 80K, 2.815 dm<sup>3</sup> steel tank, 39 cm line, 9 mm ID ending to 2 mm ID nozzle. Predictions were made with or without a discharge line and either assuming an adiabatic tank or reading the experimental stagnation conditions versus time from a file (real tank calculation).



**Figure 10.** Blowdown calculations against DISCHA-PS/KIT test, see (Venetsanos et al. 2021a).

Table below shows relative error between predicted and experimental mass flow rate for the HSE LH<sub>2</sub> experiments performed within PRESLHY. Simulations were performed with three different phase change models, see also (Venetsanos et al., 2021b).

**Table 12.** Relative error (%) of predicted mass flow rate against HSE experiments (positive means overestimation).

Nozzle diameter (mm)	2 bara			6 bara		
	Const density	HNEM	HEM	Const density	HNEM	HEM
25.4	3.4	3.3	1.9	9.0	8.5	7.1
12.7	11.6	11.5	7.9	0.1	-0.3	-3.3
6.35	-	-	-	13.4	12.7	9.6

### 3.3.4 Input values

The following parameters are required as input to the model:

- Tank volume.
- Tank initial thermodynamic state defined using pressure, temperature and vapor quality or tank states versus time from a file.
- Tank heat flux and tank area if (heat flux is non-zero).
- Ambient pressure (back pressure) and temperature.
- Number of pipe sections forming the discharge line.
- For each pipe section:
  - Inlet and outlet diameter (can be different to account for variable cross section);
  - Length;
  - Relative wall roughness;
  - Resistance factor K or equivalent L/D;
  - Discretization characteristics (e.g. number of steps, minimum step, expansion / contraction ratio);
  - Wall thickness;
  - Wall material properties (density, heat capacity, thermal conductivity);
  - External heat transfer coefficient (between external wall and ambient).
- Fictitious nozzle model (if results at fictitious nozzle are required).

### 3.3.5 Calculation procedure (possible algorithm)

Calculation procedure is described in (Venetsanos, 2019) and (Venetsanos et al., 2021a, b).

#### 3.3.5.1 Mass flow rate calculation

First choked flow is calculated using the Possible Impossible Flow (PIF) iterative maximization procedure, with inlet pressure as iteration variable. For given inlet pressure, other inlet conditions and mass flow rate are calculated assuming isentropic expansion from the known stagnation conditions, as in (Venetsanos, 2018). With given mass flow rate, discharge line equations (discretized along the line, see below) are solved step by step towards line exit until either non-possible flow is encountered at given step or given mass flow rate is possible throughout the line. If the first condition is reached inlet pressure is increased in the next PIF iteration and the opposite for the second condition. The above PIF procedure is general and once fine line discretization is used near the nozzle exit (minimum cross section) it produces (as output) Mach equal to one at the exit for under-expanded flow.

#### 3.3.5.2 Pipe step calculation

Pipe differential conservation equations are discretized over step  $\Delta x$  along the discharge line from upstream location 1 to downstream location 2 as follows:

$$\rho_1 u_1 A_1 = \rho_2 u_2 A_2 = \dot{m} \quad (3.22)$$

$$\frac{\dot{m}^2}{A_{12}} \left( \frac{1}{\rho_2 A_2} - \frac{1}{\rho_1 A_1} \right) = P_1 - P_2 - \frac{\dot{m}^2}{A_{12}} \frac{1}{2} \left( \frac{1}{\rho_1 A_1} + \frac{1}{\rho_2 A_2} \right) \frac{\Delta x}{2} \left( \frac{f_D}{D_{12}} + \frac{K}{L} \right) \quad (3.23)$$

$$h_1 + \frac{1}{2} \left( \frac{\dot{m}}{\rho_1 A_1} \right)^2 = h_2 + \left( \frac{\dot{m}}{\rho_2 A_2} \right)^2 + \dot{q} \frac{4 \Delta x}{\rho u D} \quad (3.24)$$

$$A_{12} = \frac{2A_1 A_2}{A_1 + A_2}, \quad D_{12} = 2\sqrt{A_{12}/\pi} \quad (3.25)$$

The procedure to solve the discretized pipe equations is iterative, with the downstream pressure P<sub>2</sub> as external iterations variable. For given downstream pressure, first we obtain the other downstream conditions by iteratively solving the energy equation (Fanno line) either over vapor quality or temperature at location 2 and then correct the downstream pressure until the momentum equation (Rayleigh line) is also satisfied. Vapor quality is solved first if downstream pressure is below critical pressure. If vapor is found within the physical range (0-1) then T<sub>2</sub> = T<sub>sat</sub>(P<sub>2</sub>). If vapor quality is found outside the physical range then temperature solution is performed and vapor quality is set either to 0 or 1. If the Fanno and Rayleigh lines are found not to intersect then the given mass flow rate is considered as not possible.

### 3.3.5.3 Tank state calculation

Once the mass flow rate has been calculated the tank equations are used to find the tank density and entropy at the next time step. From the new tank density and entropy the tool calculates all the other tank stagnation physical properties (pressure, temperature, vapor quality, enthalpy etc.).

### 3.3.5.4 Numerics

Program execution speed may be highly optimized using Brent's iterative root finding algorithm and Golden section min-maximization algorithm where applicable. Simulation time for PIF algorithm is order of few seconds. Simulation time for a full blow-down is order of minutes.

### 3.3.6 Output values

- Tank stagnation conditions versus time (in case of blowdown) in files and in thermodynamic charts.
- Mass flow rate.
- Distribution of flow and thermodynamic conditions (pressure, temperature, vapor quality, density, velocity) along the discharge line in files and figures.
- Flow and thermodynamic conditions and diameter at the fictitious nozzle.

All units are in SI.

### 3.3.7 Interface (GUI)

The core of the tool has been programmed in Fortran using dynamic libraries such that these can be used without change either in web applications (e.g. eLab) or in standalone mode.

The standalone version of the tool has an interface (GUI) built in python (using ctypes) and integrates all the latest tool features. The eLab version of the tool uses the eLab interface (in python and ctypes). The eLab version does not integrate all the tool's features, with most important that it does not account for a discharge line.

### 3.3.8 References

Leachman, J.W., Jacobsen, R. T., Penoncello, S.G., and Lemmon, E.W. (2009), Fundamental Equations of State for Parahydrogen, Normal Hydrogen, and Orthohydrogen, J. Phys. Chem. Ref. Data, 38, 721-748.

Venetsanos, A.G., and Giannissi, S.G. (2017), Release and dispersion modeling of cryogenic under-expanded hydrogen jets, Int. J of Hydrogen Energy, 42 (11), 7672-7682.

Venetsanos, A.G. (2018), Homogeneous non-equilibrium two-phase choked flow modelling, Int. J. of Hydrogen Energy, 43 (50), 22715-22726.

Venetsanos, A.G. (2019), Choked two-phase flow with account of discharge line effects, ICHS-8, Adelaide, Australia, 26-28 Sept. 2019.

Venetsanos A.G., Giannissi S., Tolias I., Friedrich A., Kuznetsov M. (2021a), Cryogenic and ambient gaseous hydrogen blowdown with discharge line effects, 9th Int. Conf. on Hydrogen Safety, 21-23 Sept. 2021, Edinburgh, UK.

Venetsanos A.G., Ustolin F., Tolias I., Giannissi S., Momferatos G., Coldrick S., Atkinson G., Lyons K., Jallais S. (2021b), Discharge modelling of HSE-LH<sub>2</sub> experiments, 9th Int. Conf. on Hydrogen Safety, 21-23 Sept. 2021, Edinburgh, UK.

### 3.4 Extent of cryogenic pools – HyPond (INERIS)

The purpose of this model is to estimate the size of the liquid pool on the ground produced by a low pressure spillage of liquid hydrogen.

#### 3.4.1 Introduction

HyPond is a single algebraic formula to estimate the maximum extent of the liquid pool likely to spread on the ground following a low pressure spillage of liquid hydrogen. Maximum extent refers to a free expansion of the pool over a flat, free of obstacles and horizontal surface. Since in such a model the vaporization rate is equal to feeding rate of the pool, the tool may help to decide if a retention basin could be useful to reduce the vaporization rate and, following, the size of the dangerous cloud.

#### 3.4.2 Nomenclature

Table 13 reports the nomenclature employed in the model.

**Table 13. Nomenclature of the tool to assess extent of cryogenic pools.**

Parameter	Symbol	Unit
Area of the pool	$A_{pond}$	m <sup>2</sup>
Radius of the pool	$r_{pond}$	m
Latent heat of vaporization	$L_{vap}$	J/kg
Density of the substrate (ground)	$\rho$	kg/m <sup>3</sup>
Specific heat of the substrate (ground)	$C_p$	J/kgK
Thermal conductivity of the substrate (ground)	$k$	W/mK
Thermal diffusivity of the substrate (ground)	$a_{diff}$	m <sup>2</sup> /s
Liquid mass flowrate	$Q_m$	Kg/s
Thermal conductive heat power	$Q_{cond}$	W
Boiling point of the liquid	$T_{eb}$	°C
Substrate (ground) temperature	$T_{ground}$	°C
Time elapsed since the start of the spillage	$t$	s

#### 3.4.3 Model description

The question of the extent of the liquid pool following the spillage of liquid hydrogen (LH<sub>2</sub>) was raised a long time ago, see Makeev et al. (1981), Verfondern and Dienhart (1997),

Chirivella and Witcofski (1986), Zabetakis et al. (1961). Several modelling approaches were proposed, see Ichard et al. (2012), Verfondern and Dienhart (2007), Webber (1991), probably inspired by the detailed work of Briscoe and Shaw (1980). The applicability to cryogenic liquids was recently reviewed in detail by Nguyen et al. (2019).

The models were established under the assumption of a flat, free of obstacles and horizontal surface. Admittedly, this framework might look distant from real situations in which, for instance, rough and porous substrates (sand, gravel, ...) may be present. But it is believed this assumption provides a conservative scenario leading to the largest pool.

Briscoe and Shaw (1980) claimed that the spreading of cryogenic liquids is driven by the equilibrium between the inertia of the flow of liquid along the ground and the gravity forces. The validity of this approach was recently confirmed experimentally by Nguyen et al. (2019).

It was also confirmed that the vaporization is driven by heat conduction in the solid substrate and over most of the duration of the spillage. A quiet boiling occurs suggesting no additional thermal resistance and a constant temperature inside the liquid layer (at the boiling point). Models were established in line with this observation. But this suggests that pool formation occurring in another boiling regime cannot really be addressed this way. In particular, for LH<sub>2</sub> spillages, a violent boiling (presumably film/nucleate boiling) occurs during the first 10/20 seconds (Zabetakis et al., 1961), as shown in Figure 11, producing detached buoyant pockets of flammable mixture (Makeev et al., 1981).

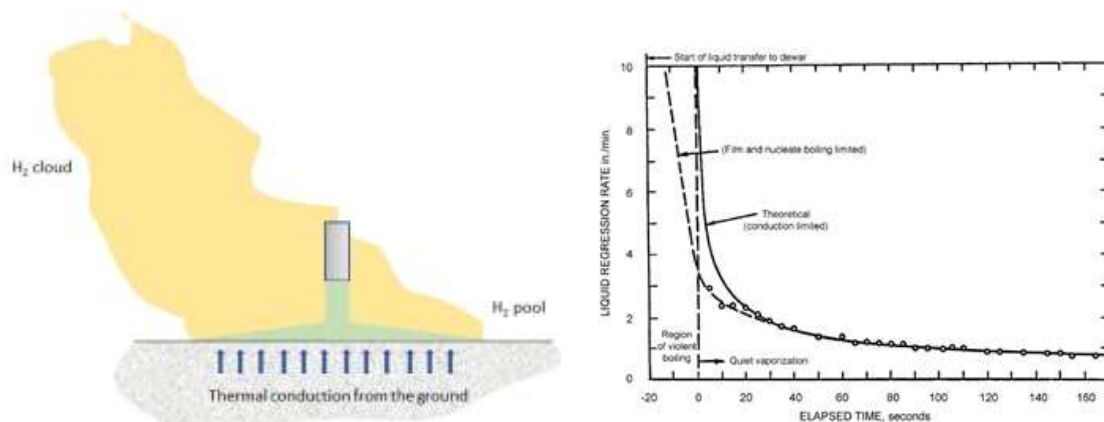


**Figure 11. Representation of the pool formation process (left) and heat flux evolution as function of time during a 1D instantaneous deposit of LH<sub>2</sub> on a paraffin wax thick substrate by Zabetakis et al. (1961) (right).**

So, the following model addresses continuous spillages rather than instantaneous releases. Continuous spillages can be caused by a hose rupturing or disconnection, valve rupturing, bursting discs, etc., which may be likely accident scenarios for LH<sub>2</sub> applications.

Even under such limitations, experimental data are severely lacking: a large scale observation from Chirivella and Witcofski (1986) (3/4 m radius pool after 35 s from a 6 kg/s LH<sub>2</sub> spilled over a compacted sand pad) and a medium scale experimentation from Verfondern and Dienhart (1997) (0.3/0.5 m radius pool after 60 s from a 0.42 kg/s LH<sub>2</sub> spilled over a thick aluminium sheet, 0.4/0.6 m radius pool after 60 s from a 0.35 kg/s LH<sub>2</sub> spilled over water).

Because of the scarcity of the data, a simple and hopefully conservative estimate of the breadth of the pool is proposed: the maximum radius of the pool is obtained by equating the mass flowrate of vaporized hydrogen to that of the LH<sub>2</sub> feeding mass flowrate. Heat is

exclusively provided by thermal conduction through the ground under a quiet boiling regime. The equations representing this physics are:

$$Q_m = \frac{Q_{cond}}{L_{vap}} \quad \text{mass conservation} \quad (3.26)$$

$$Q_{cond} = \frac{A_{pond} \cdot k \cdot (T_{ground} - T_{eb})}{\sqrt{\pi \cdot a_{diff} \cdot t}} \quad \text{heat transfer} \quad (3.27)$$

where  $Q_m$  is the LH<sub>2</sub> mass flowrate,  $Q_{cond}$  the thermal exchange between the pool and the ground,  $L_{vap}$  the heat of vaporization of LH<sub>2</sub>,  $k$  the thermal conductivity of the ground,  $a_{diff}$  the thermal diffusivity of the ground and  $t$  the time elapsed since the start of the release. Numerical values for the thermal parameters are given in the sub section “Input values” below.  $A_{pond}$  is the area of the pool and is linked to the characteristic radius  $r_{pond}$  of the pond as:  $A_{pond} = \pi \cdot r_{pond}^2$ . Finally:

$$r_{pond} = \sqrt{\frac{Q_m \cdot L_{vap} \cdot \sqrt{\pi \cdot a_{diff}}}{k \cdot \pi \cdot (T_{ground} - T_{eb})}} \cdot t^{1/4} \quad (3.28)$$

In the following table, the estimated values for  $r_{pond}$  are compared with some available measurements.

**Table 14. Comparison between experiments and predictions.**

Conditions	Mass flowrate (kg/s)	Pool radius in m (at t= in s) Present estimate	Pool radius in m (at t= in s) Measurements
LN2 on concrete <sup>a</sup>	0.041	0.46 (210)	0.45 (210)
LN2 on concrete <sup>a</sup>	0.088	0.54 (150)	0.48 (80)
LN2 on concrete <sup>a</sup>	0.163	0.57 (30)	0.49 (30)
LH <sub>2</sub> on aluminium <sup>b</sup>	0.42	0.37 (60)	0.3-0.5 (60)
LH <sub>2</sub> on water <sup>b</sup>	0.35	1.4 (60)	0.4-0.6 (60)
LH <sub>2</sub> on compacted sand <sup>c</sup>	6	5.5 (35)	3-4 (35)

<sup>a</sup>Nguyen et al. (2019); <sup>b</sup>Verfondern and Dienhart (1997); <sup>c</sup>Chirivella and Witcofski (1986)

Given the simplicity of this model, the agreement is reasonable between the estimates and the measurements when the nature of the substrate corresponds to that of the assumptions (flat, not porous, etc.). The agreement is not as good in other cases where heat exchange rates can be larger (percolation of LH<sub>2</sub> in the sand, convection over water and phase transition) but the model remains conservative.

The example of the pool formation of LH<sub>2</sub> on the aluminium substrate is shown in Figure 12 together with experimental data.

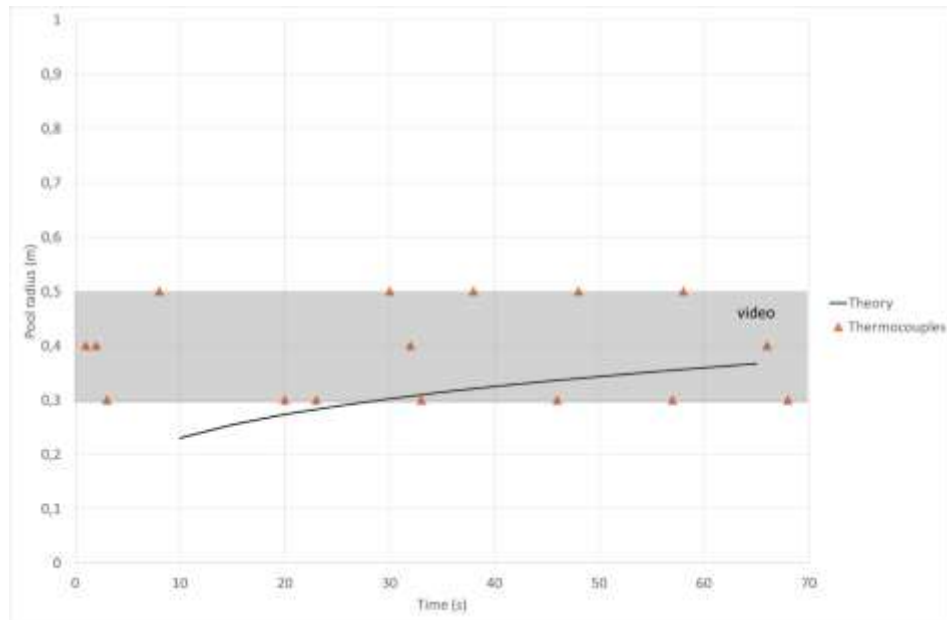


**Figure 12.** Comparison between the predicted evolution of the pool radius and the experimental observation for a 0.42 kg/s LH<sub>2</sub> spill on a thick aluminium plate (points from thermocouple reading and shadowed zone from video records) from Verfondern and Dienhart (1997).

### 3.4.4 Validity range

The models are established under the assumption of a flat, free of obstacles, non porous and horizontal surface. It is believed this assumption provides a conservative estimate leading to the largest pool.

Quiet boiling is assumed, and the estimate can be valid only for long duration spills (longer than 10-20 s). For shorter leakage duration, very different boiling regimes are observed leading to heat fluxes through the ground an order of magnitude different. Consequently, the present model should not be used for catastrophic failures leading to very short spills. Extension to such scenarios would need further development.

### 3.4.5 Input values

The model requires knowledge of the substrate material and properties. Table 15 reports the substrate characteristics for common LH<sub>2</sub> spills scenarios which can be selected. Table 16 reports the input parameters of the LH<sub>2</sub> spill required for calculations and used as example of application. Any self-consistent unit system can be used. In the present description SI units were used. The algebraic equation can be solved using a spreadsheet.

**Table 15. Input parameters on the substrate characteristics.**

Substrate parameters (ground)	Density $\rho$ (kg/m <sup>3</sup> )	Specific heat $C_p$ (J/kgK)	Thermal conductivity $k$ (J/mK)	Thermal diffusivity $a_{diff}$ (m <sup>2</sup> /s)
Concrete	2300	960	0.92	$4.17 \cdot 10^{-7}$
Soil (average)	2500	840	0.96	$4.57 \cdot 10^{-7}$
Soil (sand, dry)	1650	794	0.26	$1.98 \cdot 10^{-7}$
Soil (sand, 8% water)	1750	1000	0.59	$3.37 \cdot 10^{-7}$
Water	1000	4180	0.6	$1.43 \cdot 10^{-7}$
Aluminum	2750	900	220	$8.85 \cdot 10^{-5}$

**Table 16. Input parameters of the LH<sub>2</sub> spill.**

<b>Other parameters</b>	<b>Symbol</b>	<b>Input value</b>	<b>Unit</b>	<b>Limits (min-max)</b>
LH <sub>2</sub> Heat of vaporization	$L_{vap}$	448 690	J/kg	Fixed value
Hydrogen boiling point	$T_{eb}$	-253	°C	Fixed value
Ground temperature	$T_{ground}$	20	°C	none
LH <sub>2</sub> mass flowrate	$Q_m$	0.42	Kg/s	Experimental data range (0-11 kg/s)
Leakage duration	$t$	60	s	Min = 10 s

### 3.4.6 Output values

Table 17 reports the output of the example of application with input parameters in Table 16 for a LH<sub>2</sub> spill on aluminium, which follows validation test in Table 14. Typically, it is expected a 10 m radius for a 10 kg/s spill on the ground after some minutes.

**Table 17. Output parameters for a given LH<sub>2</sub> spill.**

<b>Parameter name</b>	<b>Symbol</b>	<b>Output value</b>	<b>Unit</b>
Characteristic size (radius) of the pool	$r_{pond}$	0.37	m

### 3.4.7 Conclusions

HyPond is a single algebraic formula to estimate the maximum extent of the liquid pool likely to spread on the ground following a low pressure spillage of liquid hydrogen. Maximum extent refers to a free expansion of the pool over a flat, free of obstacles, non porous and horizontal surface.

A quiet boiling regime is assumed which is in place 10-20 s after the start of the spill. So the present model applies rigorously only to prolonged spills and should not be used for catastrophic ruptures leading to very short release durations.

Since in such a model the vaporization rate is equal to feeding rate of the pool, the tool may help to decide if a retention basin could be useful to reduce the vaporization rate and, following, the size of the dangerous cloud.

### 3.4.8 References

- Briscoe F., Chaw P. (1980), Spread and evaporation of liquid, Progress in Energy Combustion Science, Volume 6, pp. 127-140.
- Chirivella JE, Witcofski RD (1986), Experimental results from fast 1500-Gallon LH<sub>2</sub> spills, AIChE Symposium Series 82, pages 120–40.
- Ichard M., Hansen O.R., Middha P., Willoughby D. (2012), CFD computations of liquid hydrogen releases, International Journal of Hydrogen Energy, Volume 37, Issue 22, November 2012, Pages 17380-17389.
- Makeev V.I., Pleshakov V.F., Chuguev A.P. (1981), Formation and combustion of hydrogen-air mixture in processes involving the evaporation of liquid hydrogen into the atmosphere, Combustion, Explosion and Shock Waves, volume 17, pages 489–496.
- Nguyen L.D., Kim M., Choi B., Chung K. (2019), Validation of numerical models for cryogenic-liquid pool spreading and vaporization on solid ground, International Journal of Heat and Mass Transfer, Volume 128, January 2019, Pages 817-824

Verfondern K., Dienhart B. (1997), Experimental and theoretical investigation of liquid hydrogen pool spreading and vaporization, International Journal of Hydrogen Energy, Volume 22, Issue 7, July 1997, Pages 649-660.

Verfondern K., Dienhart B. (2007), Pool spreading and vaporization of liquid hydrogen, International Journal of Hydrogen Energy, Volume 32, Issue 13, September 2007, Pages 2106-2117.

Webber DM (1991), Source terms, Journal of Loss Prevention in the Process Industries, volume 4, pages 5–15.

Zabetakis M.G., Furno A. L., Martindill G.H. (1961), Explosion Hazards of Liquid Hydrogen, Advances in Cryogenic Engineering pp 185-194.

### 3.5 Method for calculating the final state when mixing liquid hydrogen and moist air (HSE)

#### 3.5.1 Introduction

This section describes a means of determining the thermodynamic state when LH<sub>2</sub> is mixed with ambient air. The final state is defined by the following properties:

- Temperature
- Hydrogen volume fraction
- Density

The primary use of such an analysis is to support experiments on dispersing clouds of cold hydrogen in circumstances where there is minimal exchange of heat except with entrained air. The method allows estimation of gas concentrations from measured temperature, if the humidity and temperature of ambient air are known. The method is valid for final temperatures sufficient to prevent condensation of oxygen or nitrogen. This starts to occur at final temperatures below about 72 K. This limiting temperature corresponds to a final hydrogen volume fraction of 70-80% depending on atmospheric temperature and relative humidity (RH).

#### 3.5.2 Nomenclature

Table 18 reports the nomenclature used in the following sections.

**Table 18. Nomenclature in method for calculating the final state when mixing LH<sub>2</sub> and moist air.**

Parameter	Symbol	Unit
Molecular mass	$M$	kg/kmol
Pressure	$p$	Bar
Temperature	$T$	K
Mole fraction of hydrogen	$X$	-
Density	$\rho$	kg/m <sup>3</sup>

#### 3.5.3 Model description

The method requires the user to specify the saturation pressure of the released liquid hydrogen – Figure 13. If the tank is at or close to equilibrium this is simply the release pressure. However, in many of the PRESLHY experiments the liquid was flattened i.e. cooled so that its vapour pressure was approximately 1 bar absolute. The pressure in the vapour space above the liquid was then raised by injecting warmer gas. This non-

equilibrium state corresponds to worst case as far as the potential for rain-out is concerned: high release pressure and consequent flow rates but low liquid temperatures and potential for flash vaporisation. In this case the appropriate saturation pressure, defining the state of the released liquid, is 1 bar absolute (or 0 bar overpressure).

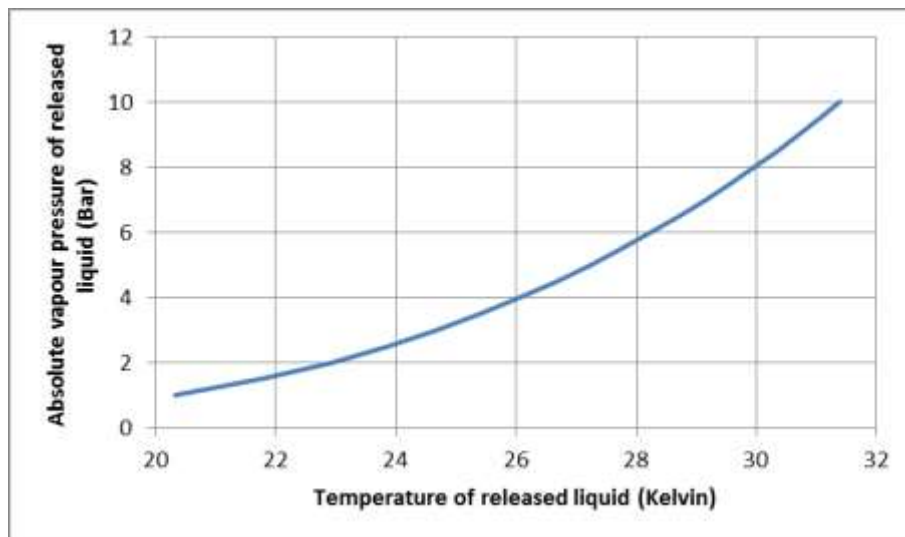


Figure 13. Saturation pressure as a function of liquid temperature

The composition of air is assumed to be 78.12% nitrogen, 20.95% oxygen, 0.93% argon. The method is only valid for a final state >90 K – all of the components of air remain gaseous. The method involves an enthalpy balance between the different components of the mixture. The main elements are listed in Table 19.

Table 19. Elements of the enthalpy balance

Species	Physical changes	Change in Enthalpy	Data source [Web data accessed 08/01/2020].
Hydrogen	Depressurisation Vaporisation Warming to the final state	Increase	NIST tabulated enthalpies of gaseous hydrogen and liquid hydrogen at saturation pressures: <a href="http://webbook.nist.gov">webbook.nist.gov</a>
Air	Cooling from ambient to the final state	Decrease	NIST tabulated enthalpies for Nitrogen: <a href="http://webbook.nist.gov">webbook.nist.gov</a> NIST tabulated enthalpies for Oxygen: <a href="http://webbook.nist.gov">webbook.nist.gov</a> NIST tabulated enthalpies Argon: <a href="http://webbook.nist.gov">webbook.nist.gov</a>
Water vapour	Cooling from ambient to the final state (all final temperatures)	Decrease	Heat capacity of water vapour: <a href="http://engineeringtoolbox">engineeringtoolbox</a> Vapour pressure over water: <a href="http://ddbonline">ddbonline</a> Vapour pressure over ice: Wexler, (1977)
Liquid water	Condensation at ambient temperature	Decrease	Heat of vaporisation as a function of temperature from the Dortmund data bank (Figure 14)

	Cooling to the final temperature (for final states above 273.15 K)		75.28 J/mol/K (Heat capacity of liquid water assumed constant)
Ice	Condensation at ambient temperature	Decrease	See above
	Cooling of water to 273.15 K		See above
	Freezing		5.34 kJ/mol
	Cooling from 273.15 K to the final temperature (for final states below 273.15 K)		Heat capacity of ice >173 K: <a href="#">engineeringtoolbox</a>
			Heat capacity of ice <173 K: Shulman, (2004)

In most cases the original data is presented in tabulated form e.g. enthalpy at ambient pressure as a function of temperature. Polynomial fits to these data have been developed to allow rapid calculation of enthalpy balance using a spread sheet. The specific equations used are given in Section 3.5.4. The heat balance involves equating the increase in enthalpy of hydrogen with the enthalpy release associated with:

- Cooling air to the final state.
- Cooling water and ice to the final state including enthalpies of phase transformation.
- Cooling water vapour to the final state.

Changes of state in gases in air are not included. Condensation of oxygen or nitrogen will not occur until around 72 K, at which point the partial pressure of oxygen exceeds the saturation pressure. For dry air at 293 K this corresponds to a maximum hydrogen mole fraction of around 76%. For RH 100% (293 K) the maximum valid hydrogen fraction is around 80%.

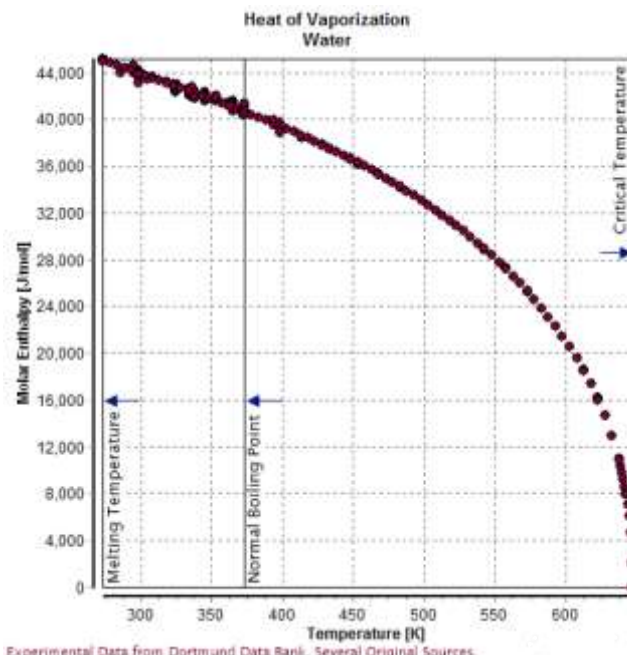


Figure 14. Enthalpy of vaporisation of water.

### 3.5.4 Equations for thermodynamic properties

Enthalpy of gaseous hydrogen at ambient pressure and a range of temperatures

Molar enthalpy (kJ/mol) is expressed as a quadratic function of absolute temperature:  
 $H = A + BT + CT^2$ .

**Table 20. Coefficients of function to assess enthalpy of gaseous hydrogen.**

Temp. range K	A	B	C
70-100	0.615	0.0181	2.00E-05
100-150	0.6244	0.017	3.00E-05
150-200	0.39	0.0199	2.00E-05
200-300	-0.07	0.0245	8.00E-06

The maximum deviation of the fit from tabulated enthalpies is <0.4% in the range 70-300 K. Changes associated with variations in atmospheric pressure are very small in this temperature range and have been neglected.

*Enthalpy of liquid hydrogen at the saturation pressure as a function of storage overpressure (bar)*

Molar enthalpy (kJ/mol) is expressed as cubic function of storage pressure (over ambient) measured in bar:  $H = A + Bp + Cp^2 + Dp^3$ .

**Table 21. Coefficients of function to assess enthalpy of liquid hydrogen.**

A	9.00E-05
B	0.0585
C	-0.0046
D	0.000275

The change in enthalpy of hydrogen between initial liquid, pressurised state and the final warmer, depressurised, gaseous state can simply be found as the difference between enthalpies calculated for gaseous and liquid hydrogen given above. This enthalpy change includes the effects of depressurisation, vaporisation and warming of gaseous hydrogen.

*Enthalpy of water vapour at ambient pressure 70-300 K*

Molar heat capacity is very close to 33.25 J/mol/K throughout the portion of the range where there is a significant water vapour pressure – which is roughly >173K.

*Heat of vaporisation of water at ambient pressure*

This is assumed to vary linearly with temperature between 45 kJ/mol (at 0°C) and 41 kJ/mol (at 100°C).

*Vapour pressure of water over liquid as a function of temperature*

Antoine coefficients for water vapour pressure over liquid water. T measured in °C.

$$p(\text{mmHg}) = 10^{A - \frac{B}{(T+C)}}, \quad (3.29)$$

where A=8.0713, B=1730.63 and C=233.426.

*Vapour pressure of water over ice*

Vapour pressure (over ice) =  $p_{\text{triple}} \times \text{EXP}(A + BT + CT^2 + DT^3)$ . T measured in °C.

**Table 22. Coefficients of function to assess vapour pressure of water over ice.**

A	0.0069	-
B	0.0848	-
C	-0.0002	-
D	3.00E-06	-
P <sub>triple</sub>	611.657	Pa

*Enthalpy of ice as a function of temperature <273.15K*

Molar enthalpy (kJ/mol) is expressed a quadratic function of absolute temperature:  
 $H = A + bT + CT^2$ , where A=5320.2, B=0.4059 and C=0.0705.

#### *Enthalpy of air*

Molar enthalpy (kJ/mol) is expressed as a cubic function of temperature (K):  
 $H = A + BT + CT^2 + DT^3$ .

**Table 23. Coefficients of function to assess enthalpy of air.**

A	-0.1927
B	0.0313
C	-9.00E-06
D	1.00E-08

Pressure sensitivity is <0.1% per 10 kPa deviation and changes associated with variations in atmospheric pressure have been neglected.

#### *Antoine coefficients for oxygen and nitrogen*

In this case the Antoine coefficients deliver a vapour pressure in bar:

$$P(\text{bar}) = 10^{A - \frac{B}{(T+C)}} \quad (3.30)$$

**Table 24. Antoine coefficients for oxygen and nitrogen.**

Nitrogen: <a href="http://webbook.nist.gov">webbook.nist.gov</a>			
Valid temp range	A	B	C
63.14 – 126 K	3.7362	264.65	-6.788
Oxygen: <a href="http://webbook.nist.gov">webbook.nist.gov</a>			
Valid temp range	A	B	C
54.36 - 100.16 K	3.85845	325.675	-5.667

This data is needed to check for oxygen or nitrogen condensation.

#### **3.5.5 Input values**

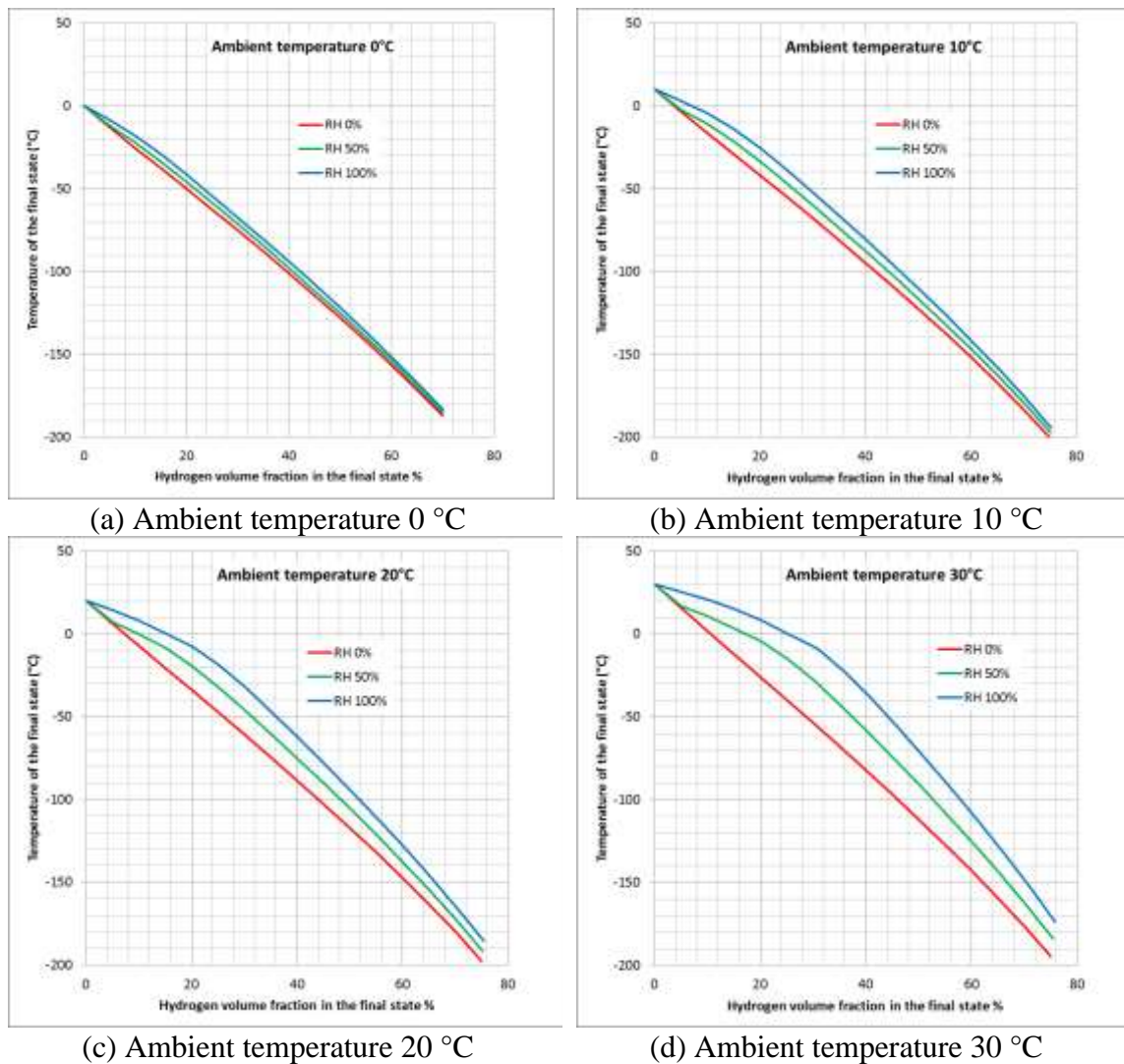
- Initial pressure of liquid hydrogen
- Temperature of ambient air
- Relative humidity

#### **3.5.6 Validity range**

The method is only valid for a final state >90 K where all of the components of air remain gaseous and for initial hydrogen gauge pressures between 0 bar and 12 bar.

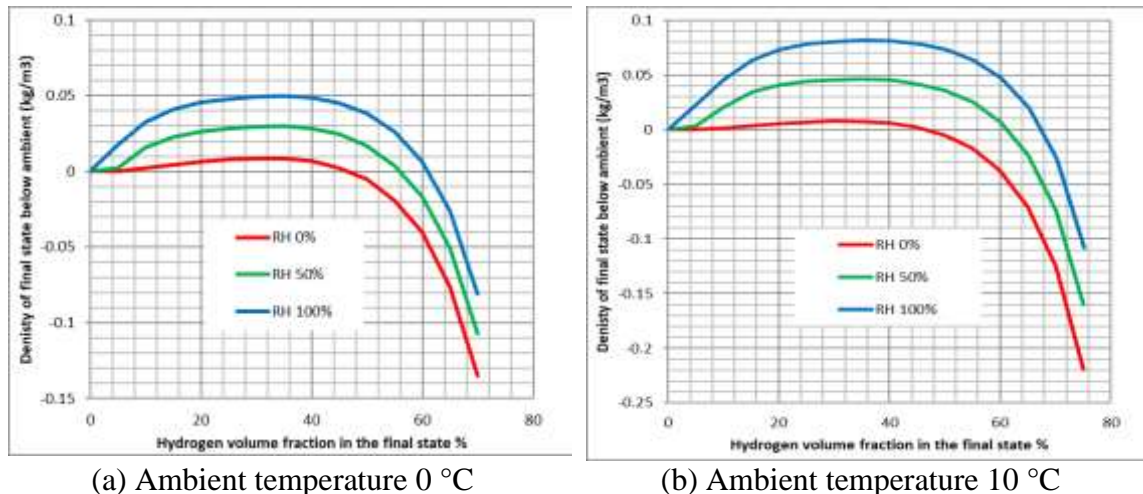
#### **3.5.7 Output values**

Figure 15 (a-d) shows the variation of final temperature with final hydrogen concentration (v/v) for a range of ambient temperatures (0-30 °C) and relative humidities (0%, 50% and 100%). In all cases the initial saturation pressure of the liquid hydrogen was 1 bar (abs).



**Figure 15. Variation of final temperature with final hydrogen concentration (v/v) for a range of ambient temperatures (0 - 30 °C) and relative humidities (0%, 50% and 100%).**

Figure 16(a-d) shows the variation of final density difference with final hydrogen concentration (v/v) for a range of ambient temperatures (0-30 °C) and relative humidities (0%, 50% and 100%). This is the difference in density between the cloud and surrounding ambient air. In all cases the initial saturation pressure of the LH<sub>2</sub> was 1 bar (abs).



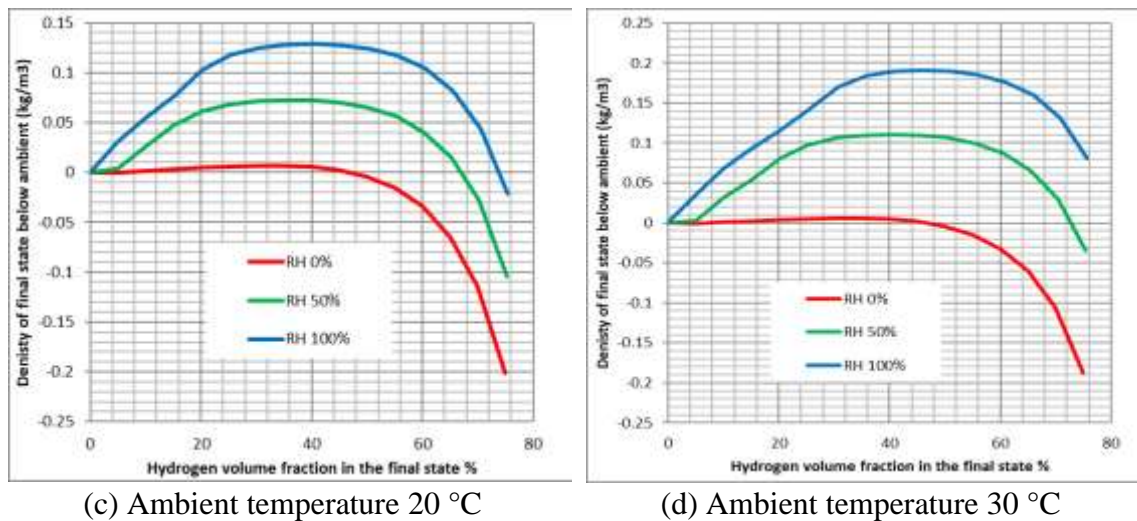


Figure 16. Variation of final density difference with final hydrogen concentration (v/v) for a range of ambient temperatures (0-30 °C) and relative humidities (0%, 50% and 100%).

Figure 17 shows the effect of release pressure for a particular ambient temperature and RH.

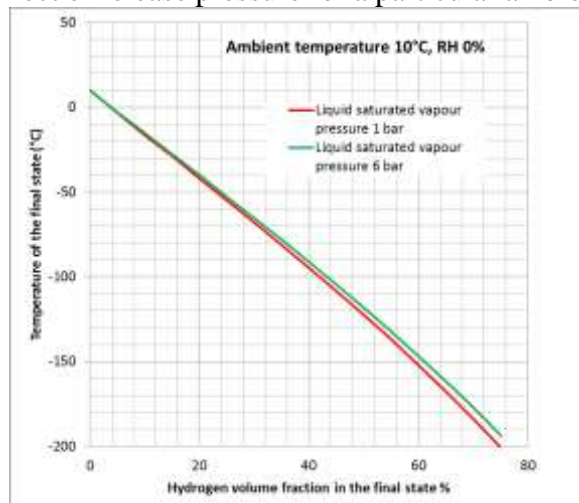


Figure 17. Effect of release pressure on the final state (saturated vapour pressures are absolute pressures).

The method can be implemented in e.g. a spreadsheet to calculate an overall enthalpy balance. All units are SI.

### 3.5.8 Conclusions

Accurate measurements of ambient conditions (temperature and humidity) are required in order to use temperature data to determine hydrogen volume fractions.

In warm weather the difference between RH 0% and RH 100% can amount to 20% H<sub>2</sub> v/v - for a given measured temperature.

The additional enthalpy associated with liquid at elevated saturated vapour pressures makes a small difference to the final state. As expected, this increases with the proportion of hydrogen in the mixture. In many cases there will be some heat transfer to the liquid hydrogen in the pipework leading to the release point and this may result in some flashing. Usually this will not markedly affect the final state in the dispersing cloud.

Even if there is limited heat transfer from the ground or solid object the vapour clouds formed by releasing liquid hydrogen are somewhat buoyant unless the hydrogen concentration is very high. This is particularly true if the ambient air is warm and humid.

In the very earliest stages of the release where the proportion of air is small the density can be greater than that of the surrounding air. However, the velocity of the gas will be high at this stage and the flow is likely to be momentum driven.

Condensing water vapour increases buoyancy because removal of one mole of water releases around 42 kJ of heat. This would be sufficient to raise the temperature of the mole of air that replaces the water by a temperature equal to roughly

$$\Delta T = \frac{\Delta H_{vap}}{c_p} \sim 1400 \quad (3.31)$$

Such a temperature rise would increase the volume of the air by more than a factor of two, so there is an overall increase in volume and drop in density.

### 3.5.9 References

Shulman, L. M. (2004), The heat capacity of water ice in interstellar or interplanetary conditions. *Astronomy & Astrophysics*, 416(1), 187-190, <http://dx.doi.org/10.1051/0004-6361:20031746>

Wexler, A. (1977), Vapor Pressure Formulation for Ice, *J. of the National Bureau of Standards- A. Physics and Chemistry* Vol. 81A, No. 1, January-February.

## 4 Ignition

This chapter presents the engineering correlations and tools developed to evaluate the hazards associated to ignition of cryogenic hydrogen-air mixtures.

### 4.1 Ignition Energy for hydrogen-air mixtures (UU)

#### 4.1.1 Introduction

The present analytical model is aimed at determining the Minimum Ignition Energy (MIE) by spark ignition in hydrogen-air mixtures with arbitrary concentration and initial temperature. The model uses the laminar flame thickness to determine the critical flame kernel. To assess the validity of the correlation, results are compared against experiments in ((Lewis and Elbe, 1961); (Ono et al., 2007)) and the experiments performed by INERIS within PRESLHY project (Proust, 2021).

#### 4.1.2 Nomenclature

Table 25 lists the nomenclature used in the correlation.

**Table 25. Nomenclature for assessment of MIE.**

Parameter	Symbol	Unit
Specific heat at constant pressure	$c_p$	J/kgK
Diameter of the critical flame kernel	$d$	m
Energy	$E$	J
Minimum energy to ensure ignition	$E_{min}$	J
Thermal conductivity	$k$	W/mK
Laminar flame speed	$S_u$	m/s
Temperature	$T$	K
Corrective parameter for the laminar flame speed to take into account flame stretch and selective diffusion	$X_{SD}$	-
Laminar flame thickness	$\delta_L$	m
Stoichiometric coefficient	$\Phi$	-
Density	$\rho$	kg/m <sup>3</sup>

**Table 26. Subscripts and superscripts.**

Subscripts	Symbol
Averaged between burnt and unburnt properties	$av$
Burnt mixture	$b$
Minimum	$min$
Property taking into account flame stretch and selective diffusion	$SD$
Unburnt mixture	$u$
Superscripts	Symbol
Blint's definition	$B$
Unstretched flame property	$0$

#### 4.1.3 Model description

The model is based on the theoretical correlation in (Lewis and Elbe, 1961), considering the MIE as the amount of energy required to heat up a sphere of flammable mixture at initial temperature  $T_u$  of the unburnt mixture, to that of the flame,  $T_b$ . The quenching distance,  $d$ , is considered as the diameter of the critical flame kernel:

$$E_{min} = \frac{1}{6} \pi d^3 \rho_{av} C_{p,av} (T_b - T_u) \quad (4.1)$$

The diameter of the critical flame kernel is considered to be proportional to the laminar flame thickness, as supported by (Law, 2006). It is reasonable to assume that a flame kernel should have diameter of at least twice the laminar flame thickness,  $\delta_L$ , to obtain the flame propagation. Studies mentioned in Babrauskas (2003) reported the quenching distance to be  $2-2.2\delta_L$  and  $3.1\delta_L$ . In the present model, the quenching distance, thus the critical flame kernel diameter, is calculated as  $d = 2.5\delta_L$ . The laminar flame thickness is estimated using Blint's correlation reported in (Poinsot and Veynante, 2005):

$$\delta_L^B = 2\delta \frac{k_p/c_{p,b}}{k_u/c_{p,u}} \quad (4.2)$$

where  $\delta$  is the so-called "diffusive" flame thickness, defined by the authors as:

$$\delta = \frac{k_u}{\rho_u c_{p,u} S_u} \quad (4.3)$$

with  $k_u$  is the thermal conductivity,  $\rho_u$  is the density and  $c_{p,u}$  is the specific heat at constant pressure for the unburnt mixture. The following sections will show how to estimate the thermophysical properties of the mixture and the laminar flame speed.

#### 4.1.3.1 Calculation of parameters for the unburnt and burnt mixtures

The model requires the knowledge of the following thermophysical properties characterising the unburnt and burnt mixture: density, thermal conductivity, specific heat at constant pressure and the temperature of the burnt mixture, which is assumed to be the adiabatic flame temperature. These parameters were calculated through the equilibrium solver available in Cantera v2.4.0, assuming a constant pressure. Results are reported in Figure 18 as function of the hydrogen concentration in air. Figure 19 reports the thermophysical properties for mixtures with initial temperature in the range 100-250 K. Whether calculation through Cantera is not possible, the user may use Figure 18 and Figure 19 to retrieve graphically the properties required to apply the model.

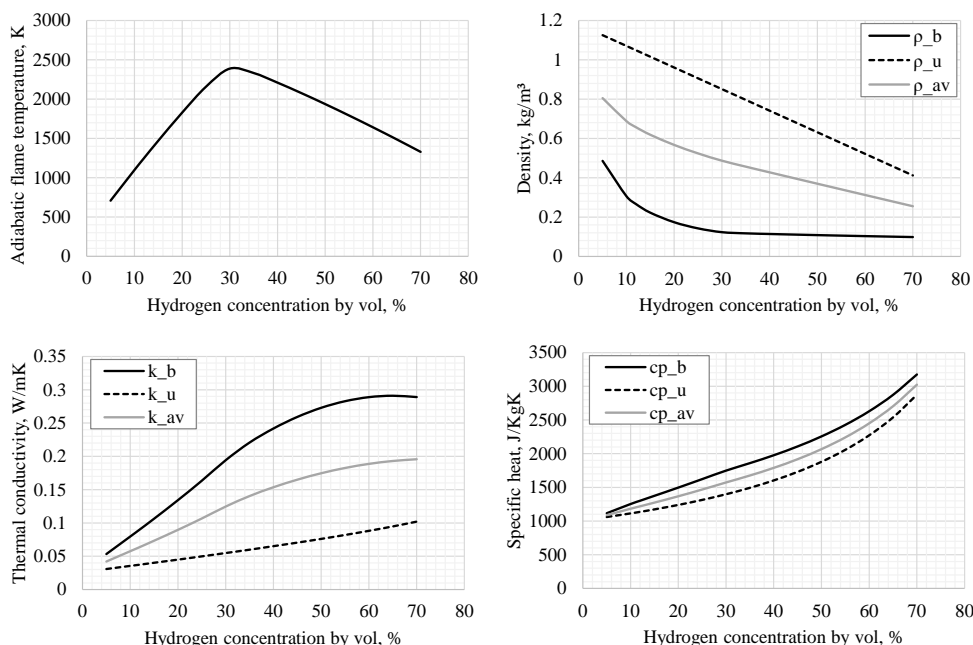


**Figure 18. Thermophysical properties of the unburnt and burnt mixture as function of hydrogen concentration in air for ambient temperature (Tu=298K).**

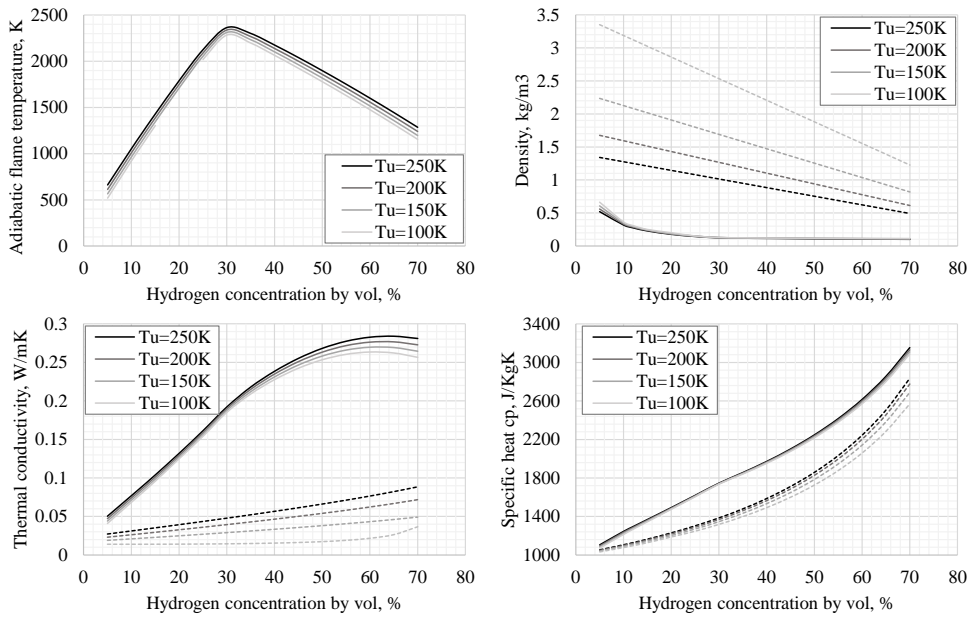


**Figure 19. Thermophysical properties of the unburnt (dashed lines) and burnt mixture (solid lines) as function of hydrogen concentration in air for temperature  $T_u=100-250$  K.**

#### 4.1.3.2 Calculation of the laminar flame speed

Chemkin software was employed to estimate the laminar flame speed for a freely propagating, adiabatic 1-D flame at atmospheric pressure. The laminar flame speed, by definition, is calculated as the relative speed between the unburnt gas mixture and the flame front. Detailed chemical mechanism considers a subset of (Peters and Rogg, 1993) mechanism with 18-step reduced chemical reaction mechanism for hydrogen combustion in air and 9 chemical specie. These calculations were found to better agree with experimental data provided in (Lamoureux. et al., 2002) on unstretched laminar flame speed compared to estimations performed via Cantera with GRI3.0 mechanism and Dryer's mechanisms. Figure 20 shows the results of the unstretched laminar flame speed as function of hydrogen concentration in air and initial temperature of the mixture. This can be used by the user to retrieve graphically the laminar flame speed to be applied in the specific case.

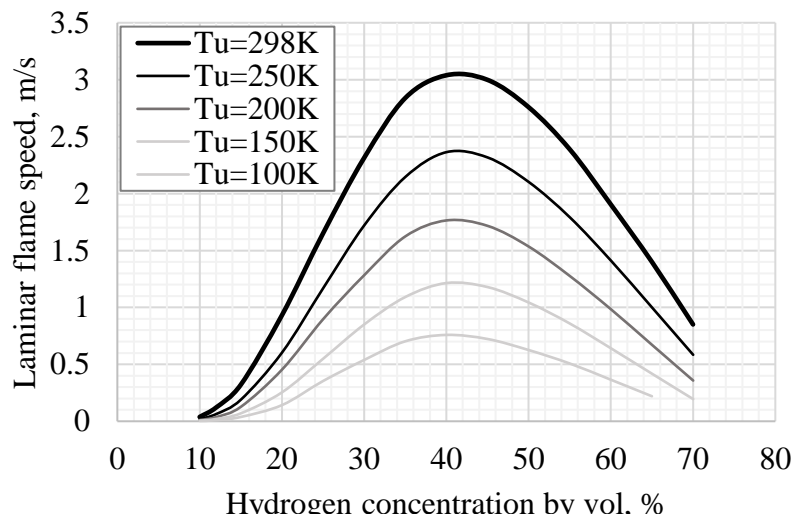


**Figure 20. Unstretched laminar flame speed calculated through Chemkin software as function of hydrogen concentration in air and temperature of the unburnt mixture.**

Chemkin assumes a one-dimensional freely propagating premixed flat flame. Therefore, it calculates the unstretched laminar flame speed,  $S_u^0$ . In spherical expanding flames, the local stretch due to the curvature and the strain rate causes the velocity at which the flame increases size to be different from that of a planar flame. Depending on the mixture composition, the spatial velocity will increase or decrease as the stretch is enhanced (see Lamourex et al., 2003).

Thermal diffusive flame instabilities may verify in combustion, depending on the effective Lewis number of the reactants. The combined effect of preferential diffusion and flame stretch may result in a local redistribution of the element mass fraction and enthalpy, leading to fuel enriched zones in a lean flame and resulting locally in more intense burning. This translates into an acceleration of the flame speed in lean hydrogen mixtures, which are in an unstable propagation regime. Evidences of this behaviour are given in experimental studies by (van Oijen et al., 2010), (Kishore et al., 2008), (Kuznetsov et al., 2012). As reported in (Kishore et al., 2008), the transition from unstable to stable regime is verified for a stoichiometric coefficient equal ( $\Phi$ ) to 0.6 in H<sub>2</sub>-O<sub>2</sub>-Ar mixtures. A hydrogen concentration of 24-26% ( $\Phi \approx 0.8$ ) was found to be the limit for unstable-stable propagation of the flame in air (Lamourex et al., 2003).

To include effect of both flame stretch and selective diffusion, a corrective parameter is calculated as the ratio of the stretched laminar flame speed taking into account preferential diffusion,  $S_u^{SD}$ , by (Zimont and Lipatnikov, 1995), and the unstretched laminar flame speed given by the dataset including data by (Alekseev et al., 2015) for hydrogen-air mixtures with  $\Phi=0.3\text{-}0.6$  and Lamourex et al. (2003) for  $\Phi=0.6\text{-}3.75$ :

$$X_{SD} = \frac{S_u^{SD}}{S_u^0} \quad (4.4)$$

The resulting corrective factor  $X_{SD}$  was extrapolated from experimental data, and can be calculated as follows:

$$\begin{aligned} X_{SD} &= 12980 \cdot (C_{H_2})^{-2.98} \text{ for } C_{H_2} < 20\% \\ X_{SD} &= 100 \cdot (C_{H_2})^{-1.2} \text{ for } 20\% \leq C_{H_2} < 35\% \\ X_{SD} &= 1 \text{ for } C_{H_2} \geq 35\% \end{aligned} \quad (4.5)$$

where  $C_{H_2}$  is the percentage of hydrogen concentration in air.

#### 4.1.4 Validity range

The model has been validated for mixtures with hydrogen concentration in air within range 9-70% and initial temperature in range 173-300K. The model can be applied to mixtures with initial temperature down to 80 K with hydrogen concentration within range 10-65%.

Figure 21 shows the comparison of the calculated MIE versus experiments for mixtures at initial temperature equal to ambient by Lewis and Elbe (1961), Ono et al. (2007), and the experiments performed by INERIS within PRESLY project (Proust, 2021).

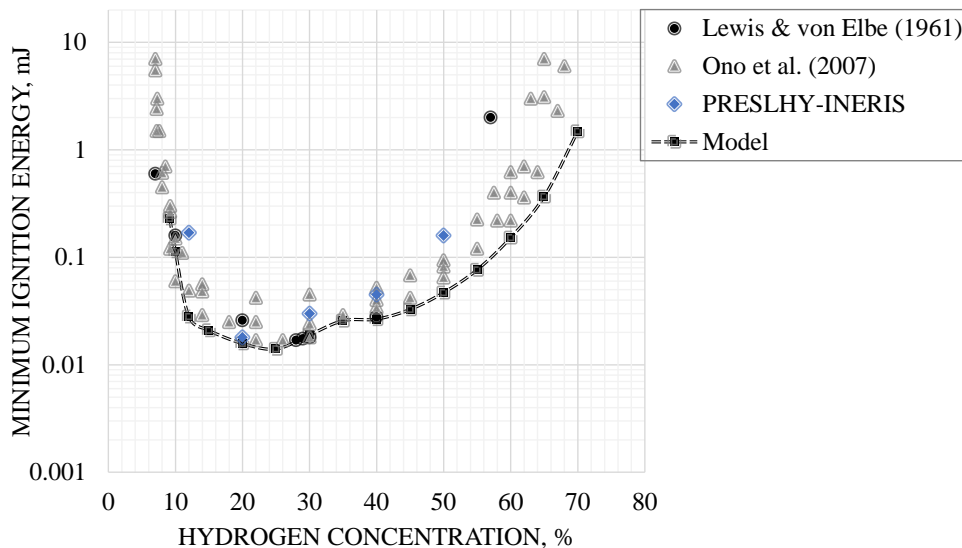


**Figure 21. Validation of the analytical model versus experiments performed with hydrogen-air mixtures at initial temperature equal to ambient.**

Figure 21 shows that the model well predicts experimental MIE for rich mixtures ( $H_2 > 40\%$  by vol in air), providing a conservative estimation of MIE. In near proximity of hydrogen concentration of 30% the model implementing corrections presents a jump in the MIE curve, due to the implementation of the corrective factor. The absolute MIE is 14  $\mu J$  and is found for a hydrogen concentration in the range 20-25%, which is within the range 22-26% leading to MIE of 17  $\mu J$  in experiments by (Ono et al., 2007). For concentrations below 20% H<sub>2</sub> by vol in air, the model leads to a conservative estimation of the ignition energy, with exception of calculations for 10% hydrogen by vol in air.

Variation of the analytical model predictions for lean H<sub>2</sub>/air mixtures from experiments may be associated as well to the following factors:

- The model assumes spherical flames at constant pressure with a uniform stretch rate over the flame surface, which may be inadequate for high energy discharges;
- There could be more uncertainties in the employed chemical mechanisms, as observed in (Bane et al., 2013);
- The onset of instabilities may occur earlier in the flame propagation, leading to a higher burning speed (Bane et al., 2013);
- The high energy discharge may increase the turbulence instabilities accelerating the flame speed.

Experiments on cryogenic mixtures ( $T=173$  K) were performed by INERIS within PRESLHY project. Figure 22 compares the model predictions versus experimental results for the ignition energy leading to ignition (I) and to no ignition (NI) of the mixture. The model predicts well the minimum ignition energy associated to the range of concentrations 20-30%. For H<sub>2</sub>=40% by vol, the model results in an ignition energy lower than the minimum value recording ignition in experiments. However, it can be observed that a lower number of tests was performed for this concentration and may not be sufficient to withdraw exact conclusions on the accuracy of the analytical model predictive capability. On the other hand, the model overestimates the IE for H<sub>2</sub>=10%. In addition to the possible causes affecting the model performance for lean hydrogen concentrations as explained for ambient temperature mixtures, it should be noted that experimental ignition energies reported in Figure 22 are given for a spark yield of 100%. The yield of the spark, i.e. the portion of

energy effectively released in the spark channel at the net of losses in the circuit, depends strongly on the employed voltage and current. As reported in (Proust, 2021), the spark yield was found to vary from 90% to approximately 20% for a high voltage spark. For H<sub>2</sub>=10%, a spark yield closer to 20% is expected, due to the associated high voltage.

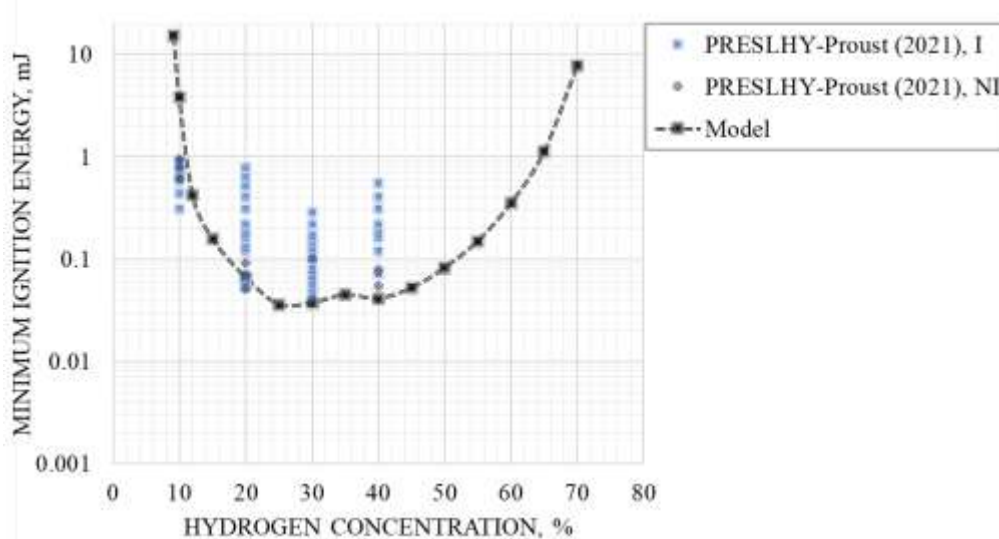


Figure 22. Validation of the analytical model versus experiments performed with hydrogen-air mixtures at initial temperature equal to 173 K.

#### 4.1.5 Input values

Table 27 reports the parameters required as input for the model. The column input value reports an example of calculations to test the tool.

Table 27. Input parameters to determine MIE for hydrogen-air mixtures.

Parameter	Symbol	Input value	Unit	Limits (min-max)	Defaults
Hydrogen concentration, %	H <sub>2</sub>	30	-	9-70	30
Mixture temperature	T	173	K	173-300	290

#### 4.1.6 Output values

The tool allows to calculate the minimum ignition energy for a given hydrogen concentration in air and initial temperature, providing an output as in Table 28.

Table 28. Output parameters for determination of MIE for hydrogen-air mixtures.

Parameter	Symbol	Output value	Unit
Ignition Energy	E <sub>min</sub>	66.1 · 10 <sup>-6</sup>	J

#### 4.1.7 Conclusions

A novel model for determination of MIE in hydrogen-air mixtures has been developed by employing the laminar flame thickness for calculation of the critical flame kernel produced by spark ignition. The laminar flame thickness was calculated by using the laminar flame speed including effects of the flame stretch and preferential diffusion characterising lean mixtures. The model well agrees with experimental results for both ambient and cryogenic hydrogen-air mixtures with concentration in the range 9-70%.

#### 4.1.8 References

Alekseev, V.A., Christensen, M., Berrocal, E., Nilsson, E.J.K.. and Konnov, A.A. (2015), Laminar premixed flat non-stretched lean flames of hydrogen in air, Combustion and

Flame, Vol. 162, pp. 4063–4074.

Babrauskas, V. (2003), Ignition Handbook, Society of Fire Protection Engineers, Fire Science Publishers, Issaquah WA, USA.

Bane, S.P.M., Ziegler, J.L., Boettcher, P.A., Coronel, S.A. and Shepherd, J.E. (2013), Experimental investigation of spark ignition energy in kerosene, hexane, and hydrogen, Journal of Loss Prevention in the Process Industries, Elsevier Ltd, Vol. 26 No. 2, pp. 290–294.

Kishore, V.R., Ravi, M.R. and Ray, A. (2008), Effect of Hydrogen Content and Dilution on Laminar Burning Velocity and Stability Characteristics of Producer Gas-Air Mixtures, International Journal of Reacting Systems, Vol. 2008, pp. 1–8.

Kuznetsov, M., Kobelt, S., Grune, J. and Jordan, T. (2012), Flammability limits and laminar flame speed of hydrogen-air mixtures at sub-atmospheric pressures, International Journal of Hydrogen Energy, Vol. 37 No. 22, pp. 17580–17588.

Lamoureux., N., Djebaili-Chaumeix, N. and Paillard, C.E. (2002), Laminar flame velocity determination for H<sub>2</sub>-air-stream mixtures using the spherical bomb method, J. Phys., Vol. 12, pp. 445–458.

Law, C.K. (2006), Combustion Physics, Cambridge University Press.

Lewis, B. and Elbe, G. von. (1961), Combustion, Flames and Explosions of Gases, Zeitschrift Für Physikalische Chemie, Vol. 36, Academic Press, New York, available at:[https://doi.org/10.1524/zpch.1963.36.3\\_4.136](https://doi.org/10.1524/zpch.1963.36.3_4.136).

van Oijen, J.A., Bastiaans, R.J.M. and Goey de, L.P.H. (2010), Modelling preferential diffusion effects in premixed methane-hydrogen-air flames by using flamelet-generated manifolds”, Fifth European Conference on Computational Fluid Dynamics, {ECCOMAS CFD 2010, Lisbon, Portugal, 14-17 June 2010, No. June, pp. 1–12.

Ono, R., Nifuku, M., Fujiwara, S., Horiguchi, S. and Oda, T. (2007), Minimum ignition energy of hydrogen-air mixture: Effects of humidity and spark duration, Journal of Electrostatics, Vol. 65 No. 2, pp. 87–93.

Peters, N. and Rogg, B. (1993), Reduced Kinetic Mechanisms for Applications in Combustion Systems, Berlin, edited by Springer-Verlag, Berlin.

Poinsot, T. and Veynante, D. (2005), Theoretical and Numerical Combustion, Second Edition, Decision Support Systems, Second., R.T. Edwards, Inc., P.O., Philadelphia, PA, USA, available at:<https://doi.org/10.1016/j.dss.2003.08.004>.

Proust, C. (2021), PRESLY D4.4 Summary of Experiment Series E4.1 Results (Ignition Parameters).

Zimont, V.L. and Lipatnikov, A.N. (1995), A numerical model of premixed turbulent combustion of gases, Chemical Physics Reports, Vol. 14 No. 7, pp. 993–1025.

## 4.2 Electrostatic field built-up generated during hydrogen releases (PS)

The present engineering tool, abbreviated as ElFiBU, aims at the assessment of electrostatic field built-up during hydrogen releases through a nozzle with circular aperture.

### 4.2.1 Introduction

The tool ElFiBU aims to give the possibility to estimate the electrostatic field built-up during hydrogen releases through a nozzle with circular aperture on the basis of values that were measured by Pro-Science/KIT during the DisCha-experiments in the frame of the

tasks 5.1 and 4.2 of the EC-funded project PRESLHY. In the experiments electrostatic fields were measured with two field-mills (model Kleinwächter, model EFM 113B, 0 - 10 kV/m) in distances of 0.5 m and 1.5 m from the nozzle with a horizontal distance of 0.9 m to the jet axis. In the experiments H<sub>2</sub>-releases from a reservoir at a wide range of initial pressures through circular nozzles with four different diameters at two different reservoir temperatures (ambient temperature and approx. 80 K) were investigated.

#### 4.2.2 Nomenclature

Table 29 provides the nomenclature employed in the model description.

**Table 29. Nomenclature for the tool EIFiBU.**

Parameter	Symbol	Unit
Nozzle diameter	$d_{Nz}$	mm
Initial pressure in reservoir	$p_{ini}$	bar
Electric field	$E$	V/m

#### 4.2.3 Model description

The experiments at ambient temperature showed no significant field built-up, which coincides with the assumption that the field built-up is closely connected with ice-crystals that form at the tip of the nozzle prior to the experiment when they were performed at the lower temperature level of approx. 80 K. It is assumed that the source of the electric fields, the so-called Tribo-Electricity, is generated through the friction and separation of these ice crystals when they are blown away from the nozzle at the beginning of the H<sub>2</sub>-release. This assumption is furthermore supported by the fact that significant electric fields were measured mainly in the first 500 ms after the beginning of the H<sub>2</sub>-release.

The EIFiBU-correlation consists of two formulas, one for the generation of positive fields Eq. (4.6) and one for the generation of negative fields Eq. (4.7):

$$\text{Positive Field Built-up: } E(+)\leq(4\cdot d_{Nz}+1)\cdot p_{ini} \quad (4.6)$$

$$\text{Negative Field Built-up: } E(-)\leq(-14\cdot d_{Nz}-11)\cdot p_{ini} \quad (4.7)$$

(The formulas might be used as a kind of rule of thumb and so the units do not match. Corresponding units can be added to slope and intercept of the linear equation in brackets)

Both formulas were derived only from experiments with reservoir temperatures of approx. 80 K, since the experiments at ambient temperature did not generate relevant electric fields. For all experiments at ambient temperature with the two smallest nozzles ( $d_{Nz} = 0.5$  mm and 1 mm) negligible fields in the range  $10 \text{ V/m} > E > -10 \text{ V/m}$  were measured. For the two larger nozzles ( $d_{Nz} = 2$  mm and 4 mm) the range of  $E = \pm 50 \text{ V/m}$  was exceeded in only 4 of the 22 experiments performed, with the highest measured electric field being  $E = -233 \text{ V/m}$ . In the experiments at approx. 80 K the highest measured electric field was  $E = -5730 \text{ V/m}$ .

The measured values were grouped according to the nozzle diameters used and sorted by increasing initial pressure. To gain a conservative approach only the extremal values for every case, this means the highest positive field and the lowest negative field for several experiments with the same nozzle diameter and the same initial pressure were selected. These selected values were then plotted in graphs over the initial pressure, one graph for each nozzle diameter, see Figure 23.

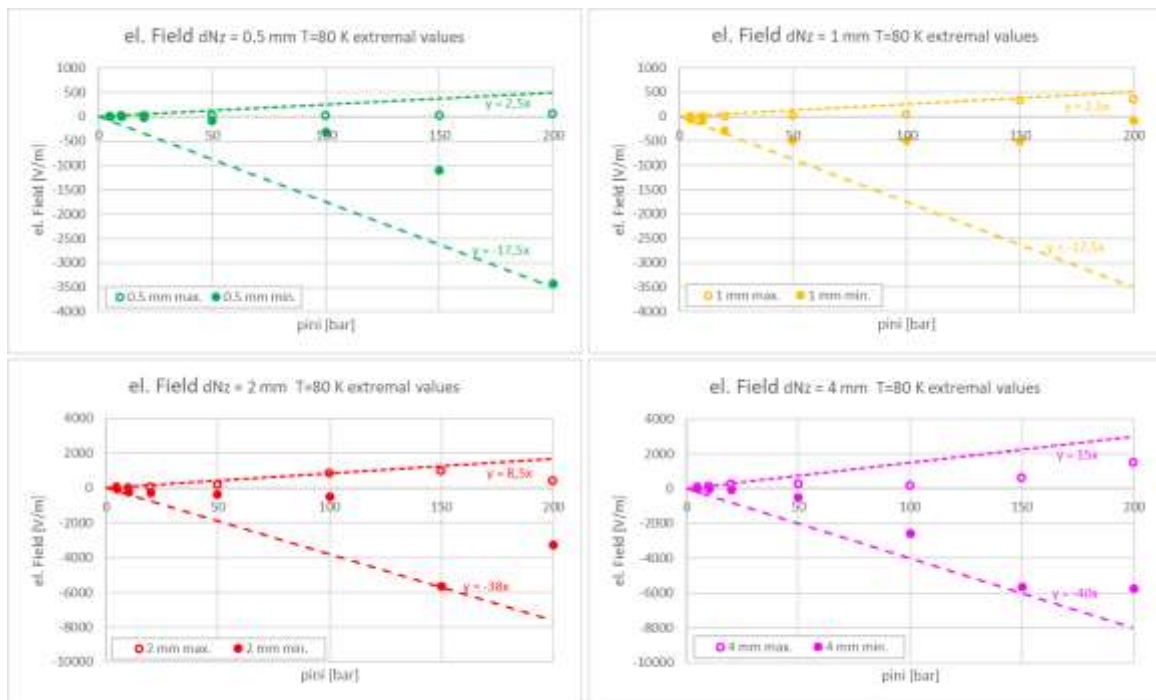


**Figure 23.** Graphs with extremal field values over initial pressure for each nozzle diameter and corresponding auxiliary lines.

To every graph two auxiliary straight lines from the origin were added that envelope all measured data points, one line for the positive values and one line for the negative ones. The slope of the different auxiliary lines was then plotted over the nozzle diameter (see Figure 24) and then again two straight lines in the range 0.5 mm to 4 mm were drawn that envelope all data points.

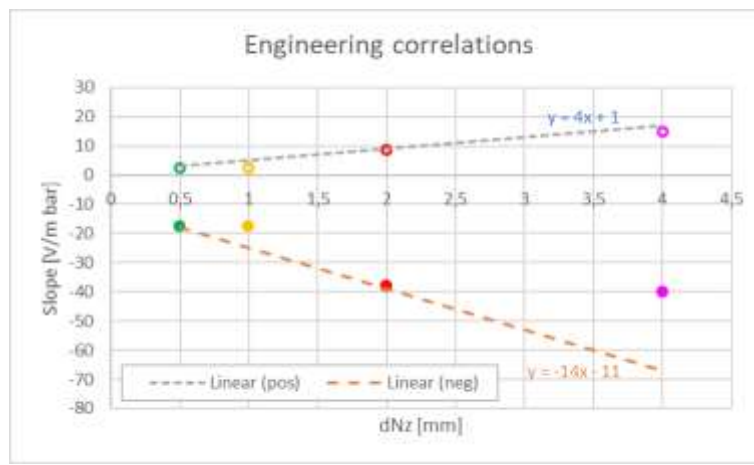


**Figure 24.** Derivation of the factors for the engineering correlations for the estimation of field built-up.

The equations of these straight lines together with the initial pressure form the engineering correlations for the estimation of the positive field built-up (Eq. 4.6) and the negative field built-up (Eq. 4.7). The corresponding lines for both correlations Eq. (4.6) and Eq. (4.7) are plotted together with the experimental data and the auxiliary lines in Figure 25.

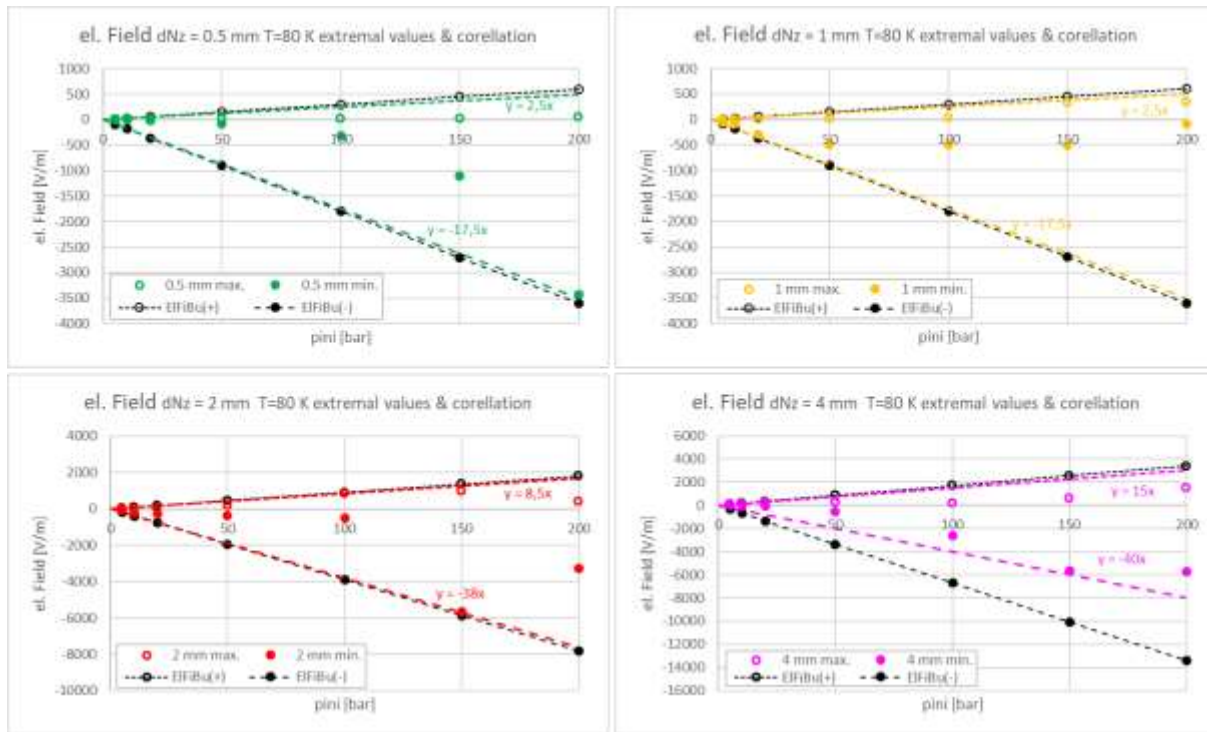


**Figure 25.** Lines for the correlations (4.6) and (4.7) in black together with the experimental data and the auxiliary lines for each nozzle diameter.

#### 4.2.4 Validity range

The experiments used for the derivation of empirical correlations were performed at 2 temperature levels with 4 circular nozzles and 7 initial pressure stages.

**Temperature stages:** Experiments were performed at ambient temperature (approx. 290 K) and with the reservoir vessel being cooled down to approx. 80 K in a bath of liquid nitrogen (LN2).

**Nozzle diameters:** Experiments were performed with circular nozzles of the diameters 0.5 mm, 1 mm, 2 mm and 4 mm.

**Initial reservoir pressures:** Experiments were performed with initial reservoir pressures of 5 bar, 10 bar, 20 bar, 50 bar, 100 bar, 150 bar and 200 bar.

In the experimental series the complete matrix of 2 (temperatures) x 4 (nozzle diameters) x 7 (pressure stages) was executed at least once (56 cases). But several repetitions, especially for the cold temperature, large nozzle diameters and high initial pressures were made. In total 123 experiments were used for the evaluation, of which 35 were at ambient temperature and 88 were at approx. 80 K.

In the experiments at ambient temperature no significant field built-up could be measured and so the complete derivation was made using experiments at approx. 80 K. Due to the fact that all measured fields at ambient temperature were significantly lower, the formula might be applicable also to temperatures higher than 80 K, but this assumption is not yet proved in detail. Lower initial temperatures might generate much higher fields and thus the formula should not be used at lower temperature than 80 K.

The formulas were derived using experimental data with initial pressures from 5 to 200 bar. Since smaller initial pressures usually generated lower fields, the formula might also be applicable to smaller initial pressures. But in most of the cases the field strength increased

rapidly with increasing initial pressure, so an extrapolation of the formulas to higher pressures than 200 bar might lead to faulty values very soon and should thus not be done.

The same applies to the nozzle diameters investigated (0.5 mm to 4 mm). With decreasing nozzle diameters usually lower fields were measured, so the formula might also be applicable to smaller nozzle diameters. With increasing nozzle diameter the measured field strength increased rapidly and so an extrapolation of the formula to larger nozzle diameters is not recommended.

#### 4.2.5 Input values

The two formulas of the ElFiBU-correlation for the estimation of the generation of positive (Eq. 4.6) and negative fields (Eq. 4.7) during the H<sub>2</sub>-releases from a reservoir can be used by simply entering the input values nozzle diameter (dNz) and initial reservoir pressure (p<sub>ini</sub>), as in Table 30.

**Table 30. Input parameters for the ElFiBU-correlation and example of application.**

Parameter	Symbol	Input value	Unit	Limits (min-max)	Defaults
Initial reservoir pressure	$p_{ini}$	100	bar	5 - 200	100
Nozzle diameter	$dNz$	2	mm	0.5 – 4.0	2

#### 4.2.6 Output values

The two formulas of the ElFiBU-correlation for the estimation of the generation of positive (Eq. 4.6) and negative fields (Eq. 4.7) generate one number each, which corresponds to the maximum positive (E(+)) or minimum negative field (E(-)) value to be expected during the release, as shown in example of application in Table 31.

**Table 31. Output parameters for the ElFiBU-correlation and example of application.**

Parameter name	Symbol	Output value	Unit
Max. positive electric field	$E(+)$	900	V/m
Min. negative electric field	$E(-)$	-3900	V/m

#### 4.2.7 Conversion of input and output units

In both formulas of the ElFiBU-correlation for the estimation of the generation of positive (Eq. 4.6) and negative fields (Eq. 4.7) the same two input variables are required.

Initial reservoir pressure (p<sub>ini</sub>) should be entered in bar, conversion from SI unit see below.

$$P_{ini} [\text{bar}] = p_{ini} [\text{Pa}] \times 10^{-5} \quad (4.8)$$

Nozzle diameter (dNz) should be entered in mm, conversion from SI unit see below.

$$dNz [\text{mm}] = dNz [\text{m}] \times 1000 \quad (4.9)$$

Both formulas of the ElFiBU-correlation for the estimation of the generation of positive (Eq. 4.6) and negative fields (Eq. 4.7) give an electric field value in the SI-unit V/m.

#### **4.2.8 Conclusions**

Experimental results obtained by Pro-Science/KIT during the DisCha-experiments in the frame of PRESLY project, were used to develop empirical correlations estimating the electrostatic field built-up during hydrogen releases through a nozzle with circular aperture. The empirical correlations can be applicable for hydrogen releases with temperature down to 80 K, initial pressure up to 200 bar, and nozzle diameter within range 0.5-4 mm.

## 5 Combustion

This chapter presents the engineering correlations and tools developed to evaluate the hazards associated to combustion of cryogenic, including liquid, hydrogen releases.

### 5.1 Laminar burning velocity and expansion ratios for hydrogen-air mixtures (INERIS)

The method proposed by INERIS includes graphs and correlations on the evolution of the laminar burning velocity of the flame and expansion ratio of combustion for hydrogen air mixtures as function of the fuel/air ratio and of the temperature. The pressure is atmospheric.

#### 5.1.1 Introduction

The purpose of this assessment is to provide graphical information and correlations to estimate the influence of temperature on the laminar burning velocity of the flame and on the expansion ratio of the combustion for hydrogen air mixtures at various fuel air ratios and at atmospheric pressure. The ranges of variations are intended to represent those potentially occurring during a leakage of liquid hydrogen.

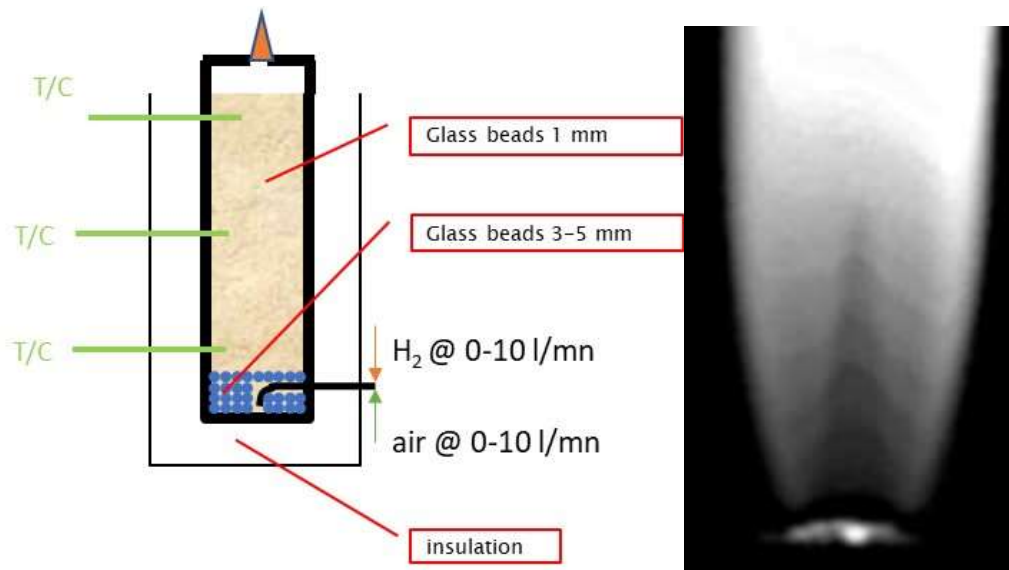
#### 5.1.2 Nomenclature

Table 32. Nomenclature for the assessment of combustion parameters.

Parameter	Symbol	Unit
Maximum laminar burning velocity at T	$Slmax_T$	m/s
Maximum laminar burning velocity at $T_{ref}$	$Slmax_{Tref}$	m/s
Expansion ratio at T	$Exp_T$	-
Expansion ratio at $T_{ref}$	$Exp_{Tref}$	-
Temperature	$T$	K
Reference temperature	$T_{ref}$	K

#### 5.1.3 Model description

The laminar burning velocity was measured using the burner method (Bouvet et al., 2011). In this specific situation for which low temperatures are needed a special design was developed (Proust C., 2021). The flammable mixture, which composition can be carefully controlled using mass flowmeters, flows through a thick bed of glass beads before reaching the exit nozzle (Figure 26). To obtain low temperatures, the glass beads are cooled down by pouring liquid nitrogen. The burner mouth is a profiled nozzle (4 mm diameter) with a discharge coefficient of about 0.85. A further difficulty is that the flame is transparent. To capture the flame front infrared films were done, pictures were converted in grey scale and added up to improve the contrast (Figure 26).



**Figure 26.** Burner used to measure the laminar burning velocity (left) and intensified IR picture of the flame (right 50% H<sub>2</sub> @ -85°C).

The evolution of the measured laminar burning velocity as function of the temperature and of the mixture composition is shown on Figure 27.

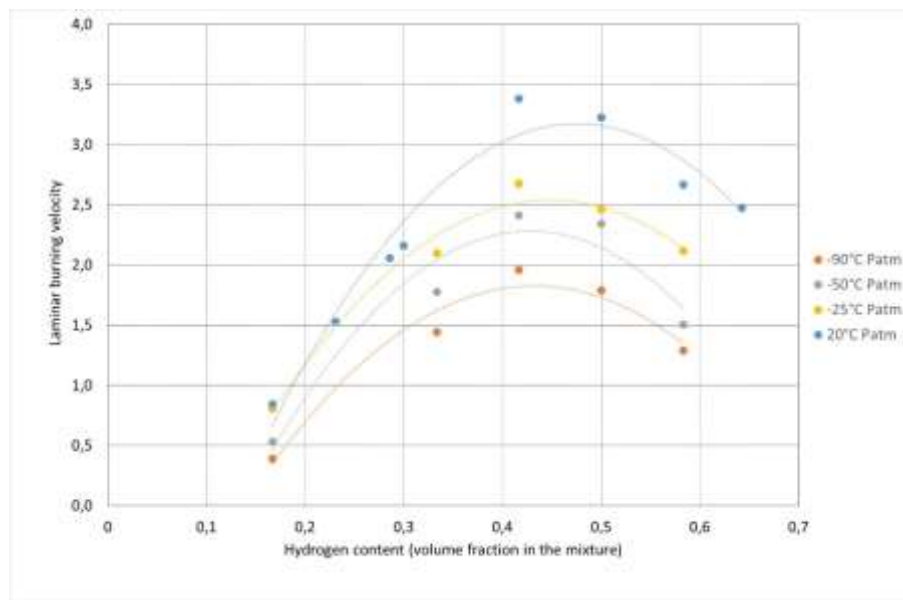


**Figure 27.** Evolution of the laminar burning velocity as function of the temperature and of the mixture composition.

At ambient temperature, the measured laminar burning velocities are in line with other measurements (Pareja et al., 2010) and measurements at higher temperatures by Liu and Mc Farlane (1983). Note that the maximum laminar burning velocity correlates correctly with the following power law in the temperature range -100°C to +250°C:

$$\frac{Slmax_T}{Slmax_{Tref}} = \left( \frac{T}{T_{ref}} \right)^{1.48} \quad (5.1)$$

where  $Slmax_T$  is the maximum laminar burning velocity at temperature T (in K) and  $Slmax_{Tref}$  is the maximum laminar burning velocity at the reference temperature  $T_{ref}$  (in K). Atmospheric pressure is considered.

*The expansion ratio* was calculated using a thermodynamic equilibrium code used at CEA (Gordon and McBride, 1994). The code minimizes the Gibbs energy of the products while conserving the enthalpy of the mixture (adiabatic combustion at constant pressure). The perfect gas law was used and the chosen final combustion products are H<sub>2</sub>O, OH, O, N, H, NO, O<sub>2</sub>, N<sub>2</sub>, H<sub>2</sub>. The simulations are done on the basis of 1 kg of mixture. The expansion ratio is the ratio between the volumes of the mixture before the combustion and after. Note that it is different from the ratio of the temperatures because of the variations of the change in the number of moles. The results are presented in Figure 28.

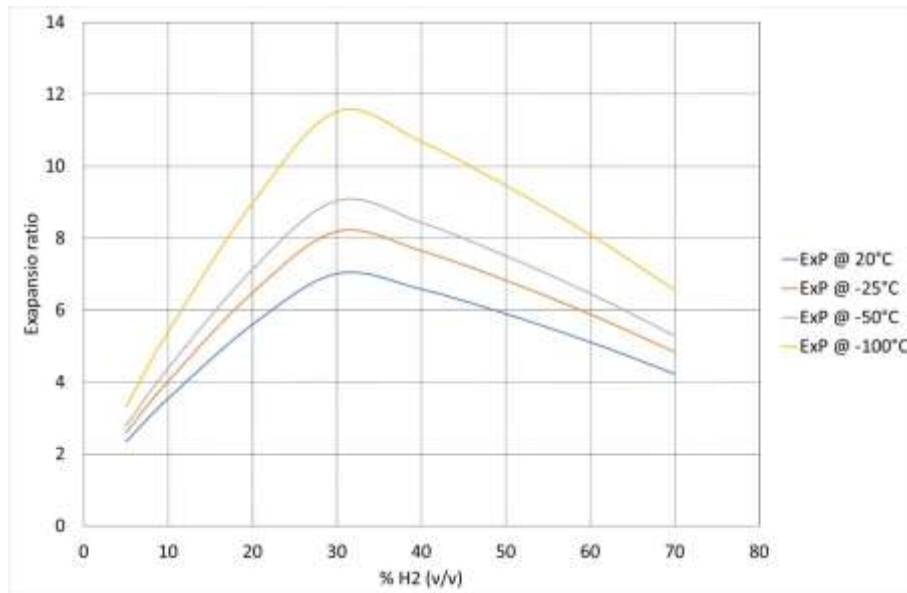


**Figure 28. Evolution of the expansion ratio of the combustion as function of the temperature and of the mixture composition.**

The theory of the adiabatic combustion tells that the expansion ratio should vary proportionally to the invers of the absolute temperature:

$$\frac{Exp_T}{Exp_{Tref}} = \frac{T_{ref}}{T} \quad (5.2)$$

where  $Exp_T$  is the expansion ratio at temperature T (in K) and  $Exp_{Tref}$  is the expansion ratio at the reference temperature  $T_{ref}$  (in K). Atmospheric pressure is considered. Proportionality is approximately true.

#### 5.1.4 Validity range

The graphical values and correlations are valid in the temperature range -100°C to ambient and at atmospheric pressure.

#### 5.1.5 Calculation procedure

The temperature and concentration of hydrogen in the mixture are required as input values. The output values of laminar burning velocity and the expansion ratio can be either calculated solving the algebraic equations by hand, or can be retrieved graphically from Figure 27 and Figure 28. Any self-coherent unit system can be used. But in the present report SI units were used.

#### 5.1.6 Conclusions

Graphical information and correlations are established to estimate the influence of the temperature on the laminar burning velocity of the flame and of the expansion ratio of the

combustion for hydrogen air mixtures at various fuel air ratios and at atmospheric pressure. The ranges of variations are intended to represent those potentially occurring during a leakage of liquid hydrogen.

### 5.1.7 References

Bouvet N., Chauveau C., Gökalp, Lee S.Y., Santoro R.J. (2011), Characterization of syngas laminar flames using the Bunsen burner configuration, International Journal of Hydrogen Energy, Volume 36, Pages 992-1005

Liu D.D.S., Mc Farlane R. (1983), Laminar burning velocities of hydrogen-air and hydrogen-air-steam flames, Combustion and Flame, volume 49, pages 59-71.

Gordon S., McBride B. J. (1994), Computer program for calculation of complex chemical equilibrium compositions and applications, Part 1: Analysis, NASA reference publication 1311.

Pareja J., Burbano H.J., Ogami Y (2010), Measurements of the laminar burning velocity of hydrogen-air premixed flames, International Journal of Hydrogen Energy, Volume 35, Pages 1812-1818.

Proust C. (2021), Summary of experiment series E4.1 results (Ignition parameters), Deliverable D21, EU Project Pre-normative REsearch for Safe use of Liquid Hydrogen (PRESLY), FCH 2 JU, Grant Agreement N. 779613.

## 5.2 Flame length correlation and hazard distances for jet fires (UU)

### 5.2.1 Introduction

The dimensionless correlation for hydrogen jet flames calculates the flame length knowing the storage conditions. In a second section of the analysis, the temperature distribution along the axis of hydrogen jet fires is compared to harm criteria for people to calculate the associated hazard distances.

### 5.2.2 Nomenclature

Table 33 reports the nomenclature employed for the dimensionless flame correlation.

**Table 33. Nomenclature for the dimensionless jet flame correlation.**

Parameter	Symbol	Unit
Flame length	$L_f$	m
Diameter	$d$	m
Density of hydrogen at the nozzle	$\rho_N$	kg/m <sup>3</sup>
Density of the surroundings	$\rho_s$	kg/m <sup>3</sup>
Velocity at the nozzle	$u_N$	m/s
Speed of sound	$C_N$	m/s
Distance	x	m
No harm (70°C) hazard distance	$X_{70}$	m
Pain limit (5 mins, 115°C) hazard distance	$X_{115}$	m
Third degree burns (20 sec, 309°C) hazard distance	$X_{309}$	m

### 5.2.3 Model description

The dimensionless flame length correlation is described in detail in Molkov and Saffers (2013). The correlation is valid for laminar and turbulent flames, buoyancy - and

momentum-controlled fires, expanded (subsonic and sonic) and under-expanded (sonic and supersonic) jet fires.

The flame length normalized to the release diameter ( $\frac{L_f}{d}$ ) depends only on the release conditions at the nozzle exit, i.e. density and velocity, the corresponding speed of sound and the density of the surrounding air grouped in the following dimensionless quantity:

$$X = \frac{\rho_N}{\rho_s} \cdot \left( \frac{u_N}{C_N} \right)^3 \quad (5.3)$$

Figure 29 shows the dimensionless hydrogen flame length correlation against the experimental data employed for a validation of the tool in Molkov and Saffers (2013) and in Cirrone et al. (2019). Parameters at the nozzle exit can be calculated through the under-expanded jet theory developed at Ulster and validated as well against the cryogenic releases included in the validation range of the flame correlation.

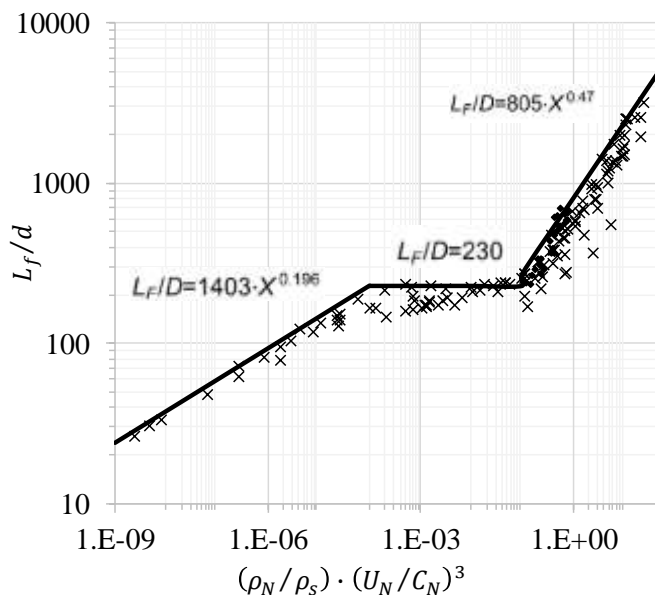


**Figure 29. The dimensionless correlation for hydrogen jet flames: “+” data from Molkov and Saffers (2013); “♦” data from Cirrone et al. (2019).**

Molkov (2012) compared the distribution of axial temperature along the axis, measured in experiments on vertical hydrogen jet fires by Imamura et al. (2008), Barlow and Carter (1996) and LaChance (2010), as function of the distance normalised to the flame length against three harm criteria defined by Lachance (2010). It was found that hazard distances can be defined as follows:

- No harm (70°C) hazard distance,  $X_{70} = 3.5L_f$ ;
- Pain limit (5 mins, 115°C) hazard distance,  $X_{115} = 3L_f$ ;
- Third degree burns (20 sec, 309°C) hazard distance,  $X_{309} = 2L_f$ .

The tool is available on e-laboratory platform developed within Net-Tools (<https://elab-prod.iket.kit.edu/>). Thanks to the studies performed within PRESLHY, this tool is validated as well against releases at cryogenic temperature (see Cirrone et al., 2019).

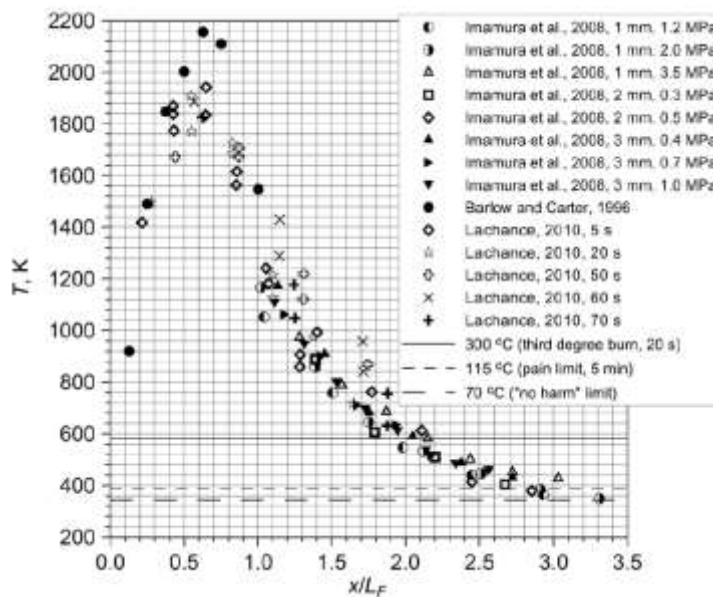


**Figure 30. Measured axial temperature as a function of distance normalised to the flame length, and three criteria for jet fire effects (Molkov, 2012).**

#### 5.2.4 Validity range

The dimensionless correlation for hydrogen jet flames was validated against jet fires with pressure in the range 10-900 bar and temperature in the range 187-300 K (Molkov and Saffers, 2013). Cirrone et al. (2019) expanded the validation of the correlation to jet fires with release temperature down to 46 K for pressure in the range 2-6 bar abs against experiments by Panda and Hecht (2017). The latter validation study was conducted within PRESLHY research programme.

#### 5.2.5 Input values

Table 34 reports the parameters required as input for the model. The column input value reports an example of calculations to test the tool once implemented on the platform.

**Table 34. Input parameters for the dimensionless jet flame correlation.**

Parameter	Symbol	Input value	Unit	Limits (min-max)	Defaults
Storage temperature	$T$	80	K	50-300	293
Storage pressure	$P$	$20 \cdot 10^6$	Pa	1-1000	350
Release diameter	$d$	0.002	m	0.0001-0.2	0.002
Ambient temperature	$T_{amb}$	288	-	233-313	293
Ambient pressure	$P_{amb}$	101325	Pa	33700-107900	101325

#### 5.2.6 Output values

Table 35 reports the output parameters of the tool.

**Table 35. Output parameters for the dimensionless jet flame correlation.**

Parameter name	Symbol	Output value	Unit
Flame length	$L_f$	6.65	m
No harm (70°C) hazard distance	$X_{70}$	23.07	m
Pain limit (5 mins, 115°C) hazard distance	$X_{115}$	19.95	m
Third degree burns (20 sec, 309°C) hazard distance	$X_{309}$	13.30	m

### 5.2.7 Conclusions

The dimensionless correlation for hydrogen flame length was found to be applicable for cryogenic hydrogen jet fires with release temperature down to 46 K for pressure in the range 2-6 bar abs. The model includes calculation of the distances to the harm levels defined in LaChance (2010) as function of the jet flame length.

### 5.2.8 References

- Barlow, R.S. and Carter, C.D. (1996), Relationships among Nitric Oxide, Temperature, and Mixture Fraction in Hydrogen Jet Flames, *Combustion and Flame*, 104:288.
- Cirrone, D., Makarov, D., Molkov, V. (2019), Cryogenic Hydrogen Jets: Calculation of Hazard Distances. International Conference on Hydrogen Safety, 24th-26th September 2019, Adelaide, Australia.
- Imamura, T., Hamada, S., Mogi, T., Wada, Y., Horiguchi, S., Miyake, A., et al. (2008), Experimental Investigation on the Thermal Properties of Hydrogen Jet Flame and Hot Currents in the Downstream Region, *International Journal of Hydrogen Energy*, 33, pp. 3426-3435.
- LaChance, J.L. (2010), Progress in Risk Assessment Methodologies for Emerging Hydrogen Applications. In: Sixth international short course and advanced research workshop “Progress in hydrogen safety e regulations, codes, and standards”, 25-29 January 2010, Belfast, Northern Ireland, UK.
- Molkov, V. (2012), Fundamentals of Hydrogen Safety Engineering I, Free-download electronic book available at [www.bookboon.com](http://www.bookboon.com), 2012. Download free books at bookboon.com.
- Molkov, V. and Saffers, J. B. (2013), Hydrogen Jet Flames, *International Journal of Hydrogen Energy*, vol. 38, no. 19, pp. 8141–8158.
- Panda, P. P. and Hecht, E. S. (2017), Ignition and Flame Characteristics of Cryogenic Hydrogen Releases, *International Journal of Hydrogen Energy*, vol. 42, no. 1, pp. 775–785.

## 5.3 Assessment of thermal load from hydrogen jet fires (UU)

### 5.3.1 Introduction

The reduced tool shown in the present section aims at the assessment of the radiative heat flux in the surrounding of hydrogen jet fires from vertical and horizontal releases of hydrogen at ambient and cryogenic temperature. The reduced tool is based on the weighted multi source flame radiation model developed by Hankinson and Lowesmith (2012) and further expanded by Ekoto et al. (2014) for application to large scale flames. Within the framework of PRESLHY project, UU adapted the model to include evaluation of flame length and width through the dimensionless correlation presented in Section 5.2 and expand the validation range to cryogenic hydrogen jet fires.

### 5.3.2 Nomenclature

Table 36 reports the nomenclature and parameters employed for the model.

**Table 36. Nomenclature for reduced model to evaluate radiative heat flux from a hydrogen jet fire.**

Parameter	Symbol	Unit
Adiabatic flame temperature	$T_{ad}$	K
Density	$\rho$	kg/m <sup>3</sup>
Diameter	$d$	m
Flame length	$L_f$	m/s
Flame residence time	$t_f$	ms
Flame width	$W_f$	m
Gas heat of combustion	$\Delta H_c$	MJ/kg
Mass flow rate	$\dot{m}$	kg/s
Plank's mean absorption coefficient for the product species	$\alpha_f$	1/m
Pressure	$p$	Pa
Radiant fraction	$\chi$	-
Stoichiometric mass fraction of hydrogen	$Y_s$	-
Stoichiometric molecular weight of the hydrogen combustion products in air	$MW_{st}$	g/mol
Surface emissive power	$S$	W
Temperature	$T$	K
Thermal dose	$TD$	[ $(\text{kW}/\text{m}^2)^{4/3}\text{s}$ ]
Universal gas constant	$R_u$	g/(mol·K)

### 5.3.3 Model description

The model used for the prediction of radiative heat flux from hydrogen jet fires is based on the weighted multi source flame radiation model developed by Hankinson and Lowesmith (2012).

The methodology requires the knowledge of hydrogen parameters at the real nozzle, which can be evaluated through the under-expanded jet theory described in section 3.1.3, which has been validated as well against the cryogenic releases included in the range of the present reduced tool.

The radiative heat flux prediction starts from the evaluation of the radiant fraction  $\chi$ , which is the ratio of the energy effectively emitted by the flame as radiation and the chemical energy associated to the fuel stream. This parameter is strictly dependent on the fuel and is usually derived from experimental considerations and correlations. The expression of radiant fraction used in the model was derived by Molina et al. (2007):

$$\chi = 0.08916 \cdot \log_{10}(t_f \cdot \alpha_f \cdot T_{ad}^4) - 1.2172 \quad (5.4)$$

where  $t_f$  is the flame residence time (ms),  $\alpha_f$  is the Plank's mean absorption coefficient for water vapour, assumed to be equal to  $0.23 \text{ m}^{-1}$  based on study by Ekoto et al. (2014), and  $T_{ad}$  is the adiabatic flame temperature, which is assumed to be 2390 K for hydrogen combustion in air.

The radiant fraction depends on the considered substance and on the jet and flame characteristics through the flame residence time  $t_f$ , which is evaluated using Turns and Myhr (1991) equation:

$$t_f = \frac{\pi}{12} \frac{\rho_f \cdot W_f^2 \cdot L_f \cdot Y_s}{\dot{m}} \quad (5.5)$$

where  $Y_s$  is the hydrogen stoichiometric mass fraction ( $Y_s = 0.0281$ ),  $L_f$  is the visible flame length,  $W_f$  is the visible flame width,  $\dot{m}$  is the mass flow rate of hydrogen and  $\rho_f$  is the flame density.

The flame length is evaluated through the dimensionless correlation presented in Section 5.2, whereas the flame width is calculated as  $W_f \approx 0.17 \cdot L_f$ , following observations by Schefer et al. (2006) and Houf et al. (2007). The flame density is evaluated through the following expression:

$$\rho_f = \frac{P_{amb} \cdot MW_{st}}{R_u \cdot T_{ad}} \quad (5.6)$$

where  $P_{amb}$  is the ambient pressure,  $MW_{st}$  is the stoichiometric molecular weight of the hydrogen combustion products in air ( $MW_{st} = 24.52$  g/mol) and  $R_u$  is the universal gas constant ( $R_u = 8314.47$  g/(kmol·K)).

The model treats the flame as an emitting body with surface emissive power  $S$ :

$$S = \chi \cdot \dot{m} \cdot \Delta H_c \quad (5.7)$$

where  $\Delta H_c$  is the gas heat of combustion ( $\Delta H_{c,H_2O} = -119$  MJ/kg).

The portion of radiation emitted by the flame and reaching the target depends on its location, expressed through the view factor  $VF$ , and the amount of radiation absorbed in the path from the flame to the target, which is function of the atmospheric transmissivity  $\tau$ ; the radiative heat flux reaching the target is evaluated as:

$$q = \frac{VF}{A_f} \cdot S \cdot \tau \quad (5.8)$$

The weighted multi source model consists in the decomposition of the jet flame axis in  $N$  emitting points, with  $N$  decided accordingly to the characteristics of the problem. Full description of the approach is given in Hankinson and Lowesmith (2012). Each point along the flame is considered as a radiation emitter and has a different contribution on the final balance of the heat flux, expressed as:

$$\tau \frac{VF}{A_f} = \sum_{i=1}^N \frac{w_i \cdot \cos \varphi_i}{4 \cdot \pi \cdot r_i^2} \cdot \tau_i \quad (5.9)$$

where  $r_i$  is the distance between the observer and the point source,  $\varphi_i$  is the angle between the observer unit normal and the  $i$ -emitter,  $w_i$  is the emitter strength parameter and  $\tau_i$  is the atmospheric transmissivity related to the point source  $i$ . Figure 31 shows a visual representation of the flame decomposition in  $N$  points and geometrical parameters incurring into the evaluation of radiative heat flux at the receiver.

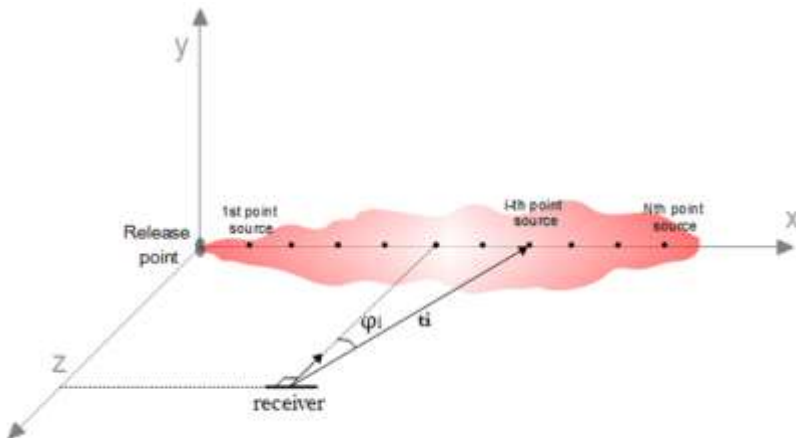


**Figure 31. Visual representation of the weighted multi source model.**

The contribution of each point  $i$  has been quantified through  $w_i$ , which depends on the position of the point along the jet flame axis because the emission of heat radiation is not uniform as proved by measurements made on large scale jet fires. The weighting of the points was simplified, supposing a linear increase of source emitter contribution if located between the point of release and  $0.6L_f$ , individuated by the point  $n=0.6N$ , and a linear decrease if the point is located in the remaining part of the jet flame axis:

$$w_i = i \cdot w_1, \text{ if } i \leq n = 0.6 \cdot N$$

$$w_i = \left[ n - \frac{n-1}{N-n-1} (i - n - 1) \right] \cdot w_i, \text{ for } i > n = 0.6 \cdot N \quad (5.10)$$

$$\sum_{i=1}^N w_i = 1$$

The transmissivity in air is estimated through the empirical method by Wayne (1991):

$$\tau = 1.006 - 0.01171 [\log_{10} X(H_2O)] - 0.02368 [\log_{10} X(H_2O)]^2 - 0.03188 [\log_{10} X(CO_2)] + 0.001164 [\log_{10} X(CO_2)]^2 \quad (5.11)$$

where  $X(CO_2)$  is a function representing the amount of carbon dioxide in the path, and  $X(H_2O)$  is a corresponding function for water vapour, evaluated as:

$$X(CO_2) = L \left( \frac{273}{T} \right) \quad \text{and} \quad (H_2O) = R_H LS_{mm} \left( \frac{288.651}{T} \right) \quad (5.12)$$

where  $L$  is the path length (m),  $R_H$  is the fractional relative humidity,  $S_{mm}$  is the saturated vapour pressure of water at atmospheric temperature  $T$  (mmHg).

The total radiative heat flux at the receiver is given by:

$$q = \sum_{i=1}^N \frac{w_i \cdot \cos \beta_i}{4 \cdot \pi \cdot D_i^2} \cdot \tau_i \cdot S \quad (5.13)$$

The thermal dose is a comprehensive parameter calculating the level of harm as a function of the exposure duration ( $t$ , s) in addition to the incident radiative heat flux ( $I$ , kW/m<sup>2</sup>). It is expressed in terms of thermal dose (TD) and measured in [(kW/m<sup>2</sup>)<sup>4/3</sup>s]:

$$TD = \int_0^t I(t)^{4/3} dt. \quad (5.14)$$

### 5.3.4 Validity range

The reduced tool for hydrogen jet flames was validated against jet fires with pressure in the range 2-900 bars and temperature in the range 48-315 K. Table 37 reports the detailed

parameters for the experiments used for validation of the model to evaluate the radiative heat flux from hydrogen jet fires. The model has been validated against radiative heat flux measurements on the side of jet fires up to a distance of 5 m. The maximum radiative heat flux and distribution along the flame is well represented by the model. However, it was observed that sensors with coordinate tending towards the flame length may be not accurately reproduced, and this is believed to be due to calculation of geometrical angles for the view factor. See details in following section for the model validation process.

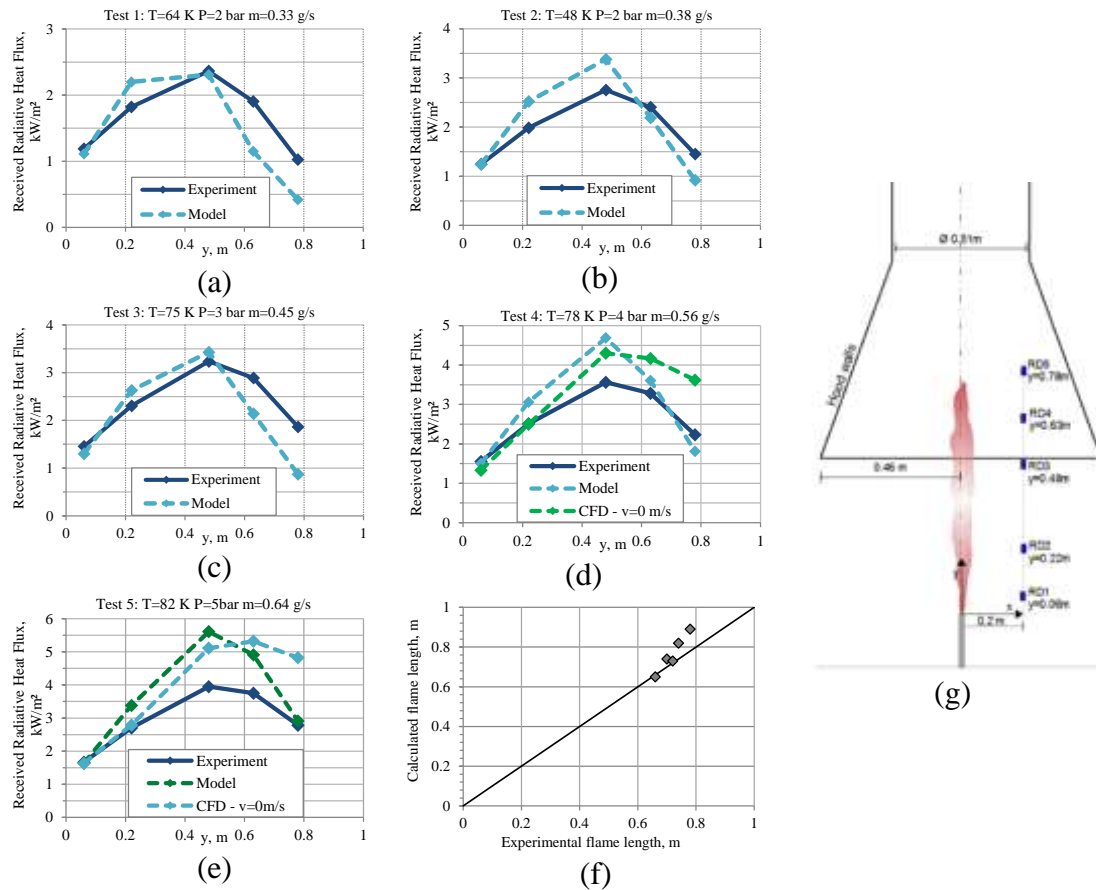
**Table 37. Experiments for the validation of the model to evaluate radiative heat flux.**

Series name	Temperature, K	Pressure, bar	Diameter, mm	N. Tests	Reference
SNL	48-82	2-5	1.25	5	Panda and Hecht (2017)
KIT	80, 290	3-20	2, 4	6	Breitung et al. (2009)
INERIS	315	900	2.0	1	Proust et al. (2011)

#### 5.3.4.1 Validation against experimental tests on hydrogen jet fires

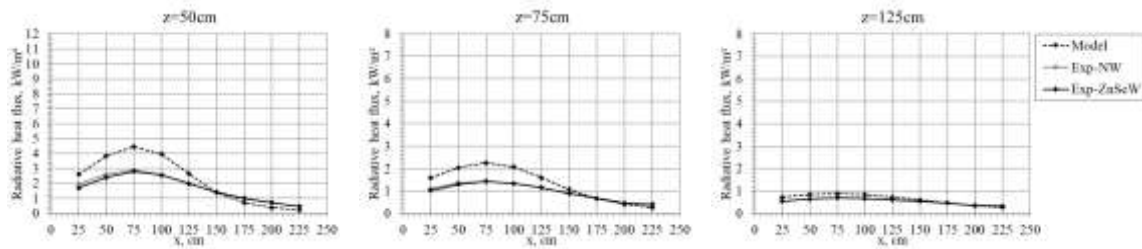
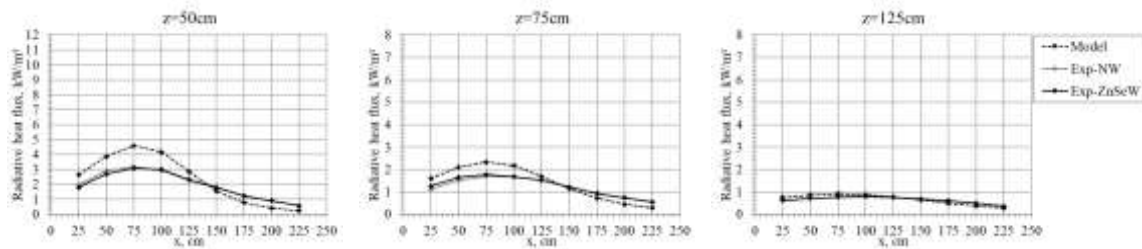
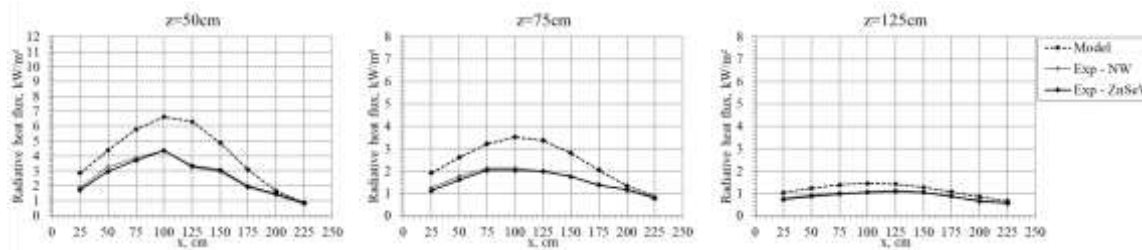
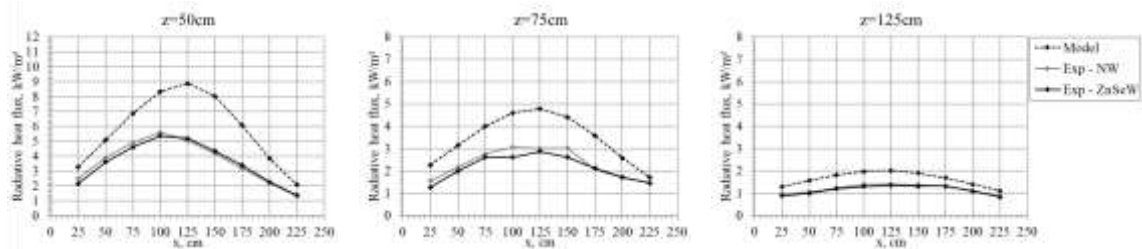
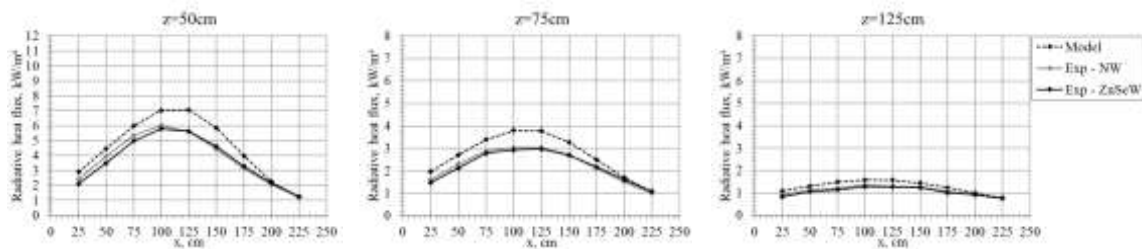
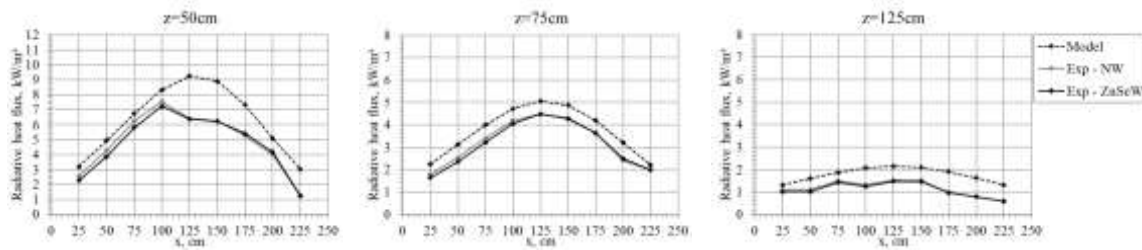
Three experimental series for a total of 12 tests were used to validate the engineering model to assess the radiative heat flux from hydrogen jet fires.

Figure 32a-e show the comparison between the modelled radiative heat flux and experimental measurements at the five sensors located as in Figure 32g. The model well predicts the experimental radiative heat flux in the first portion of the jet fire for all Tests. Tests 1-3 (Figure 32a-c) show a significant underprediction for the furthest sensor from the release point. This is caused by the sensor RD5 coordinate which is approximately the same of the flame length, and given that it is very close to the jet axis (0.2 m), it leads to an inaccurate view factor estimation when the weighted multi source model is applied. Maximum experimental radiative heat flux for Tests 4 and 5 is overpredicted by the model, see Figure 32d-e. To explain this deviation, it should be remarked that the experimental facility was provided with a hood extracting combustion products. The extraction velocity at the hood was proportional to the released hydrogen mass flow rate, which is greater for Tests 4 and 5. Therefore, in these tests a greater effect of extraction velocity on maximum radiative heat flux recorded experimentally is expected, as a larger part of combustion products emitting radiation will be removed. This effect is proven by CFD modelling previously validated against SNL experiments in Cirrone et al. (2019a). Here, results by CFD simulations for hood velocity equal to 0 m/s are reported and compared to estimation by the engineering tool. It is possible to see that in this case the engineering tool well reproduces the maximum recorded in simulations.



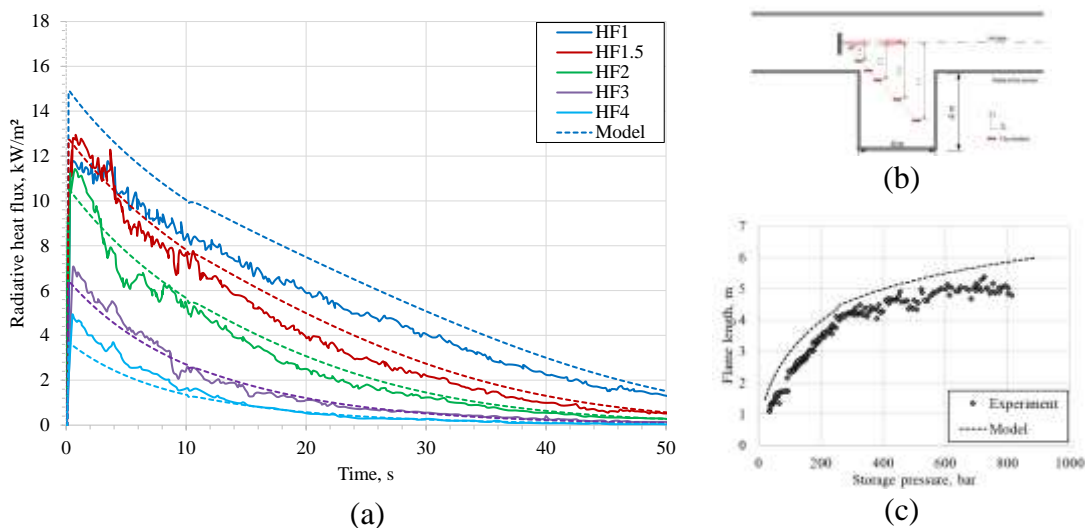
**Figure 32. Validation of the model against SNL tests: a-e) calculated versus experimental radiative heat flux for Tests 1-5; f) calculated versus experimental flame length for Tests 1-5; g) scheme of the experimental set-up including sensors' location.**

The second set of experiments used for validation of the model are those carried out by Breitung et al. (2009) on jet fires with ambient and cryogenic storage temperature. Nine radiative heat flux sensors were located on three lines parallel to the jet axis at distances  $z=50, 75$  and  $125\text{ cm}$ . The nine sensors on a same line had distance  $25\text{ cm}$  from each other. Release characteristics were calculated as in Cirrone et al. (2021). Figure 33 shows the comparison between experimental and calculated radiative heat flux for the six tests. Experimental measurements for Tests 1 and 2 on hydrogen release at ambient temperature and Tests 5 and 6 at cryogenic hydrogen temperature are well reproduced by the engineering tool. Tests 3 and 4 experimental measurements are overestimated by the analytical model. This could be due to the associated overestimation of flame length up to approximately 20%. Overall, for these tests the engineering tool produces a conservative estimation.

**Test 1: T=290 K, P=4 bar, d=2 mm**

**Test 2: T=290 K, P=4 bar, d=2 mm**

**Test 3: T=80 K, P=14 bar, d=2 mm**

**Test 4: T=80 K, P=20 bar, d=2 mm**

**Test 5: T=80 K, P=3 bar, d=4 mm**

**Test 6: T=80 K, P=4 bar, d=4 mm**


**Figure 33. Validation of the model against KIT tests: calculated versus experimental radiative heat flux.**

The model has been validated as well against experiments on a transient hydrogen jet fire at high pressure carried out in Proust et al. (2007). Hydrogen was released from a 25 L storage tank at initial ambient temperature and pressure of 900 bar. Release nozzle was equal to 2 mm. The adiabatic-to-isothermal blowdown model was used to estimate hydrogen parameters at the real nozzle (see Cirrone et al., 2019b). Figure 34a shows the comparison between the calculated and experimental radiative heat flux measured at five different sensors located as Figure 34b. The model well predicts the transient of radiative heat flux following the flame length decrease in time due to the tank depressurization. There is a discrepancy of the model prediction and experiments at sensor HF1 which is the closest to the flame. However, it is possible to observe that in the initial phase of the experiments, heat flux measured at 1 m from the flame is lower than the value measured at 1.5 m from the flame (HF1.5) and approximately the same of measurement at 2 m (HF2). This is ought to be associated to the flame development in the initial stage of the release. Experimental observations on ignition of high pressure gas releases shown a spherical broadening of the jet fire head during the first stage of the release (0–400 ms) that is characterised by intense radiation, see Studer et al. (2009) and Kessler et al. (2014). The model instead considers an established flame since the beginning of the release. Figure 34c shows that the predicted flame length well estimates experimental measurements during the tank blowdown and test duration.



**Figure 34. Validation of model against INERIS test:** a) calculated versus experimental radiative heat flux; b) position of radiometers with respect to the flame; c) flame length prediction during storage tank blowdown.

### 5.3.5 Input values

Table 38 reports the parameters required as input for the model. The column input value reports an example of calculations to test the tool once implemented on the platform.

**Table 38. Input parameters and associated details.**

Parameter	Symbol	Input value	Unit	Limits (min-max)	Defaults
Storage temperature	$T$	75	K	48-300	293
Storage pressure	$P$	$3 \cdot 10^5$	Pa	$2 \cdot 10^5$ - $900 \cdot 10^5$	350
Release diameter	$d$	0.00125	m	0.001-0.004	0.002
Ambient temperature	$T_{amb}$	288	K	288-313	293
Ambient pressure	$P_{amb}$	101325	Pa	100000-107900	101325
Jet direction	$n$	[0,1,0]	-	[0,0,0]-[1,1,1]	[0,1,0]
Receiver location	$x$	[0.2,0.48,0]	m	[0,0,0]- [100,100,100]	[0.2,0.5,0]
Exposure time	$t$	20	s	0.1-1000	20

### 5.3.6 Output values

Table 39 reports the output that will be returned from the model applied to the test conditions reported in Table 38.

**Table 39. Output parameters and associated details.**

Parameter name	Symbol	Output value	Unit
Flame length	$L_f$	0.73	m
Radiative heat flux	$q$	3.43	kW/m <sup>2</sup>
Thermal dose	$TD$	103.46	[(kW/m <sup>2</sup> ) <sup>4/3</sup> s]

### 5.3.7 Conclusions

The presented reduced model assesses the thermal radiative heat flux emitted from cryogenic hydrogen jet fires. Once the conditions of the release are known, the model permits the calculation of the radiative heat flux and thermal dose received at a certain position with respect to the jet fire and for a certain exposure duration. The thermal model can be extended to the calculation of hazard distances according to harm criteria available in literature.

### 5.3.8 References

- Breitung, W., Stern, G., Veser, A., Friedrich, A., Kutznetsov, M., Fast, G., Oechsler, B., Kotchourko, N., Travis, J.R., Xiao, J., Schwall M. (2009), Final Report: Experimental and theoretical investigations of sonic hydrogen discharge and jet flames from small breaks.
- Cirrone, D., Makarov, D., Molkov, V. (2019a), Thermal radiation from cryogenic hydrogen jet fires, International Journal of Hydrogen Energy 44 (17), 8874-8885.
- Cirrone, D., Makarov, D., Molkov, V. (2019b), Simulation of thermal hazards from hydrogen under-expanded jet fire, International Journal of Hydrogen Energy 44 (17), 8886-8892.
- Cirrone, D., Makarov, D., Kuznetsov, M., Friedrich, A., Molkov, V. (2021), Effect of heat transfer through the release pipe on simulations of cryogenic hydrogen jet fires and hazard distances, submitted to International Conference on Hydrogen Safety, Edinburgh, Scotland.

- Ekoto, I.W., Ruggles, A.J., Creits, L.W., Li, J.X. (2014) Updated jet flame radiation modelling with buoyancy corrections, International Journal of Hydrogen Energy 39, 20570-20577.
- Hankinson, G. and Lowesmith, B.J. (2012) A consideration of methods of determining the radiative characteristics of jet fires. Combustion and Flame, 159 (3), 1165 - 1177.
- Houf, W. and Schefer, R. (2007) Predicting radiative heat fluxes and flammability envelopes from unintended releases of hydrogen, International Journal of Hydrogen Energy 32, 136-151.
- Kessler, A., Schreiber, A., Wassmer, C., Deimling, L., Knapp, S., Weiser, V., et al. (2014) Ignition of hydrogen jet fires from high pressure storage, International Journal of Hydrogen Energy 39 (35), 20554-20559.
- Molina, A., Schefer, R.W. and Houf, W.G. (2007) Radiative fraction and optical thickness in large-scale hydrogen-jet fires, Proceedings of the Combustion Institute 31, 2565-2572.
- Panda, P. P. and Hecht, E. S. (2017) Ignition and Flame Characteristics of Cryogenic Hydrogen Releases, International Journal of Hydrogen Energy 42 (1), 775–785.
- Schefer, R.W., Houf, W.G., Bourne, B., Colton, J. (2006) Spatial and radiative properties of an open-flame hydrogen plume, International Journal of Hydrogen Energy 31, 1332-1340.
- Studer, E., Jamois, D., Jallais, S., Leroy, G., Hebrard, J., Blanchetière, V. (2009) Properties of large-scale methane/hydrogen jet fires, International Journal of Hydrogen Energy 34 (23), 9611-9619.
- Turns, S.R. and Myhr, F.H. (1991) Oxides of nitrogen emissions from turbulent jet flames: Part I -Fuel Effects and Flame Radiation, Combustion and Flame 87, 319–335.
- Wayne, F. D. (1991) An economical formula for calculating atmospheric infrared transmissivities, Journal of Loss Prevention in the Process Industries 4, Issue 2, 86-92.

## 5.4 Maximum pressure load from delayed ignition of turbulent jets (UU)

### 5.4.1 Introduction

The delayed ignition of a highly turbulent under-expanded hydrogen jet may cause a strong deflagration. The generated overpressure can seriously harm people and damage civil structures. The semi-empirical correlation presented here aims at predicting the maximum overpressure generated by delayed ignition of a hydrogen jet at an arbitrary location for known storage pressure and release diameter. The correlation is applicable only to free jets in open atmosphere.

### 5.4.2 Nomenclature

Table 40 reports the nomenclature used in the correlation.

**Table 40. Nomenclature for correlation on pressure load from delayed ignition of a turbulent jet.**

Parameter	Symbol	Unit
Nozzle diameter	$d$	m
Expansion coefficient	$E_i$	-
Ambient pressure	$P_0$	Pa
Storage pressure	$P_s$	Pa
Distance between the centre of the fast burning mixture in the jet (25-35% by volume) and the target location	$R_w$	m

Ambient temperature	$T_0$	K
Storage temperature	$T_s$	K
Receiver coordinates	$(x_t, y_t, z_t)$	m
Overpressure	$\Delta P_{exp}$	Pa

#### 5.4.3 Model description

The model assumes that the maximum overpressure is generated by the portion of jet with the fast burning mixture (25-35% H<sub>2</sub> by vol). The location in the jet with concentration equal to 30% by vol of hydrogen in air is assumed to be the centre of the mixture that will deflagrate and generate the maximum overpressure. This concentration corresponds indeed to the maximum flame speed taking into account combustion instabilities as in (Verbecke et al., 2009).

The location of this centre was calculated using the similarity law for momentum expanded (Chen and Rodi, 1980) and under-expanded jets (Molkov, 2012):

$$x_{30\%} = 5.4 \sqrt{\frac{\rho_N}{\rho_S}} D \frac{c_N}{c_{30\%}}. \quad (5.15)$$

The distance between the centre of the 25-35% flammable cloud and the pressure sensor (in experiment) or “target” (person or structure) location is defined as  $R_w$ , and it can be calculated as:

$$R_w = \sqrt{(x_{30\%} - x_t)^2 + (y_{30\%} - y_t)^2 + (z_{30\%} - z_t)^2} \quad (5.16)$$

The similitude analysis has been applied to build a correlation. The dimensionless overpressure generated by delayed ignition of hydrogen jets at an arbitrary location,  $\Delta P_{exp}/P_0$ , is correlated to the dimensionless parameter composed of the product of the ratio of the dimensionless storage pressure,  $\sqrt{P_s/P_0}$ , and the square of ratio of release diameter to the distance between the centre of the fast burning mixture in the jet (25-35% by volume) and the target location,  $(d/R_w)^2$ .

The generated overpressure is strongly affected by the ignition delay and ignition point location. The ignition location obviously determines whether ignition verifies in a hydrogen rich or lean portion of the jet, affecting combustion and generated overpressure. The ignition delay determines if ignition of the hydrogen jet takes place in a more or less unsteady and turbulent portion of the jet. As an example, HSL-1 tests recorded overpressures that goes from a minimum of 3.7 kPa for an ignition delay of 400 ms to a maximum of 19.4 kPa for an ignition delay of 600 ms. Following this peak, the increase of ignition delay led to a decrease in recorded overpressure, down to 9.5 kPa for an ignition delay of 2 s. Therefore, a scattering of experimental data for same release conditions but different ignition location and delay is expected. The main practical objective in this study is derivation of an experimentally based conservative correlation for determining the maximum overpressure that could be produced by delayed ignition of any hydrogen jet for arbitrary ignition conditions. Therefore, the maximum values overpressure ratios  $\Delta P_{exp}/P_0$  are used to build a conservative correlation as in Figure 35 for the analysed tests. Data from approximately 80 experimental tests were used to build the correlation (Royle and Willoughby, 2010; Grune et al., 2013; Grune, 2019; Takeno et al., 2007; Takeno, 2019; Daubech et al., 2015; Miller et al., 2015). Experimental data of tests conducted within PRESLHY by Pro-Science and KIT were used to expand the applicability range of the correlation to cryogenic temperature of a release (Friedrich et al., 2021).

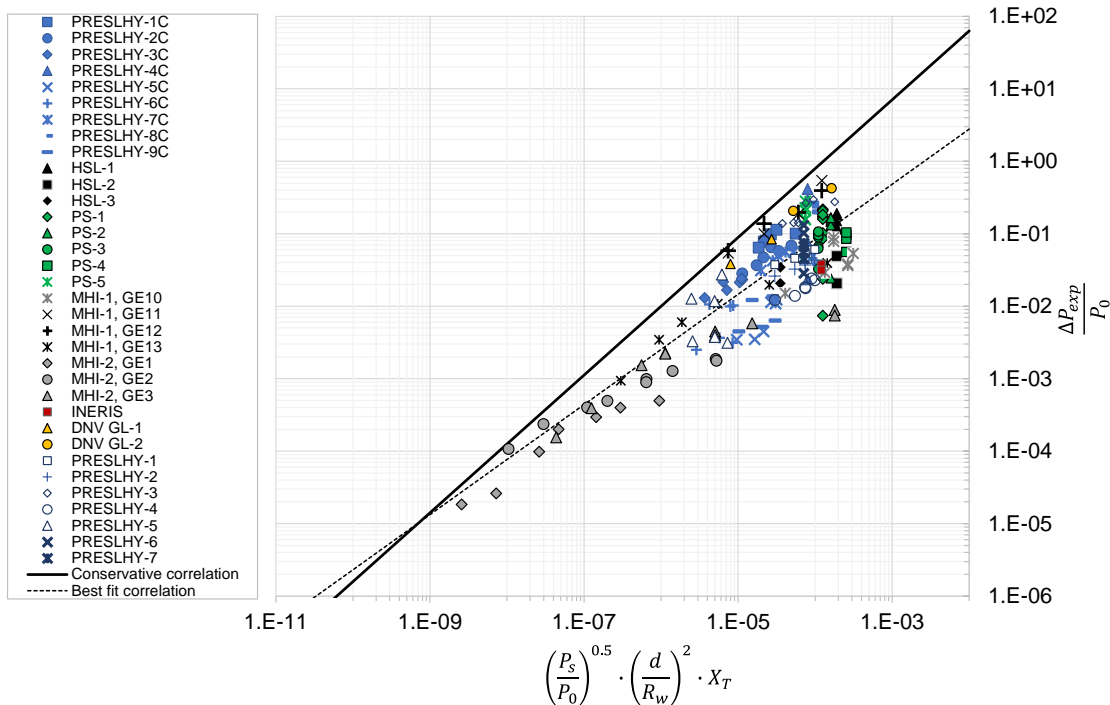


**Figure 35. The correlation for predicting overpressure from delayed ignition of turbulent hydrogen jets versus experiments.**

The semi-empirical correlation, built on similitude analysis as in Figure 35, can be used to estimate the pressure at the target location for ambient temperature jets as:

$$\Delta P_t = P_0 \cdot 5000 \cdot \left[ \left( \frac{P_s}{P_0} \right)^{0.5} \cdot \left( \frac{d}{R_w} \right)^2 \cdot X_T \right]^{0.95} \quad (5.17)$$

where  $X_T = 1$  is a corrective factor depending on the temperature of the release and the associated expansion coefficients' ratio. This is  $X_T = 1$  for ambient temperature releases, whereas for releases at cryogenic temperature is defined as follows:

$$X_T = \frac{T_S E_{i,T_S}}{T_0 E_{i,T_0}} \quad (5.18)$$

From Figure 35, a best fit correlation can be withdrawn as follows:

$$\Delta P_t = P_0 \cdot 92.4 \cdot \left[ \left( \frac{P_s}{P_0} \right)^{0.5} \cdot \left( \frac{d}{R_w} \right)^2 \cdot X_T \right]^{0.76} \quad (5.19)$$

#### 5.4.4 Validity range

The semi-empirical correlation was built using 79 experiments with hydrogen storage pressure 0.5-65 MPa and release diameter 0.5-52.5 mm. Seventeen of the tests were performed at cryogenic temperature (80 K). Maximum validation distance of the target from the release source is 50 m. The correlation is valid for free jets in open-atmosphere, thus in absence of obstacles and congestion. The experimental data used to build the correlation were made available by the following authors: (Royle and Willoughby, 2010), (Grune et al., 2013), (Grune, 2019), (Takeno et al., 2007), (Takeno, 2019), (Daubech et al., 2015), (Miller et al., 2015). Experimental data of tests conducted within PRESLHY were used to expand the applicability range of the correlation (Friedrich et al., 2021).

### 5.4.5 Input values

Table 41 reports the parameters required as input for the model. The column input value reports an example of calculations to test the tool once implemented on the platform. This considers a hydrogen tank having a storage pressure of 35 MPa ( $P_s$ ) and release diameter ( $d$ ) of 2 mm. The release is horizontal and is assumed to be originated at the location (0, 1, 0). Overpressure is estimated at the location with coordinates  $(x_t, y_t, z_t) = (2, 1, 2)$ . Ambient temperature and pressure are 288 K and 101325 Pa.

**Table 41. Input parameters for the reduced model on delayed ignition of hydrogen jets.**

Parameter	Symbol	Input value	Unit	Limits (min-max)	Defaults
Nozzle diameter	$d$	0.002	m	0.0005-0.0525	0.002
Ambient pressure	$P_0$	101325	Pa	100000-102000	101325
Storage pressure	$P_s$	$35 \cdot 10^6$	Pa	$0.5-65 \cdot 10^6$	$70 \cdot 10^6$
Ambient temperature	$T_0$	288	K	280-305	288
Storage temperature	$T_s$	288	K	80-300	288
Jet origin	$(x_0, y_0, z_0)$	(0, 1, 0)	m	0.0-2.0	(0, 1, 0)
Target coordinates	$(x_t, y_t, z_t)$	(2, 1, 2)	m	0.1-50.0	(2, 1, 2)

### 5.4.6 Output values

The semi-empirical correlation is used to calculate the maximum overpressure generated by the delayed ignition of turbulent hydrogen jets for the input parameters given in Table 41. In addition, the correlation may be used to estimate the hazard distances corresponding to defined harm criteria for people. In this example, a “no harm” overpressure of 1.35 kPa is considered, according to the harm criteria proposed in (Baker et al., 1983). A “injury” and “fatality” limit were considered to be 16.5 kPa and 100 kPa respectively, following the harm criteria proposed in (Mannan, 2005). Table 42 reports the output parameters of the tool. Hazard distances are given from the location of the centre of the fast burning cloud. The maximum hazard distance from the nozzle is given in brackets.

**Table 42. Output parameters for the reduced model on delayed ignition of hydrogen jets.**

Parameter	Symbol	Output value	Unit
Overpressure at target location	$\Delta P_t$	$14.53 \cdot 10^3$	Pa
Hazard distance to “no harm” limit	$R_{no\ harm}$	7.4 (8.7)	m
Hazard distance to “injury” limit	$R_{injury}$	2.0 (3.3)	m
Hazard distance to “fatality” limit	$R_{fatality}$	0.8 (2.1)	m

### 5.4.7 Conclusions

The similitude analysis and an extended experimental dataset were used to develop a reliable correlation for predicting the maximum overpressure produced by delayed ignition of hydrogen under-expanded jet. The semi-empirical correlation can be used to calculate the maximum blast wave overpressure for arbitrary ignition conditions of hydrogen release through orifice of any diameter and from hydrogen storage or equipment at any pressure. The conservative correlation can be used as a tool for hydrogen safety engineering and recommendations for Regulations, Codes and Standards. The validation domain of the correlation includes hydrogen releases at storage pressure 0.5-65 MPa, temperature 80-300 K and release diameters in the range 0.5-52.5 mm. The correlation is applicable to free jets in open atmosphere.

### 5.4.8 References

- Baker, W.E., Cox, P.A., Kulesz, J.J. Strehlow, R.A. and Westine, P.S. (1983), *Explosion Hazards and Evaluation*, Elsevier.
- Chen, C. and Rodi, W. (1980), *Vertical Turbulent Buoyant Jets - a Review of Experimental Data*, Pergamon Press, Oxford.
- Daubech, J., Hebrard J., Jallais, S., Vyazmina, E., Jamois, D., Verbecke, F. (2015), Un-ignited and ignited high pressure hydrogen releases : Concentration - Turbulence mapping and overpressure effects, *Journal of Loss Prevention in the Process Industries* 36, 439-446.
- Friedrich, A., Veser, A., Jordan, T. (2021), PRESLY D5.4. Summary of experiment series E5.1 (Ignited discharge) results.
- Grune, J. (2019), "Private communication".
- Grune, J., Sempert, K., Kuznetsov, M. and Jordan, T. (2013), Experimental study of ignited unsteady hydrogen releases from a high pressure reservoir, *International Journal of Hydrogen Energy* 39 (11), 6176–6183.
- Mannan, S. (2005), *Lee's Loss Prevention in the Process Industries*.
- Miller, D., Eastwood, C.D. and Kelly Thomas, J. (2015), Hydrogen jet vapour Cloud explosion: test data and comparison with predictions, 11th Global Congress on Process Safety, Austin, Texas.
- Molkov, V. (2012), *Fundamentals of Hydrogen Safety Engineering I*.
- Royle, M. and Willoughby, D.B. (2010), Consequences of catastrophic releases of ignited and unignited hydrogen jet releases, *International Journal of Hydrogen Energy* 36 (3), 2688–2692.
- Takeno, K. (2019), "Private communication".
- Takeno, K., Okabayashi, K., Kouchi, A., Nonaka, T., Hashiguchi, K. and Chitose, K. (2007), Dispersion and explosion field tests for 40 MPa pressurized hydrogen, Vol. 32, 2144–2153.
- Verbecke, F., Makarov, D. and Molkov, V. (2009), Vles of Lean Hydrogen-Air Deflagrations in a Closed Vessel 5.7 M High. International Conference on Hydrogen Safety, Ajaccio, Corsica, France, June 7-11.

## 5.5 Flame acceleration and detonation transition for cryogenic hydrogen-air mixtures (KIT/PS)

### 5.5.1 Introduction

The model is dedicated to calculate critical hydrogen concentrations for effective flame acceleration and detonation onset for hydrogen-air combustion at cryogenic temperatures. Evaluation of Flame Acceleration (FA) and Detonation-to-Deflagration Transition (DDT) conditions at cryogenic temperatures depends on four major parameters:

1. Geometry of the system:
  - Confinement degree (only confined is considered).
  - Geometry of the channel (smooth, rough, congested/blocked).
  - Scale (characteristic size – cross-section, length of the channel, length of the cloud of hydrogen-air mixture).
2. Mixture characterization:

- Mixture uniformity (only uniform is considered).
  - Initial pressure and temperature.
  - Mixture reactivity (laminar flame velocity, expansion ratio, speed of sound, detonation velocity, detonation pressure, detonation cell size).
3. History and dynamics of combustion process (run-up-distance, runway distance to flame acceleration and DDT).

### 5.5.2 Nomenclature

Table 43 reports the nomenclature employed in the model description.

**Table 43. Nomenclature: FA and DDT for cryogenic hydrogen-air mixtures.**

Parameter	Symbol	Unit
Temperature	<i>T</i>	K
Pressure	<i>p</i>	Pa
Volume concentration of hydrogen	<i>X</i>	%
Blockage ratio	<i>BR</i>	(-)
Distance along the tube	<i>x</i>	m
Diameter of the tube	<i>D</i>	m
Orifice diameter	<i>d</i>	m
Characteristic size of the tube	<i>L</i>	m
Length of the tube	<i>L</i>	m
Universal gas constant	<i>R</i>	J/K/kmol
Density	<i>ρ</i>	kg/m <sup>3</sup>
Expansion ratio	<i>σ</i>	(-)
Detonation cell size	<i>λ</i>	m

### 5.5.3 Model description

Within the flammability limits, three typical combustion regimes can be distinguished for gaseous mixtures. These include slow subsonic deflagrations ( $v < c_r$  - flame velocity  $v$  is less than the speed of sound in reactants  $c_r$ ), fast supersonic flame ( $c_r < v < c_p$  - flame velocity is less than the sound speed in products  $c_p$ , but more than the sound speed in reactants), and detonation ( $v = D_{CJ}$ , Chapman-Jouguet velocity). All possible regimes and characteristic pressure profiles based on paper (Dorofeev et al., 2001) are shown in Figure 36 for hydrogen-air mixtures at initial pressure of 1 bar.

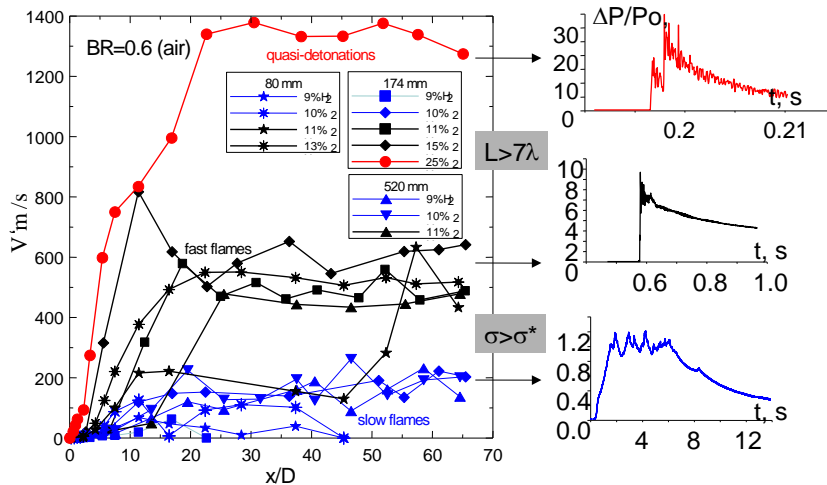


**Figure 36. Combustion regimes for hydrogen-air mixtures in a tube geometry (Dorofeev et al., 2000; 2001).**

As it was suggested by Dorofeev and co-authors (Dorofeev et al., 2000; 2001), the critical expansion rate  $\sigma^*$  and  $7\lambda$  - criteria can be used as potentials for strong flame acceleration and detonation onset, respectively. Mixtures with the expansion rate  $\sigma$  above the critical value  $\sigma^*$  can effectively accelerate to the speed of sound and then detonate, if the detonation criteria  $L > 7\lambda$  is satisfied ( $L$  is the characteristic size of the combustible domain;  $\lambda$  is the detonation cell size). The mixtures with  $\sigma < \sigma^*$  cannot accelerate to the speed of sound and only subsonic combustion regimes may occur. Characteristic combustion pressure depends on flame propagation velocity and can be changed from 1-2 bar for slow combustion, to 6-8 bar for sonic deflagration and 20-40 bar for detonation at initial pressure 1 bar (Figure 36).

#### 5.5.3.1 Flame acceleration

Expansion ratio is the ratio of densities of unburned material  $\rho_u$  to the density of combustion products  $\rho_b$ :  $\sigma = \rho_u / \rho_b \approx T_b / T_0$ . It is roughly equal to the ratio of adiabatic combustion temperature  $T_b$  and initial temperature of the gas  $T_u$ . For hydrogen-air mixtures at ambient conditions, the critical expansion ratio  $\sigma^* = 3.75$  (Dorofeev et al., 2001). It corresponds to 11% of hydrogen in the mixture. In general, critical expansion ratio  $\sigma^*$  is a function of dimensionless integral scale as Peclet number  $Pe = L_T/\delta$  ( $L_T$  - turbulent length scale,  $\delta$  - laminar flame thickness) and Zeldovich number  $\beta$  ( $\beta = E_a(T_b-T_u)/T_b^2$ ). The critical Peclet number  $Pe > 100$  was experimentally found to be required for the strong flame acceleration and to exclude a local flame extinction due to heat losses (Dorofeev et al., 2001). The Peclet number lower than 100 may result in critical expansion ratio increase. The critical expansion ratio  $\sigma^*$  decreases with initial temperature  $T_u$  increase and overall energy activation  $E_a$  decrease. Since adiabatic combustion temperature  $T_b$  is almost independent of the initial temperature  $T_u$ , the critical expansion ratio for elevated temperatures above  $T=293K$  is only a function of the energy activation and temperature (Dorofeev et al., 2001):

$$\sigma^* = 9.010^{-6}x^3 - 0.0019x^2 + 0.1807x + .2314, \quad (5.20)$$

where  $x=E_a/RT_u$ . Assuming a constant activation energy  $E_a=7500K$  for hydrogen-air mixtures in wide range of temperatures and concentrations, this formula gives too conservative results being extrapolated to cryogenic temperatures.

Figure 37 summarizes all experimental data of current PRESLY project (Kuznetsov et al., 2021) with an extension to elevated temperature  $T = 650K$  from paper (Dorofeev et al.,

2001), so that it covers the temperature range from cryogenic T = 90K to elevated temperature T = 650K. Open points show current experimental data on expansion ratios at different temperatures. With a good accuracy the border line between slow (M<1) and fast sonic deflagration (M>1) can be approximated by exponential dependence on initial temperature T[K]:

$$\sigma^* = 2200T^{-1.12} \quad (5.21)$$

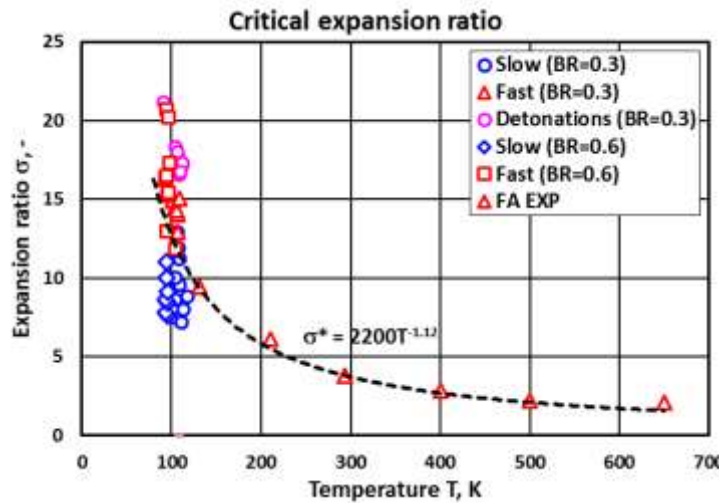


Figure 37. Critical expansion ratio as function of initial temperature based on experiments in obstructed tubes (BR=0.3 and BR=0.6): black dashed line is the border between slow and fast flames.

Experimentally, it was found the critical expansion ratio  $\sigma^* = 12.5$  at 100T of initial temperature of the gas. In terms of hydrogen concentration, it corresponds to about 16% H<sub>2</sub> in air. The cut-off line for fast and slow deflagration described by equation Eq. (5.21) is very close to the simplified hyperbolic dependence on initial temperature. We may transform it as follows:

$$\sigma^*(T) = \sigma^*(T_0) \left( \frac{T_0}{T} \right) \quad (5.22)$$

where  $\sigma^*(T_0) = 3.75$  at the ambient temperature  $T_0 = 293\text{K}$ . Then, for  $T = 100\text{K}$  we get more conservative values of  $\sigma^*(T) = 11.0$  instead of  $\sigma^*(T) = 12.6$  according to Eq. (5.21). Still, the Eq. (5.22) is very valuable for the prediction of flame acceleration limits at different temperatures. Figure 38 shows the dependence of hydrogen concentrations [H<sub>2</sub>]cr corresponding to critical expansion ratio  $\sigma^*$  according to Eq. (5.21) as function of initial temperature. The dependence can be approximated as a polynomial function of initial temperature and might be more useful for practical application than the critical expansion ratio:

$$[H_2]_{cr} = 4.817 \cdot 10^{-5} T^2 - 0.0441T + 19.96. \quad (5.23)$$

Eq. (5.23) shows for instance that hydrogen concentration required for strong flame acceleration to the speed of sound reduces from 16% at 100K, to 14.4% at 150K, and to 13.1% H<sub>2</sub> at 200K. It is in a contradiction with the correlation Eq. (5.20) which shows an opposite trend at cryogenic temperatures in terms of hydrogen concentration.

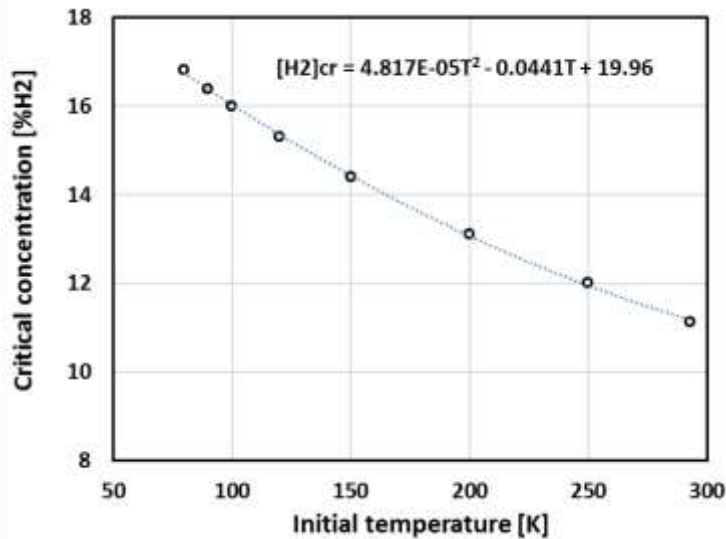


**Figure 38.** Hydrogen concentrations corresponding to critical expansion ratio according to Eq. (5.21) as function of initial temperature.

#### 5.5.3.2 Detonation onset. DDT conditions

One of required conditions for detonation onset is the ability of the flame to reach the speed of sound. It creates sufficient strength of the flow providing the level of turbulence and preheating of unburned material ahead the flame prior to the detonation transition. We evaluate this condition using the abovementioned critical sigma  $\sigma^*$ -criterion.

The model includes the DDT criterion as dimensionless ratio  $L/\lambda$  of the characteristic size  $L$  over the detonation cell size  $\lambda$  as a measure of detonability of the mixture:

$$L/\lambda > N^* \quad (5.24)$$

where  $N^*$  is the critical value for detonation onset (DDT) or detonation propagation dependent on the geometry of the system. The values of critical factor  $N^*$  are collected in Table 44 for several most useful geometries of the channel. We suppose that the DDT criterion does not change at cryogenic conditions. The only change could occur is the detonation cell size.

**Table 44. Dimensionless scale for different processes.**

Dimensionless scale	Critical value $N^*$ , (-)	Detonation relevant phenomenon	References
$D/\lambda$	$1/\pi$	Detonation propagation in a smooth channel with diameter $D$	Moen et al. (1981)
$d/\lambda$	1	Detonation propagation in obstructed tubes with orifice size $d$ ( $BR^*<0.43$ )	Teodorczyk et al. (1988)
$d/\lambda$	3	Detonation propagation in obstructed tubes with orifice size $d$ ( $BR^*=0.6$ )	Teodorczyk et al. (1988), Kuznetsov et al. (2000)
$d/\lambda$	10	Detonation propagation in obstructed tubes with orifice size $d$ ( $BR^*=0.9$ )	Veser et al. (2002)
$L/\lambda$	7	Detonation onset in obstructed channels ( $0.1<BR^*<0.6$ )	Dorofeev et al. (2000)

(\*) Blockage ratio is the ratio of blocked area to the channel cross section area. For cylinder tube geometry it can be expressed as follows:

$$BR = 1 - \frac{d^2}{D^2} \quad (5.25)$$

where  $d$  is the orifice diameter of open area;  $D$  is the inner tube diameter. For complex geometry, the blockage ratio can be expressed as follows

$$BR = \sum A_i / A \quad (5.26)$$

where  $A_i$  is the total area of each visible object blocking the channel cross-section  $A$ . Most of the practical cases are covered by more universal criterion  $L/\lambda > 7$  based on large scale experiments (Dorofeev et al., 2000). Characteristic size  $L$  for detonation onset is formulated depending on the size of the channel  $D$ , dimension of unobstructed passage between obstacle and sidewall  $d$  and spacing between repeating obstacles  $S$ :

$$L = \frac{D + S}{2(1 - d/D)} \quad (5.27)$$

It can be more convenient to express the ratio  $d/D$  through the blockage ratio  $BR$  because parameter  $d$  is not well defined for the complex geometry of obstacles:

$$d/D = \sqrt{1 - BR} \quad (5.28)$$

Then, assuming equidistant spacing between vehicles  $S = D$ , Eq. (5.27) can be derived as a function of blockage ratio  $BR$  and an equivalent diameter  $D$  keeping constant the DDT condition  $L/\lambda = 7$ :

$$L = \frac{D}{1 - \sqrt{1 - BR}} = 7\lambda \quad (5.29)$$

Table 45 summarizes the results of such a practical transformation of Eq. (5.27). It may tell us several conclusions useful for safety assessment. For very small blockage  $BR = 0.1$  characteristic length for DDT is about 20 calibres ( $L/D = 19.5$ ). For practically unblocked channel ( $BR=0.1$ ), the critical ratio  $D/\lambda = 0.36$  approaches the ratio  $D/\lambda = 1/\pi$  found by Moen et al. (1981) for smooth tubes. The critical ratios  $d/\lambda = 0.96$  for  $BR = 0.3$  and  $d/\lambda = 1.22$  for  $BR = 0.4$  are very close to the DDT criterion  $d/\lambda = 1$  found by Teodorczyk et al. (1988) for obstructed tube with  $BR < 0.43$ . Higher blockage leads to larger ratios  $D/\lambda$  and  $d/\lambda$ .

**Table 45. Critical ratios for DDT as function of blockage ratio.**

Blockage ratio BR	L/D	D/λ	d/λ
0.1	19.49	0.36	0.34
0.2	9.47	0.74	0.66
0.3	6.12	1.14	0.96
0.4	4.44	1.58	1.22
0.5	3.41	2.05	1.45
0.6	2.72	2.57	1.63

Both of aforementioned criteria for flame acceleration and DDT also require the satisfaction of so-called run-up distance (RUD) criterion  $X_D < L$ , where  $L$  is the characteristic length of the channel (Veser et al., 2002; Kuznetsov et al., 2005; Ciccarelli et al., 2008).  $X_D$  is the distance required for flame acceleration and detonation

preconditioning. If dimension  $L$  is longer than the run-up-distance to the speed of sound  $X_D$  then the detonation may occur.

The run-up-distance to detonation depends on mixture reactivity (expressed in terms of laminar flame speed and detonation cell size) and level of turbulence. Both factors can promote flame acceleration and shorten the run-up distance  $X_D$ . High level of turbulence can be managed by fans or obstacles. If there are no obstacles and the channel is relatively smooth, then the boundary layer is the only a source of the turbulent motion. Based on the critical thickness of the boundary layer for detonation onset  $\delta = 10\lambda$  a run-up-distance to detonation was experimentally evaluated depending on the tube roughness (Kuznetsov et al., 2005):

$$X_D = (500 \div 550) \lambda, \quad (5.30)$$

Eq. (5.30) is valid for very thick tubes similar to tunnel with  $D > 20\lambda$ . For relatively narrow tubes with  $10\lambda < D < 20\lambda$  the run-up-distance  $X_D$  is proportional to tube diameter  $D$  depending on roughness  $\Delta$ :

$$X_D = (24-27) D, \quad \Delta = 100\mu \quad (5.31)$$

$$X_D = (18-19) D, \quad \Delta = 1000\mu \quad (5.32)$$

$$X_D = (12-14) D, \quad \Delta = 5000\mu \quad (5.33)$$

These values fit very well to  $X_D = (15-40) D$  according to papers (Bollinger et al., 1961; Laffitte et al., 1926). To take into account an integral effect of roughness and blockage of the channel, semi-empirical correlations for run-up distance  $X_D$  have been proposed in (Veser et al., 2002; Ciccarelli et al., 2008) involving boundary layer theory. The problem is that such correlations cannot be used at cryogenic temperatures because they involve also such measures of mixture reactivity as laminar flame speed, which is an incognita at such conditions (Veser et al., 2002):

$$X_D = \frac{a_p D (1 - BR)}{(1 + 1.5 \cdot BR) 10 S_L (\sigma - 1)} \quad (5.34)$$

where  $a_p$  is the sound speed in combustion products;  $S_L$  is the laminar flame speed. However, a parametric analysis of  $X_D$  correlation (Eq. 5.34) shows that the run-up distance to sonic flame or detonation at cryogenic temperatures ( $T = 100K$ , for instance) can be almost the same because two times reduced speed of sound  $a_p$  will be compensated by two times reduced product  $S_L(\sigma - 1)$ .

An attempt to evaluate the run-up distance to detonation can be done by using Eq. (5.29). The run-up distance in tube calibers  $L/D$  as function of blockage ratio  $BR$  is shown in Table 45. The value  $L/D = 19.5$  for  $BR=0.1$  is very close to that for tube roughness  $\Delta = 1000\mu$  (Kuznetsov et al., 2005). The data in Table 45 are quite close to experimental run-up distances as function of blockage ratio (Kuznetsov et al., 2002):

$$X_D = (10-12)D \quad (BR = 0.3) \quad (5.35)$$

$$X_D = (3-4)D \quad (BR = 0.6) \quad (5.36)$$

$$X_D = (2-3)D \quad (BR = 0.9) \quad (5.37)$$

The detonability factor as the detonation cell size  $\lambda$  is not included in the consideration in Eqs. (5.34-5.37). Then, it might be a curious result obtained that the distance is enough for the detonation onset but the detonation cell size is too big for the system to make the

mixture detonable. In such a case, the flame accelerates only to the speed of sound without a detonation transition. Another disadvantage of run-up distance correlations Eqs. (5.35-5.37) is that there is no dependence of run-up distance on temperature because no temperature dependent parameters are included.

### 5.5.3.3 Mixture characterization. Strength of the explosion.

The detonation cell size is the measure of detonability to be used to evaluate the detonation propagation and detonation transition criteria:

$$D = \frac{\lambda}{\pi} \quad \text{smooth tube (BR = 0-0.1)} \quad (5.38)$$

$$d = \lambda \quad \text{obstructed tube (BR = 0.3)} \quad (5.39)$$

$$d = 3\lambda \quad \text{obstructed tube (BR = 0.6)} \quad (5.40)$$

$$d = 10\lambda \quad \text{obstructed tube (BR = 0.9)} \quad (5.41)$$

The run-up distance to detonation at cryogenic temperatures was experimentally found to be two times shorter than at ambient conditions:

$$X_D = 500\lambda \quad \text{smooth tube (BR = 0)} \quad (5.42)$$

Recently, the data at cryogenic temperature T = 100K were experimentally obtained in (Kuznetsov et al., 2002). Figure 39 shows a comparison of experimental detonation cell sizes at cryogenic (T=100K) obtained in current project (Kuznetsov et al., 2021) and at ambient temperature (T=293K) calculated by CELL\_H2 code based on detail chemistry and gas dynamics of detonation (Gavrikov et al., 2000). The data for detonation cell sizes can be approximated as polynomial dependence on hydrogen concentration:

$$\lambda = 0.0006724[H_2]^4 - 0.1039[H_2]^3 + 6.0786[H_2]^2 - 159.74[H_2] + 1603.3 \quad (5.43)$$

where [H<sub>2</sub>] is the hydrogen concentration in volumetric percent.

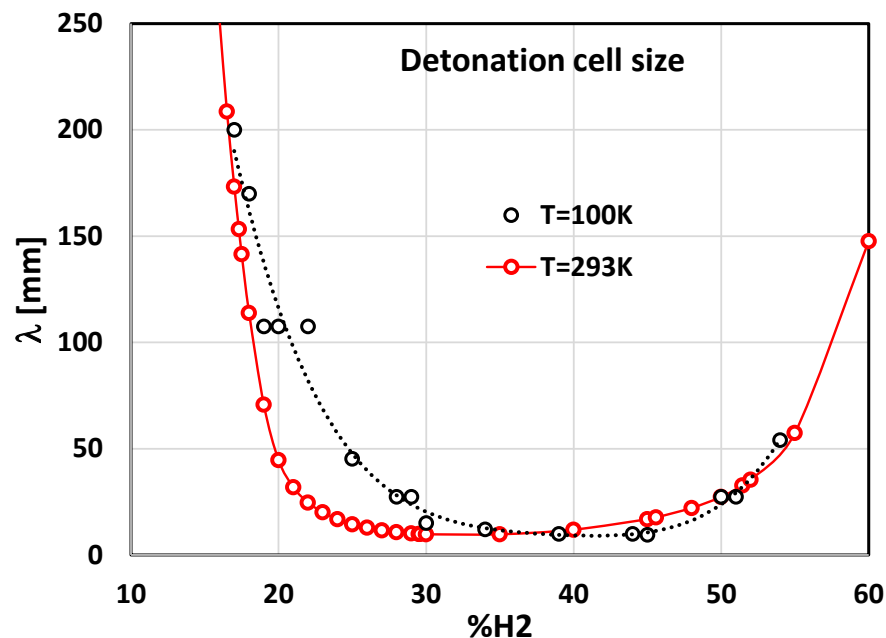
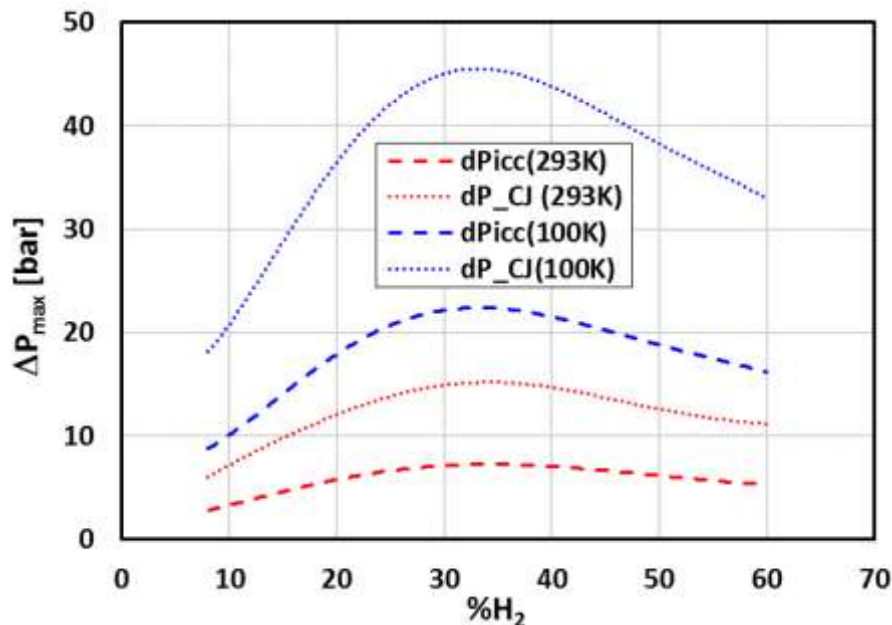


Figure 39. Experimental detonation cell size at cryogenic temperature T=100K in comparison with the data at ambient temperature T = 293K.

Surprisingly, the detonation cell sizes in the range 30-50%H<sub>2</sub> at cryogenic temperatures insignificantly differ from the data at ambient temperature. The only two-three times difference occurs between 20-30%H<sub>2</sub>.

Maximum combustion pressure is the integral characteristic of combustion process, which depends on energy of combustion and dynamics of flame propagation. Theoretically, the maximum combustion pressure for sonic deflagration is of the order of adiabatic combustion pressure  $P_{icc}$ . For detonation, characteristic pressure is the Chapman-Jouguet pressure,  $P_{CJ}$ . The STANJAN code (Reynolds, 1986) and Cantera code (Goodwin, 2001) based on NASA thermodynamic database are able to calculate the  $P_{icc}$  pressure and Chapman-Jouguet pressure even to LN<sub>2</sub> temperature of 78K. Comparison of maximum combustion pressure,  $\Delta P_{icc}$  and  $\Delta P_{CJ}$ , at cryogenic temperature T=100K with the data at ambient temperature T = 293K (Figure 40) shows that even sonic deflagration produces a pressure 3 times higher than that at ambient initial temperature and exceeds 1.5 times the detonation pressure at the ambient initial temperature. This means that cryogenic hydrogen combustion is much more dangerous than the detonation at ambient temperature.



**Figure 40.** Maximum combustion pressure for different hydrogen-air mixtures at cryogenic temperature T=100K in comparison with the data at ambient temperature T = 293K.

Similar to Eq. (5.22), the maximum combustion pressures at cryogenic temperature P(T) can be calculated from the reference data at ambient conditions P( $T_0$ ) times the temperature factor (Table 46):

$$P_{icc}(T) = P_{icc}(T_0) \cdot \left( \frac{T_0}{T} \right) \quad (5.44)$$

$$P_{CJ}(T) = P_{CJ}(T_0) \cdot \left( \frac{T_0}{T} \right) \quad (5.45)$$

where  $P_{icc}(T)$  and  $P_{CJ}(T)$  are the adiabatic combustion pressure and Chapman-Jouguet detonation pressure. Figure 41 demonstrates very good availability of Eqs. (5.44-5.45) to predict maximum combustion pressure at cryogenic temperatures based on reference data for stoichiometric hydrogen-air mixture at ambient temperature T=293K. The same dependence should be true for any other hydrogen concentration in the gas.

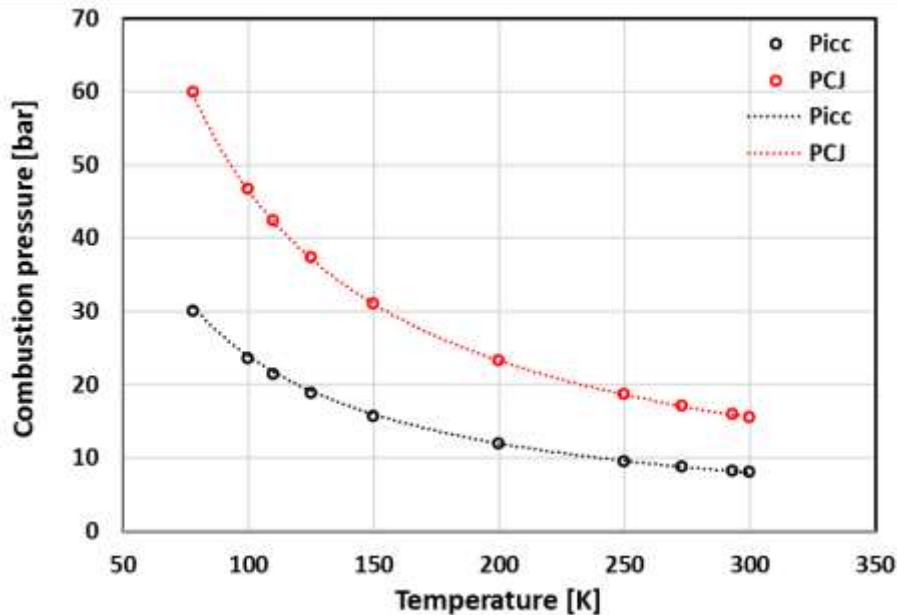


**Figure 41.** Chapman-Jouguet detonation pressure  $P_{CJ}$  and adiabatic combustion pressure  $Picc$  as a function of initial temperature for stoichiometric hydrogen-air mixture: open points – calculations by STANJAN code; dotted line – Eqs. (5.44-5.45).

**Table 46.** Main properties of hydrogen-air combustible mixtures at ambient temperature  $T=293K$ .

H2 mole fraction* $X_{H2}$	Picc [bar]	$P_{CJ}$ [bar]	H2 mole fraction $X_{H2}$	Picc [bar]	$P_{CJ}$ [bar]
0.08	3.80	7.12	0.25	7.74	15.06
0.09	4.10	7.72	0.296	8.26	16.10
0.1	4.39	8.31	0.3	8.29	16.14
0.11	4.67	8.87	0.35	8.27	16.13
0.12	4.94	9.42	0.4	8.00	15.60
0.13	5.20	9.95	0.45	7.66	14.91
0.14	5.46	10.47	0.5	7.28	14.14
0.15	5.71	10.97	0.55	6.85	13.27
0.16	5.95	11.46	0.6	6.38	12.32
0.18	6.41	12.38	0.65	5.87	11.30
0.2	6.84	13.24	0.7	5.32	10.20
0.22	7.23	14.03	0.75	4.73	9.01

\* The data for intermediate concentration can be linearly or by spline interpolated.

Optionally, the same behaviour of maximum combustion pressure should be for hydrogen-oxygen mixtures at cryogenic temperatures. Figure 42 shows the comparison of theoretical maximum combustion pressure for sonic deflagration and detonations for hydrogen-oxygen mixtures at cryogenic and ambient temperatures. The data were calculated by STANJAN code (Reynolds, 1986) and Cantera code (Goodwin, 2001) based on NASA thermodynamic database as the values of adiabatic combustion pressure  $Picc$  for sonic deflagration and Chapman-Jouguet pressure  $P_{CJ}$  for detonations. The same relationships Eqs. (5.44-5.45) can be used for hydrogen-oxygen mixtures as well to calculate the maximum combustion pressures at cryogenic temperature  $T$  based on the data at ambient temperature  $T = 293K$  taken from the plot Figure 42.

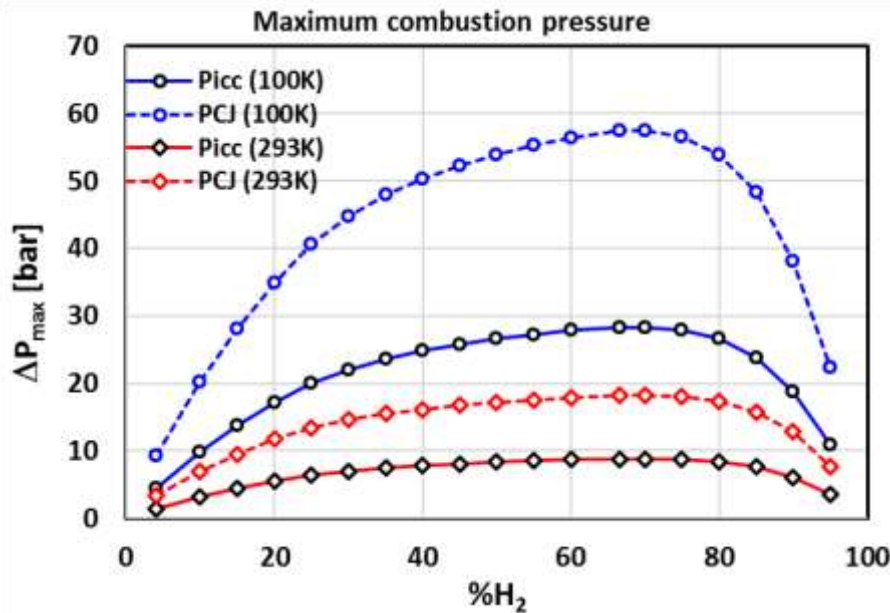


**Figure 42. Maximum combustion pressure for different hydrogen-oxygen mixtures at cryogenic temperature T=100K in comparison with the data at ambient temperature T = 293K.**

During the combustion process, the flame can accelerate to the speed of sound or to detonation. Thus, characteristic combustion pressure should be of the order of Picc or P\_CJ. In case of transient regime, a gas dynamic dependence can be used in an assumption that flow velocity behind shock wave is equal to visible flame velocity:

$$\frac{P_2}{P_1} = \frac{2\gamma}{\gamma+1} M^2 - \frac{\gamma-1}{\gamma+1} \quad (5.46)$$

where  $P_2$  is the dynamic combustion pressure in our case;  $P_1$  is the initial pressure 1 bar;  $\gamma$  is the adiabatic coefficient of burned composition;  $M = v/c$  is the Mach number as a ratio of flow (fame) velocity  $v = U_f$  over the speed of sound in reactants  $c = c_r$ . Figure 43 shows the difference of dynamic pressure at cryogenic temperature T = 100K in comparison with ambient initial temperature for the same stoichiometric hydrogen-air mixture. Dynamic pressure at cryogenic temperature is 2-3 times higher than at ambient temperature for the same flow velocity. The reasons are almost two times lower speed of sound and larger adiabatic coefficient  $\gamma$  at cryogenic temperature. Such behaviour was experimentally confirmed within PRESLHY project for different tube geometries (Figure 44). It was shown that the maximum combustion pressure at the temperature T = 100K is about 2 times higher than at ambient temperature. It is of practical interest that the dependence pressure vs. flame velocity is practically linear. Theoretically, the overpressure of about 2.6 bar corresponds to the flow speed with the speed of sound ( $M = 1$ ). This is the main reason to prevent fast sonic deflagration for safety applications.

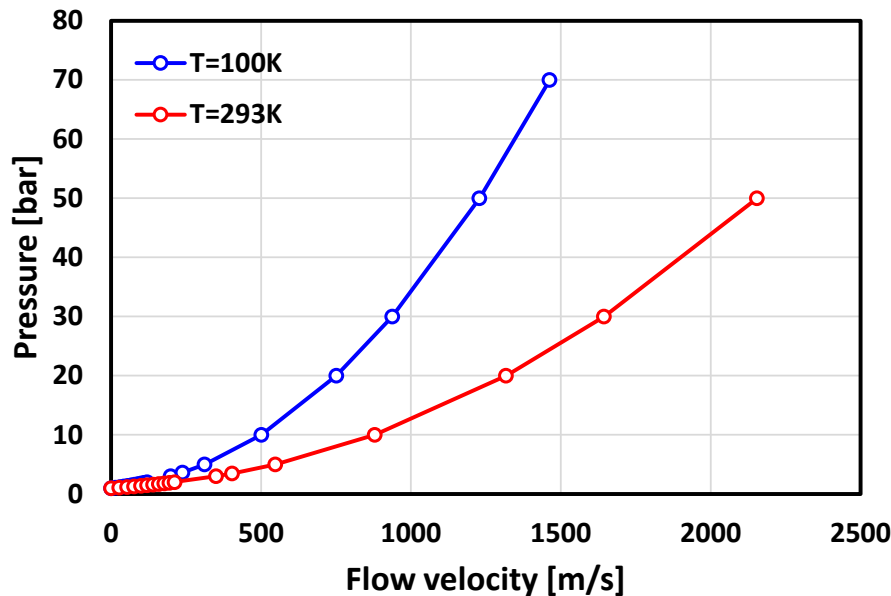


Figure 43. Dynamic pressure as a function of flow velocity calculated for stoichiometric hydrogen air at two temperatures.

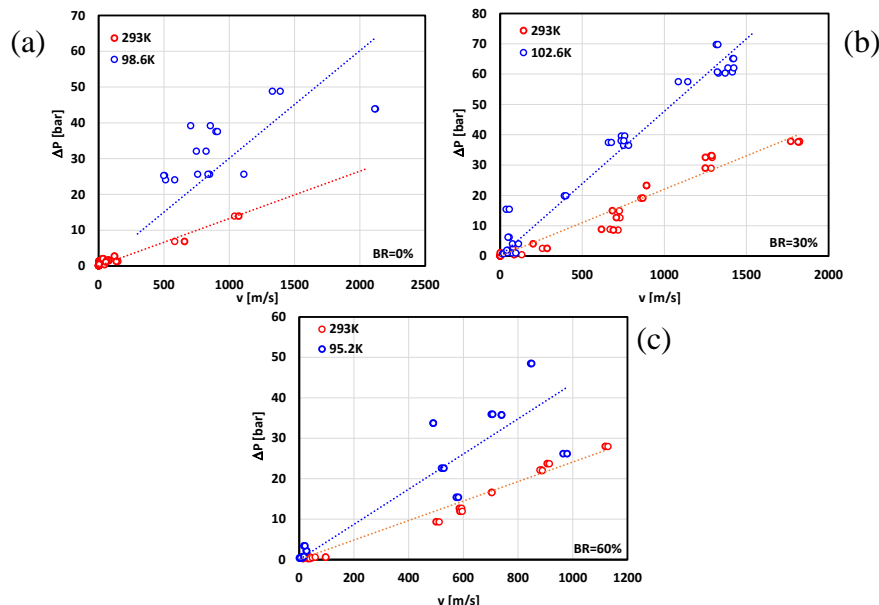


Figure 44. Maximum combustion pressure as function of characteristic flame velocity in obstructed and smooth tube: a) BR=0%; b) BR=30%; c) BR=60%.

#### 5.5.4 Validity range

The model works at atmospheric pressure of 1 bar within the temperature range from 90K to 293K in wide range of hydrogen concentrations from 8 to 60 vol. %. The model covers elongated structures as tubes, channels, sequences of rooms with smooth and rough walls. It also considers the blockage of channels from 10 to 60%.

#### 5.5.5 Calculation procedure: required parameters and algorithm

This section summarises the detailed calculation procedure, with equations, loops, “if” statements, algorithms etc. which will be performed to obtain the required output results. The calculation procedure will change according to the following cases identified in 5.5.3:

- Option 1: Sonic deflagration in obstructed tube (BR=0.3).
- Option 2: Detonation in obstructed tube (BR=0.3).

- Option 3: Slow deflagration in obstructed tube (BR=0.6).
- Option 4: Detonation in smooth tube (BR=0).

The following sections report in detail the required tabulated input parameters, calculation procedure and output parameters for each of the cases.

#### 5.5.5.1 Option1: Sonic deflagration in obstructed tube (BR=0.3)

Table 47. Input parameters for option 1: sonic deflagration in obstructed tube (BR=0.3).

Parameter	Symbol	Input value	Unit	Limits (min-max)	Defaults
Hydrogen mole fraction	X <sub>H<sub>2</sub></sub>	0.20	(-)	0.08-0.6	0.2
Initial temperature	T <sub>0</sub>	100	K	90-650	100
Initial pressure	p <sub>0</sub>	1	bar	1	1
Tube diameter	D	0.1	m	0.02-1	0.1
Tube Length	L	10	m	1-100	1
Blockage ratio	BR	0.3	(-)	0-0.9	0.3

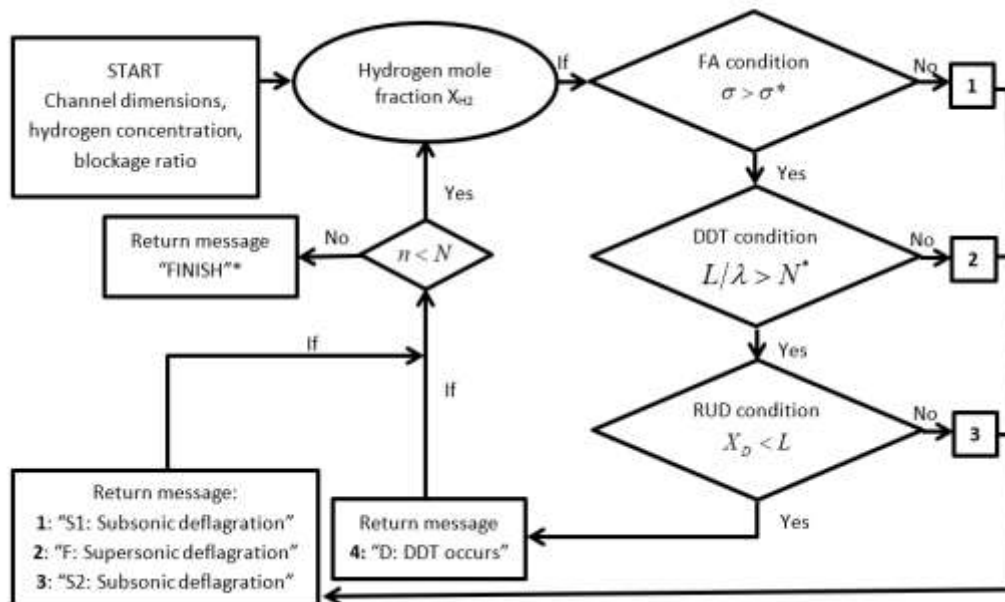


Figure 45. Algorithm of solution for option 1: sonic deflagration in obstructed tube (BR=0.3). (\*) Maximum possible combustion pressure can be evaluated here.

Table 48. Algorithm of solution for option 1: sonic deflagration in obstructed tube (BR=0.3). Steps 1, 2, 3...

1	Hydrogen mole fraction	0.2	(-)
2	Blockage ratio	BR = 0.3	(-)
3	Expansion ratio, σ	Table 49: σ = 15.02	(-)
4	Critical expansion ratio, σ*	Eq. (5.21): σ* = 12.6	(-)
5	Flame acceleration evaluation	σ > σ*	Yes/No
6	Detonation cell size, λ	Eq. (5.43): λ = 0.0006724[H <sub>2</sub> ] <sup>4</sup> - 0.1039[H <sub>2</sub> ] <sup>3</sup> + 6.0786[H <sub>2</sub> ] <sup>2</sup> - 159.74[H <sub>2</sub> ] + 1603.3 = 116	mm
7	Pre-detonation length, L	Eq. (5.27): L <sub>D</sub> = (D + S)/2(1 - d/D) or	m

		Eq. (5.29): $L_D = \frac{D}{1 - \sqrt{1 - BR}} = 0.612 \text{ m if } (S=D)$	
8	Detonation evaluation	$L_D < 7\lambda = 0.814 \text{ m}$	Yes/No
9	FA and DDT run-up-distance, $X_D$	Eq. (5.29): $L_D = \frac{D}{1 - \sqrt{1 - BR}} = 0.612 \text{ m if } (S=D)$ or Eq. (5.35): $X_D = (10 \div 12)D = 1 \div 1.2 \text{ m}$	m
10	Slow/fast regime evaluation	$L_D, X_D < L = 10 \text{ m}$	Yes/No
11	Characteristic flame speed, $U_f$	<b>Fast flame:</b> $U_f = a_p = 820 \text{ m/s}$	m/s
12	Characteristic pressure, $\Delta P$	Table 49: $\Delta P_{\max} = P_{icc} - P_0 = 16.66 \text{ bar}$	bar
13	Characteristic pressure, $\Delta P$	Figure 44(b) $\Delta P_{\max} = 0.0477 U_f = 39.1 \text{ bar}$	bar
14	Final regime evaluation	<b>Fast:</b> supersonic deflagration	

**Table 49. Main properties of hydrogen-air combustible mixtures at cryogenic temperature T=100K.**

H2 mole fraction* $X_{H_2}$	Expansion ratio** $\sigma [-]$	Sound speed in reactants cr [m/s]	Sound speed in products cp [m/s]	Adiabatic combustion pressure Picc [bar]	Detonation pressure P_CJ [bar]
0.08	7.30	208	554	8.44	18.46
0.09	8.03	209	582	9.34	20.27
0.1	8.73	210	608	10.21	22.02
0.11	9.42	211	633	11.06	23.72
0.11	9.42	211	633	11.06	23.72
0.12	10.10	212	657	11.88	25.36
0.15	12.04	216	723	14.21	30.03
0.16	12.66	218	744	14.94	31.51
0.17	13.27	219	764	15.65	32.93
0.18	13.87	220	784	16.34	34.31
0.19	14.45	222	803	17.01	35.65
0.2	15.02	223	821	17.66	36.95
0.22	16.13	226	857	18.89	39.43
0.25	17.67	231	906	20.57	42.82
0.28	19.02	235	946	21.99	45.70
0.29	19.38	237	956	22.34	46.37
0.3	19.59	239	966	22.56	46.82
0.34	19.18	246	997	22.39	46.55
0.39	18.25	256	1014	21.47	44.65
0.44	17.22	266	1029	20.37	42.42
0.45	17.01	269	1032	20.14	41.95
0.5	15.90	281	1046	18.91	39.46
0.51	15.67	284	1048	18.65	38.94
0.54	14.97	292	1056	17.85	37.34
0.58	13.99	305	1066	16.73	35.08
0.6	13.49	312	1070	16.15	33.91

\* The data for intermediate concentration can be linearly or by spline interpolated.

\*\* Main properties calculated by STANJAN, Cantera and NIST Standard Reference Database (Goodwin, 2001; Reynolds, 1986; Manion et al., 2015).

\*\*\* Detonation cell sizes calculated with CELL\_H2 program based on (Gavrikov et al., 2000).

**Table 50. Output values for option 1: sonic deflagration in obstructed tube (BR=0.3).**

Parameter name	Symbol	Output value	Unit
Expansion ratio	$\sigma$	15.02	(-)
Critical expansion ratio	$\sigma^*$	12.6	(-)
Detonation cell size	$\lambda$	116	mm
Critical FA/DDT length	$L_D$	0.612	m
FA and DDT run-up-distance	$X_D$	1-1.2	m
Maximum flame speed	$U_f$	820	m/s
Maximum combustion pressure	$\Delta P_{\max}$	16.66	bar

### 5.5.5.2 Option 2: Detonation in obstructed tube (BR=0.3)

**Table 51. Input values for option 2: detonation in obstructed tube (BR=0.3).**

Parameter	Symbol	Input value	Unit	Limits (min-max)	Defaults
Hydrogen mole fraction	$X_{H_2}$	0.25	(-)	0.08-0.6	0.2
Initial temperature	$T_0$	100	K	90-650	100
Initial pressure	$p_0$	1	bar	1	1
Tube diameter	$D$	0.1	m	0.02-1	0.1
Tube Length	$L$	10	m	1-100	
Blockage ratio	$BR$	0.3	(-)	0-0.9	0.3

**Table 52. Algorithm of solution for option 2: detonation in obstructed tube (BR=0.3). Steps 1, 2, 3...**

1	Hydrogen mole fraction	0.25	(-)
2	Blockage ratio	$BR = 0.3$	(-)
3	Expansion ratio, $\sigma$	Table 49: $\sigma = 17.67$	(-)
4	Critical expansion ratio, $\sigma^*$	Eq. (5.21): $\sigma^* = 12.6$	(-)
5	Flame acceleration evaluation	$\sigma > \sigma^*$	Yes/No
6	Detonation cell size, $\lambda$	Eq. (5.43): $\lambda = 0.0006724[H_2]^4 - 0.1039[H_2]^3 + 6.0786[H_2]^2 - 159.74[H_2] + 1603.3 = 48.1$	mm
7	Pre-detonation length, L	Eq. (5.27): $L_D = (D + S)/2(1 - d/D)$ or Eq. (5.29): $L_D = \frac{D}{1 - \sqrt{1 - BR}} = 0.612 \text{ m if } (S=D)$	m
8	Detonation evaluation	$L_D > 7\lambda = 0.337 \text{ m}$	Yes/No
9	FA and DDT run-up-distance, $X_D$	Eq. (5.29): $L_D = \frac{D}{1 - \sqrt{1 - BR}} = 0.612 \text{ m if } (S=D) \text{ or}$ Eq. (5.35): $X_D = (10 \div 12)D = 1 \div 1.2 \text{ m}$	m
10	Slow/fast regime evaluation	$L_D, X_D < L = 10 \text{ m}$	Yes/No
11	Characteristic flame speed, $U_f$	<b>Detonation:</b> $D_{CJ} = 1873 \text{ m/s}$	m/s
12	Characteristic pressure, $\Delta P$	Table 49: $\Delta P_{\max} = P_{CJ} - P_0 = 40.8 \text{ bar}$	bar
13	Characteristic pressure, $\Delta P$	Figure 44(b): $\Delta P_{\max} = 0.0477U_f = 89.3 \text{ bar}$	bar
14	Final regime evaluation	<b>Detonation</b>	

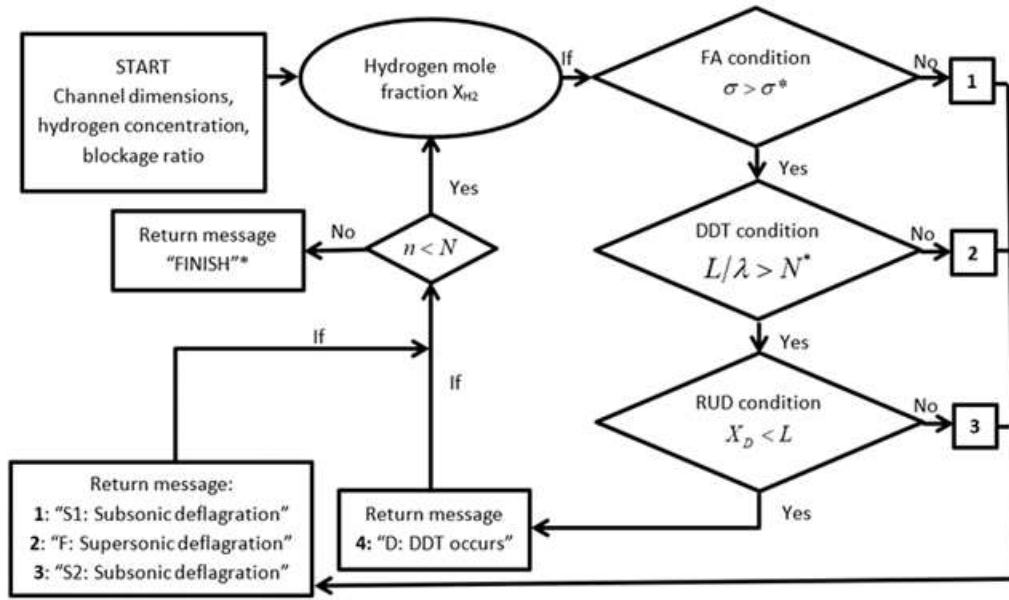


**Figure 46.** Algorithm of solution for option 2: detonation in obstructed tube (BR=0.3).  
 (\*)Maximum possible combustion pressure can be evaluated here.

**Table 53. Output values for option 2: detonation in obstructed tube (BR=0.3).**

Parameter name	Symbol	Output value	Unit
Expansion ratio	$\sigma$	17.67	(-)
Critical expansion ratio	$\sigma^*$	12.6	(-)
Detonation cell size	$\lambda$	48.1	mm
Critical FA/DDT lengtht	$L_D$	0.612	m
FA and DDT run-up-distance	$X_D$	1-1.2	m
Maximum flame speed	$U_f$	1873	m/s
Maximum combustion pressure	$\Delta P_{\max}$	40.1	bar

### 5.5.5.3 Option 3: Slow deflagration in obstructed tube (BR=0.6)

Table 54. Input values for option 3: slow deflagration in obstructed tube (BR=0.6).

Parameter	Symbol	Input value	Unit	Limits (min-max)	Defaults
Hydrogen mole fraction	$X_{H_2}$	0.125	(-)	0.08-0.6	0.2
Initial temperature	$T_0$	100	K	90-650	100
Initial pressure	$p_0$	1	bar	1	1
Tube diameter	$D$	0.1	m	0.02-1	0.1
Tube Length	$L$	10	m	1-100	1
Blockage ratio	$BR$	0.6	(-)	0-0.9	0.3

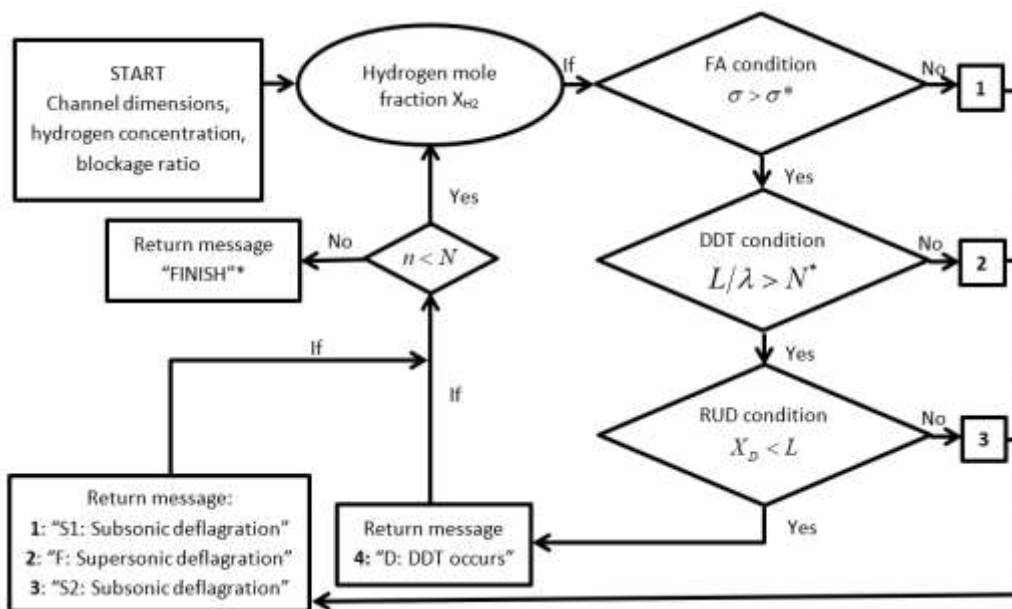


Figure 47. Algorithm of solution for option 3: slow deflagration in obstructed tube (BR=0.6).  
(\*)Maximum possible combustion pressure can be evaluated here.

Table 55. Algorithm of solution for option 3: slow deflagration in obstructed tube (BR=0.6). Steps 1, 2, 3...

1	Hydrogen mole fraction	0.125	(-)
2	Blockage ratio	$BR = 0.6$	(-)
3	Expansion ratio, $\sigma$	Table 49: $\sigma = 10.4$	(-)
4	Critical expansion ratio, $\sigma^*$	Eq. (5.21): $\sigma^* = 12.6$	(-)
5	Flame acceleration evaluation	$\sigma > \sigma^*$	Yes/No
6	Detonation cell size, $\lambda$	$\text{Eq. (5.43): } \lambda = 0.0006724[H_2]^4 - 0.1039[H_2]^3 + 6.0786[H_2]^2 - 159.74[H_2] + 1603.3 = 370$	mm
7	Pre-detonation length, L	$\text{Eq. (5.27): } L_D = (D + S)/2(1 - d/D) \text{ or}$ $\text{Eq. (5.29): } L_D = \frac{D}{1 - \sqrt{1 - BR}} = 0.272 \text{ m if } (S=D)$	m
8	Detonation evaluation	$L_D \ll 7\lambda = 2.590 \text{ m}$	Yes/No
9	Characteristic flame speed, $U_f$	<b>Slow:</b> $U_f = 30 - 200 \text{ m/s}$	m/s

12	Adiabatic coefficient, $\gamma$	$\gamma = 1.438$	(-)
12	Speed of sound, $c_r$	$c_r = 213 \text{ m/s}$	m/s
12	Mach number	$U_f = \frac{2}{\gamma+1} \left( M - \frac{1}{M} \right) \rightarrow M = 1.0895 - 1.3263$	(-)
12	Characteristic pressure, $\Delta P$	Eq. (26): $\frac{P_2}{P_1} = \frac{2\gamma}{\gamma+1} M^2 - \frac{\gamma-1}{\gamma+1} \rightarrow \Delta P_{\max} = 0.22 - 0.895 \text{ bar}$	(-)
13	Characteristic pressure, $\Delta P$	Figure 44(c): $\Delta P_{\max} = 0.0435 U_f = 1.3 - 4.35 \text{ bar}$	bar
14	Final regime evaluation	<b>Slow deflagration</b>	

**Table 56. Output values for option 3: slow deflagration in obstructed tube (BR=0.6).**

Parameter name	Symbol	Output value	Unit
Expansion ratio	$\sigma$	10.4	(-)
Critical expansion ratio	$\sigma^*$	12.6	(-)
Detonation cell size	$\lambda$	370	mm
Critical FA/DDT lengtht	$L_D$	0.272	m
Maximum flame speed	$U_f$	30-200	m/s
Maximum combustion pressure	$\Delta P_{\max}$	0.22-2.33	Bar

#### 5.5.5.4 Option 4: Detonation in smooth tube (BR=0)

Table 57. Input values for option 4: detonation in smooth tube (BR=0).

Parameter	Symbol	Input value	Unit	Limits (min-max)	Defaults
Hydrogen mole fraction	$X_{H2}$	0.3	(-)	0.08-0.6	0.2
Initial temperature	$T_0$	100	K	90-650	100
Initial pressure	$p_0$	1	bar	1	1
Tube diameter	$D$	0.1	m	0.02-1	0.1
Tube Length	$L$	10	m	1-100	
Blockage ratio	$BR$	0	(-)	0-0.9	0.3

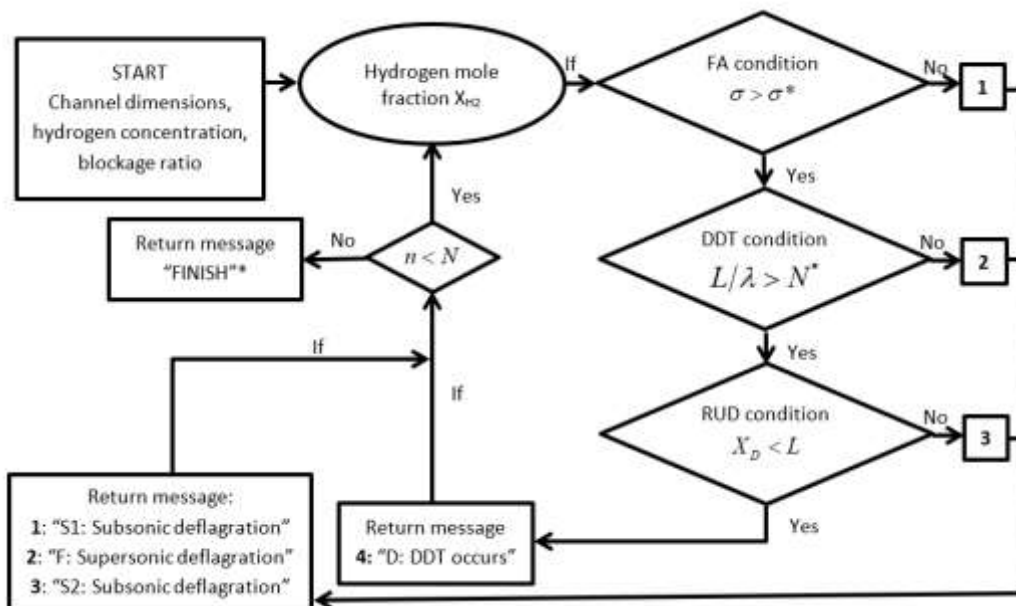


Figure 48. Algorithm of solution for option 4: detonation in smooth tube (BR=0). (\*)Maximum possible combustion pressure can be evaluated here.

Table 58. Algorithm of solution for option 4: detonation in smooth tube (BR=0). Steps 1, 2, 3...

1	Hydrogen mole fraction	0.3	(-)
2	Blockage ratio, roughness	$BR = 0$	(-)
3	Expansion ratio, $\sigma$	Table 49: $\sigma = 19.59$	(-)
4	Critical expansion ratio, $\sigma^*$	Eq. (5.21): $\sigma^* = 12.6$	(-)
5	Flame acceleration evaluation	$\sigma > \sigma^*$	Yes/No
6	Detonation cell size, $\lambda$	$\begin{aligned} \text{Eq. (5.43): } \lambda &= 0.0006724[H_2]^4 - 0.1039[H_2]^3 \\ &+ 6.0786[H_2]^2 - 159.74[H_2] + 1603.3 = 21.2 \end{aligned} \text{ mm}$	mm
7	Critical tube diameter, $D$	$\text{Eq. (5.38): } D = \frac{\lambda}{\pi}$	m
8	Detonation evaluation	$\text{Eq. (5.38): } D = 100\text{mm} > \frac{\lambda}{\pi} = 6.75\text{mm}$	Yes/No
9	FA and DDT run-up-distance, $X_D$	$\text{Eq. (5.42): } X_D = 500\lambda = 10.6\text{m}$	m
10	Slow/fast regime evaluation	$X_D \approx L = 10 \text{ m}$	Yes/No
11	Characteristic flame speed, $U_f$	<b>Detonation: <math>D_{CJ} = 2009 \text{m/s}</math></b>	m/s

12	Characteristic pressure, $\Delta P$	Table 49: $\Delta P_{\max} = P_{CJ} - P_0 = 44.8 \text{ bar}$	bar
13	Characteristic pressure, $\Delta P$	Figure 44(a): $\Delta P_{\max} = 0.0301 U_f = 62.3 \text{ bar}$	bar
14	Final regime evaluation	<b>Detonation</b>	

**Table 59. Output values for option 4: detonation in smooth tube (BR=0).**

Parameter name	Symbol	Output value	Unit
Expansion ratio	$\sigma$	19.6	(-)
Critical expansion ratio	$\sigma^*$	12.6	(-)
Detonation cell size	$\lambda$	21.2	mm
Critical FA/DDT lengtht	$L_D$	6.75	mm
FA and DDT run-up-distance	$X_D$	10.6	m
Maximum flame speed	$U_f$	2009	m/s
Maximum combustion pressure	$\Delta P_{\max}$	44.8	bar

### 5.5.6 Conversion units

**Pressure  $P$ ,** should be in Pascal (Pa). So whatever unit the user selects (bar, Pa, atm, MPa, kPa or psi), pressure should be converted to Pa:

- $P_{(Pa)} = P_{(atm)} \times 101325$
- $P_{(Pa)} = P_{(bar)} \times 100000$
- $P_{(Pa)} = P_{(psi)} \times 6894.76$
- $P_{(Pa)} = P_{(MPa)} \times 1000000$
- $P_{(Pa)} = P_{(kPa)} \times 1000$

Following the completion of calculations, for the purposes of creating the results table, the pressure units should be converted back into those initially chosen by the user:

- $P_{(atm)} = \frac{P_{(Pa)}}{101325}$
- $P_{(bar)} = \frac{P_{(Pa)}}{100000}$
- $P_{(psi)} = \frac{P_{(Pa)}}{6894.76}$
- $P_{(MPa)} = \frac{P_{(Pa)}}{1000000}$
- $P_{(kPa)} = \frac{P_{(Pa)}}{1000}$

**Temperature T,** should be in Kelvin (K). So whatever unit the user selects (C or F), temperature should be converted to K:

- $T_{(K)} = T_{(C)} + 273.15$
- $T_{(K)} = (T_{(F)} + 459.67) * \frac{5}{9}$

Following the completion of calculations, for the purposes of creating the results table, the units of temperature should be converted back into those initially chosen by the user:

- $T_{(C)} = T_{(K)} - 273.15$
- $T_{(F)} = T_{(K)} * \frac{9}{5} - 459.67$

**Distance (length) L** (in our case height and width H&W), should be in meters (m). Whatever unit the user selects (ft, inch, cm), it should be converted to m:

- $L_{(m)} = L_{(ft)} \times 0.3048$
- $L_{(m)} = L_{(inch)} \times 0.0254$
- $L_{(m)} = L_{(cm)} \times 0.01$

Following the completion of calculations, for the purposes of creating the results table, the units of distance should be converted back into the units initially chosen by the user:

- $L_{(ft)} = \frac{L_{(m)}}{0.3048}$
- $L_{(inch)} = \frac{L_{(m)}}{0.0254}$
- $L_{(cm)} = \frac{L_{(m)}}{0.01}$

### 5.5.7 Conclusions

A method to calculate critical conditions for flame acceleration and detonation transition at cryogenic temperatures was proposed for elongated channel or tube geometry with or without obstructions. The method is based on new experimental data on critical expansion ratio and detonation cell sizes obtained within PRESLHY project in the temperature range 90-130K. Then, for predicted flame propagation regime, the maximum combustion pressure is evaluated.

### 5.5.8 References

- Bollinger, L.E., Fong, M.C., Edse, R. (1961), Experimental measurements and theoretical analysis of detonation induction distance. Am Rocket Soc J 1961;31:588.
- Ciccarelli, G., Dorofeev, S. (2008) Flame acceleration and transition to detonation in ducts, Progress in Energy and Combustion Science, Volume 34, Issue 4, 499-550.
- Dorofeev S.B., Sidorov V. P., Kuznetsov M. S., Matsukov I. D., Alekseev V. I. (2000), Effect of scale on the onset of detonations. Shock Waves, v. 10, 137-149.
- Dorofeev S.B., Kuznetsov M.S., Alekseev V.I., Efimenko A.A., Breitung W. (2001), Evaluation of limits for effective flame acceleration in hydrogen mixtures. Journal of Loss Prevention in the Process Industries, Vol 14/6, 583-589.
- Gavrikov, A.I., Efimenko, A.A., Dorofeev, S.B. (2000), A model for detonation cell size prediction from chemical kinetics, Combustion and Flame, Vol. 120, Issues 1–2, 19-33.
- Goodwin, D.G. (2001), Cantera User's Guide, Cal. Institute of Techn., Pasadena, CA.
- Kuznetsov M.S., Alekseev V. I., Dorofeev S. B. (2000), Comparison of critical conditions for DDT in regular and irregular cellular detonation systems. Shock Waves 10, 217-224.
- Kuznetsov, M., Alekseev, V., Matsukov, I. (2002), Deflagration-to-Detonation Transition in H<sub>2</sub>-Air and H<sub>2</sub>-O<sub>2</sub>-N<sub>2</sub> mixtures in channels with obstructions. Advances in Confined Detonations, Torus Press Ltd., Moscow, 26-30.
- Kuznetsov M., Alekseev V., Matsukov I., Dorofeev S. (2005), DDT in a Smooth Tube filled with Hydrogen-Oxygen Mixtures. Shock Waves, vol. 14, No 3, 205-215.
- Kuznetsov, M., Denkevits, A., Veser, A., Friedrich, A., Necker, G., Jordan, T. (2021) Shock tube experiments on flame propagation regimes and critical conditions for flame acceleration and detonation transition for hydrogen-air mixtures at cryogenic temperatures. Submitted to ICHS9, Edinburgh, UK, 2021.
- Laffitte P, Dumanois P. (1926), Influence of pressure on the formation of the explosive wave. Compt Rend Acad Sci Paris, 83:284.

Manion, J.A., Huie, R.E., Levin, R.D., Burgess Jr., D.R., Orkin, V.L., Tsang, W., McGivern, W.S., Hudgens, J.W., Knyazev, V.D., Atkinson, D.B., Chai, E., Tereza, A.M., Lin, C.-Y., Allison, T.C., Mallard, W.G., Westley, F., Herron, J.T., Hampson, R.F. Frizzell, D.H. (2015), NIST Chemical Kinetics Database, NIST Standard Reference Database 17, Version 7.0 (Web Version), Release 1.6.8, Data version 2015.09, National Institute of Standards and Technology, Gaithersburg, Maryland, 20899-8320. Web address: <http://kinetics.nist.gov/>

Moen, I. O., Donato, M., Knystautas, R., Lee, J. H. S. (1981), The influence of confinement on the propagation of detonations near the detonability limit. Symp. (Int.) Combust., 18th, pp. 1615--23. Pittsburgh, Pa : Combust. Inst.

Reynolds, W.C. (1986), The Element Potential Method for Chemical Equilibrium Analysis: Implementation in the Interactive Program STANJAN Version 3, Dept. of Mechanical Engineering, Stanford University, Palo Alto, California, January 1986.

Teodorczyk, A., Lee, J.H., Knystautas, R. (1988), Propagation mechanism of quasi-detonations. 22nd Symposium (Int.) on Combustion. The Combustion Institute, Pittsburgh, 1723–173.

Veser, A., Breitung, W., Dorofeev, S.B. (2002), Run-up distances to supersonic flames in obstacle-laden tubes, J. Phys. IV France, 12, No 7, 333-340.

## 5.6 Fireball size after liquid hydrogen spill combustion (UU, KIT)

### 5.6.1 Introduction

The present correlation determines a fireball size after liquid hydrogen spill combustion. The correlation was built based on results from experiments carried out by Zabetakis (1964). Full description of the model is available in Makarov et al. (2021), which reports as well a correlation to calculate a fireball size after high pressure hydrogen tank rupture in a fire.

### 5.6.2 Nomenclature

Table 60 reports the nomenclature used in the correlation.

**Table 60. Nomenclature for correlation on fireball size from LH<sub>2</sub> spills.**

Parameter	Symbol	Unit
Diameter	<i>D</i>	m
Mass	<i>m</i>	kg

### 5.6.3 Model description

Makarov et al. (2021) built a first correlation to calculate a fireball size from LH<sub>2</sub> spills based on the best fit of experimental data Zabetakis (1961):

$$D_{bf} = 8.16m^{0.45} \quad (5.47)$$

A second correlation provides a conservative correlation to estimate a fireball size from combustion of LH<sub>2</sub> spills:

$$D_c = 10m^{0.45} \quad (5.48)$$

### 5.6.4 Validity range

The model was built based on experimental data by Zabetakis (1964) on a fireball produced by combustion of spills of LH<sub>2</sub> in the range 2.71-87.69 L, which correspond to a hydrogen

mass in the range 0.19–6.21 kg. The measured fireball width varied from 4.59 to 18.48 m, whereas its height from 3.74 to 15.49 m. Validation of the model is available in Makarov et al. (2021).

### 5.6.5 Input and output values

Table 61 reports the parameters required as input for the model. The column input value reports an example of calculations to test the tool once implemented on the platform. Table 62 reports the output parameters of the tool.

**Table 61. Input parameters for the correlation on a fireball size.**

Parameter	Symbol	Input value	Unit	Limits (min-max)	Defaults
Hydrogen mass	$m$	0.2	kg	0.19–6.21	1

**Table 62. Output parameters for the correlation on a fireball size.**

Parameter	Symbol	Output value	Unit
Best fit fireball diameter	$D_{bf}$	3.96	m
Conservative fireball diameter	$D_c$	4.85	m

### 5.6.6 Conclusions

The presented correlation allows the determination of a fireball size after liquid hydrogen spill combustion.

### 5.6.7 References

Makarov, D., Shentsov, V., Kuznetsov, M. and Molkov, V. (2021) Hydrogen Tank Rupture in Fire in the Open Atmosphere: Hazard Distance Defined by Fireball, Hydrogen, Vol. 2 No. 1, pp. 134–146.

Zabetakis, M.G. Flammability Characteristics of Combustible Gases and Vapors; Bureau of Mines: Pittsburgh, PA, USA, 1964.

## 6 Conclusions

The present report aimed at gathering the engineering correlations and tools developed and validated throughout PRESLHY project. The engineering correlations and tools aim at characterising the phenomena associated to cryogenic hydrogen and at assessing the hazards and consequences from likely accident scenarios involving releases, ignition and combustion. Experimental data from literature and from the experimental campaigns carried out within PRESLHY research programme were used to either build semi-empirical and empirical correlations, or to validate theoretical models. The engineering correlations and tools mainly address cryogenic hydrogen applications, however, where relevant and applicable, they cover as well the range of temperatures close to ambient, to either assess if the models are suitable for both cryogenic and ambient temperature hydrogen, or to highlight the eventual differences in behaviour. The engineering correlations and tools are described via a unified template to ease future implementation into existing and/or future integrated platforms for hazards and risks assessment, e.g. the e-Laboratory developed within the ongoing project Net-Tools.

The engineering correlations and tools developed and validated within PRESLHY will be implemented to support and produce guidelines and recommendations for Regulations Codes and Standards.

## Annex 1. Template for tool description

Task 6.4 “Engineering correlations and tools” aims at gathering the correlations developed and validated in WP3-5 and bring them into a unified format suitable for consequent programming and implementation into any existing and/or future integrated platforms for hazards and risks assessment, e.g. European e-Laboratory (ongoing NET-Tools project), HyRAM tool in USA, similar Canadian tool (UTRQ), etc.

The template was prepared by UU and distributed to partners in November 2018. All partners could use the unified template to describe the correlations developed within WP3-5 as soon as available, so that they could be integrated into deliverable D6.5 “Detailed description of novel engineering correlations and tools for LH2 safety, version 2”.

As shown below, the template is designed in 10 sections. As suggested in the Grant Agreement, the template includes a brief scientific summary, the validity range specifying the experimental data where relevant, a short user’s manual which describes the input/output parameters and the detailed algorithm description for implementation in a software, and finally the reference and/or link to publication. The suggested contents and actions for each section are indicated in *italic*. The template may be adapted to the specifics of the described engineering correlation.

### 1. Name of addressed phenomenon

#### 1.1 Name of a tool and responsible partner (e.g. UU)

*In title 1.1 please provide the name of the tool and responsible partner in brackets. In text, provide a short description of the tool.*

##### 1.1.1 Introduction

*In 1.1.1. please provide a short description of the correlation and model, indicating its objective and addressed scenario.*

##### 1.1.2 Nomenclature

*Please provide table with all parameters and units which are used in the model, e.g.*

Table 63. Nomenclature.

Parameter	Symbol	Unit
Area	A	m <sup>2</sup>
Gravity acceleration	g	m/s <sup>2</sup>
Vent height	H	M
Molecular mass	M	kg/kmol
Pressure	p	Pa
Universal gas constant	R	J/K/kmol
Temperature	T	K
Volume fraction of hydrogen	X	-
Density	ρ	kg/m <sup>3</sup>

##### 1.1.3 Model description

*Here please provide model description with main equations, assumptions, graphical representations, references and where to get more information about it (for user).*

##### 1.1.4 Validity range

*Here please indicate the limits within which the model has been validated, providing experimental data when relevant.*

### 1.1.5 Input values

*Please provide table with all initial parameters and units values to be used in the model as input for calculation. The values should be real test values to verify the model during programming.*

*To make a tool more user-friendly as many details as possible should be given, e.g. limits of application for input values (validation range i.e. minimum and maximum), default values for input parameters etc.*

**Table 64. Input parameters and associated details.**

Parameter	Symbol	Input value	Unit	Limits (min-max)	Defaults
Hydrogen pressure	$p_1$		Pa, atm, bar, psi		
Hydrogen temperature	$T_1$		K, C, F		
Orifice diameter	$d_1$		m, cm, ft, inch		

### 1.1.6 Calculation procedure (possible algorithm)

*This section should contain the detailed calculation procedure, with equations, loops, “if” statements, algorithms, etc., which will be performed to obtain the required output results. It should be included here in order to guide programmer and ease the design of the tool. Equations and the calculation procedure should not be visible to the user when the tool is published in its final form.*

### 1.1.7 Output values

*Please provide a table with all output values that the tool will return after calculation is performed. The values should be real test values to verify the model during programming. Please describe in detail what messages should pop out, ways of how data should be saved (excel, txt, pdf, word, jpeg etc.) or dynamic visualization required e.g. plot the graph, table etc.*

**Table 65. Output parameters and associated details.**

Parameter name	Symbol	Output value	Unit
Hydrogen mass flow rate	$\dot{m}$		kg/s, g/s
Vent height	$H$		m, cm, ft, inch
Vent width	$W$		m, cm, ft, inch
Hydrogen volume fraction	$X$		-

### 1.1.8 Conversion of input and output units

*To make the tool more universal and applicable the user should be given a list of choices of different units for input and output results: temperature (K, C, F), pressure (Pa, MPa, KPa, Psi, ATM, Bar etc.), density (kg/m3, g/cm3, g/m3, oz/gal, oz/ft3 etc.), volume (Litre, m3, ft3, etc.), length (m, ft, cm, yard etc.), mass flow rate (g/s, kg/s, g/min, kg/min etc.), volume flow rate (NL/min, m3/min, l/s, l/min etc.) etc.*

*For example pressure P should be in Pascal (Pa) for the purposes of the calculations. So, pressure in any unit selected by the user (bar, Pa, atm or psi) should be converted to Pa:*

- $P_{(Pa)} = P_{(atm)} \times 101325$
- $P_{(Pa)} = P_{(bar)} \times 100000$
- $P_{(Pa)} = P_{(psi)} \times 6894.76$
- $P_{(Pa)} = P_{(MPa)} \times 1000000$

- $P_{(Pa)} = P_{(kPa)} \times 1000$

Following the completion of the calculations, for the purposes of the creation of the results table, the units of pressure should be converted back into the units initially chosen by the user:

- $P_{(atm)} = \frac{P_{(Pa)}}{101325}$
- $P_{(bar)} = \frac{P_{(Pa)}}{100000}$
- $P_{(psi)} = \frac{P_{(Pa)}}{6894.76}$
- $P_{(MPa)} = \frac{P_{(Pa)}}{1000000}$
- $P_{(kPa)} = \frac{P_{(Pa)}}{1000}$

The same applies to temperature, density, distance, volume, mass and volume flow rates, etc.

Please provide two tables for the units which will be stored in the database for each tool, e.g. Table 66 and Table 67.

- Standard units for calculation and storage in database (all values would be stored and processed in these units)

**Table 66. Standard units for calculation and storage in database.**

Parameter name	Standard unit name	Symbol	Unit
Length	Meter	L	m
Temperature	Kelvin	T	K
...			

- Alternative units for user inputs and outputs

**Table 67. Alternative units for user inputs and outputs.**

Parameter name	Unit name	Symbol	Unit	Conversion from standard unit	Conversion to standard unit
Length	foot	L	ft	L(m) / 0.3048	L(ft) * 0.3048
Length	centimetre	L	cm	L(m) / 0.01	L(cm) * 0.01
...					
Temperature	degree Celsius	T	C	T(K) - 273.15	T(C) + 273.15
Temperature	degree Fahrenheit	T	F	T(K) * 9/5 - 459.67	(T(F) + 459.67) * 5/9
...					

### 1.1.9 Conclusions

Please provide brief conclusions on the engineering tool and its applications.

### 1.1.10 References

Please provide reference to the publication presenting the tool validation and any other relevant publication.